

1991

Control of a very flexible robot in gravity

Jay E. Shannan
Iowa State University

Follow this and additional works at: <https://lib.dr.iastate.edu/rtd>

 Part of the [Mechanical Engineering Commons](#)

Recommended Citation

Shannan, Jay E., "Control of a very flexible robot in gravity" (1991). *Retrospective Theses and Dissertations*. 9684.
<https://lib.dr.iastate.edu/rtd/9684>

This Dissertation is brought to you for free and open access by the Iowa State University Capstones, Theses and Dissertations at Iowa State University Digital Repository. It has been accepted for inclusion in Retrospective Theses and Dissertations by an authorized administrator of Iowa State University Digital Repository. For more information, please contact digirep@iastate.edu.

7

92

1

2

1

8

7

U·M·I

MICROFILMED 1992

INFORMATION TO USERS

This manuscript has been reproduced from the microfilm master. UMI films the text directly from the original or copy submitted. Thus, some thesis and dissertation copies are in typewriter face, while others may be from any type of computer printer.

The quality of this reproduction is dependent upon the quality of the copy submitted. Broken or indistinct print, colored or poor quality illustrations and photographs, print bleedthrough, substandard margins, and improper alignment can adversely affect reproduction.

In the unlikely event that the author did not send UMI a complete manuscript and there are missing pages, these will be noted. Also, if unauthorized copyright material had to be removed, a note will indicate the deletion.

Oversize materials (e.g., maps, drawings, charts) are reproduced by sectioning the original, beginning at the upper left-hand corner and continuing from left to right in equal sections with small overlaps. Each original is also photographed in one exposure and is included in reduced form at the back of the book.

Photographs included in the original manuscript have been reproduced xerographically in this copy. Higher quality 6" x 9" black and white photographic prints are available for any photographs or illustrations appearing in this copy for an additional charge. Contact UMI directly to order.

U·M·I

University Microfilms International
A Bell & Howell Information Company
300 North Zeeb Road, Ann Arbor, MI 48106-1346 USA
313/761-4700 800/521-0600

Order Number 9212187

Control of a very flexible robot in gravity

Shannan, Jay Eric, Ph.D.

Iowa State University, 1991

U·M·I

**300 N. Zeeb Rd.
Ann Arbor, MI 48106**



**Control of a very flexible
robot in gravity**

by

Jay E. Shannan

**A Dissertation Submitted to the
Graduate Faculty in Partial Fulfillment of the
Requirements for the Degree of
DOCTOR OF PHILOSOPHY**

Major: Mechanical Engineering

Approved:

Signature was redacted for privacy.

In Charge of Major Work

Signature was redacted for privacy.

For the Major Department

Signature was redacted for privacy.

For the Graduate College

**Iowa State University
Ames, Iowa
1991**

TABLE OF CONTENTS

ACKNOWLEDGMENTS	xiii
DESCRIPTION OF NOMENCLATURE	xiv
1. INTRODUCTION	1
2. LITERATURE REVIEW	3
2.1 Theoretical Studies	4
2.2 Theoretical and Experimental Studies	9
3. ANALYTICAL ROBOT MODEL	14
3.1 Kinetic Energy	14
3.2 Potential Energy	17
3.3 Assumed Modes	17
3.4 Gravitational Correction Term	19
3.5 Equations of Motion	21
3.6 Boundary Conditions	22
3.7 Linearization	23
3.8 Assumed Mode Shapes	26
3.9 Static Equilibrium	28
3.10 Calculation of Strain	31

4. CONTROL ALGORITHMS	33
4.1 Model Parameters	36
4.2 Strain Gage Placement	37
4.3 A Practical Consideration	38
4.4 Proportional-Derivative Controller	38
4.5 Linear Quadratic Regulator	50
4.6 Linear Quadratic Regulator with Prescribed Degree of Stability . . .	61
4.7 Summary of Results	75
5. EXPERIMENTAL TEST BED AND RESULTS	81
5.1 Description of Experimental Test Bed	81
5.2 Calibration Procedure	86
5.3 Proportional-Derivative Experimental Results	87
5.4 Modal Feedback Experimental Results	92
5.5 Summary of Experimental Results	108
6. CONCLUSIONS	113
7. BIBLIOGRAPHY	116

LIST OF TABLES

Table 4.1:	Physical parameters of the robot arm	36
Table 4.2:	Physical parameters of the end masses	36
Table 4.3:	Flexible arm target static equilibrium states	37
Table 4.4:	Summary of the responses of the flexible arm and payloads using the PD control algorithm	77
Table 4.5:	Summary of the responses of the flexible arm and payloads using the LQRA control algorithm	78
Table 4.6:	Summary of the responses of the flexible arm and payloads using the LQRB control algorithm	79
Table 4.7:	Summary of the responses of the flexible arm and payloads using the LQRA2 control algorithm	80
Table 4.8:	Summary of the responses of the flexible arm and payloads using the LQRA3 control algorithm	80
Table 5.1:	Summary of the FC experimental responses of the unloaded arm with a target end point position of 45 degrees.	99
Table 5.2:	Summary of the FC experimental responses of the flexible arm and 23% load with a target end point position of 45 degrees.	100

Table 5.3:	Summary of the FC experimental responses of the flexible arm and 64% load with a target end point position of 45 degrees.	102
Table 5.4:	Summary of the FC experimental responses of the unloaded arm with a target end point position of 90 degrees.	106
Table 5.5:	Summary of the FC experimental responses of the flexible arm and 23% load with a target end point position of 90 degrees.	108
Table 5.6:	Summary of the FC experimental responses of the flexible arm and 64% load with a target end point position of 90 degrees.	109
Table 5.7:	Summary of the experimental responses of the flexible arm and payloads using the P control algorithm	111
Table 5.8:	Summary of the experimental responses of the flexible arm and payloads using the PD control algorithm	112

LIST OF FIGURES

Figure 3.1:	Diagram of flexible arm and end mass	15
Figure 3.2:	Diagram showing shortening effects due to transverse displacement	19
Figure 3.3:	Schematic diagram showing the end point angle at static equilibrium	30
Figure 4.1:	Optimal locations of the first strain gage	39
Figure 4.2:	Optimal locations of the second strain gage	39
Figure 4.3:	PD end point response of a rigid arm with a target end point position of 45 degrees	41
Figure 4.4:	PD torque response of a rigid arm with a target end point position of 45 degrees	41
Figure 4.5:	PD end point response of the unloaded flexible arm with a target end point position of 45 degrees	42
Figure 4.6:	PD torque response of the unloaded flexible arm with a target end point position of 45 degrees	42
Figure 4.7:	PD end point response of the flexible arm and 23% load with a target end point position of 45 degrees	43

Figure 4.8:	PD torque response of the flexible arm and 23% load with a target end point position of 45 degrees	43
Figure 4.9:	PD end point response of the flexible arm and 64% load with a target end point position of 45 degrees	44
Figure 4.10:	PD torque response of the flexible arm and 64% load with a target end point position of 45 degrees	44
Figure 4.11:	PD end point response of a rigid arm with a target end point position of 90 degrees	46
Figure 4.12:	PD torque response of a rigid arm with a target end point position of 90 degrees	46
Figure 4.13:	PD end point response of the unloaded flexible arm with a target end point position of 90 degrees	47
Figure 4.14:	PD torque response of the unloaded flexible arm with a target end point position of 90 degrees	47
Figure 4.15:	PD end point response of the flexible arm and 23% load with a target end point position of 90 degrees	48
Figure 4.16:	PD torque response of the flexible arm and 23% load with a target end point position of 90 degrees	48
Figure 4.17:	PD end point response of the flexible arm and 64% load with a target end point position of 90 degrees	49
Figure 4.18:	PD torque response of the flexible arm and 64% load with a target end point position of 90 degrees	49
Figure 4.19:	LQRA end point response of the unloaded flexible arm with a target end point position of 45 degrees	53

Figure 4.20: LQRA torque response of the unloaded flexible arm with a target end point position of 45 degrees	53
Figure 4.21: LQRA end point response of the flexible arm and 23% end mass with a target end point position of 45 degrees	55
Figure 4.22: LQRA torque response of the flexible arm and 23% end mass with a target end point position of 45 degrees	55
Figure 4.23: LQRA end point response of the flexible arm and 64% end mass with a target end point position of 45 degrees	56
Figure 4.24: LQRA torque response of the flexible arm and 64% end mass with a target end point position of 45 degrees	56
Figure 4.25: LQRB end point response of the flexible arm and 64% end mass with a target end point position of 45 degrees	58
Figure 4.26: LQRB torque response of the flexible arm and 64% end mass with a target end point position of 45 degrees	58
Figure 4.27: LQRB end point response of the unloaded flexible arm with a target end point position of 45 degrees	59
Figure 4.28: LQRB end point response of the flexible arm and 23% end mass with a target end point position of 45 degrees	59
Figure 4.29: LQRA end point response of the unloaded flexible arm with a target end point position of 90 degrees	60
Figure 4.30: LQRA torque response of the unloaded flexible arm with a target end point position of 90 degrees	60
Figure 4.31: LQRA end point response of the flexible arm and 23% end mass with a target end point position of 90 degrees	62

Figure 4.32: LQRA torque response of the flexible arm and 23% end mass with a target end point position of 90 degrees	62
Figure 4.33: LQRA end point response of the flexible arm and 64% end mass with a target end point position of 90 degrees	63
Figure 4.34: LQRA torque response of the flexible arm and 64% end mass with a target end point position of 90 degrees	63
Figure 4.35: LQRB end point response of the unloaded flexible arm with a target end point position of 90 degrees	64
Figure 4.36: LQRB end point response of the flexible arm and 23% end mass with a target end point position of 90 degrees	64
Figure 4.37: LQRB end point response of the flexible arm and 64% end mass with a target end point position of 90 degrees	65
Figure 4.38: LQRB torque response of the flexible arm and 64% end mass with a target end point position of 90 degrees	65
Figure 4.39: LQRA2 end point response of the unloaded flexible arm with a target end point position of 45 degrees	69
Figure 4.40: LQRA2 torque response of the unloaded flexible arm with a target end point position of 45 degrees	69
Figure 4.41: LQRA2 end point response of the flexible arm and 23% end mass with a target end point position of 45 degrees	70
Figure 4.42: LQRA2 torque response of the flexible arm and 23% end mass with a target end point position of 45 degrees	70
Figure 4.43: LQRA2 end point response of the flexible arm and 64% end mass with a target end point position of 45 degrees	72

Figure 4.44: LQRA2 torque response of the flexible arm and 64% end mass with a target end point position of 45 degrees	72
Figure 4.45: LQRA3 end point response of the unloaded flexible arm with a target end point position of 45 degrees	73
Figure 4.46: LQRA3 torque response of the unloaded flexible arm with a target end point position of 45 degrees	73
Figure 4.47: LQRA3 end point response of the flexible arm and 23% end mass with a target end point position of 45 degrees	74
Figure 4.48: LQRA3 torque response of the flexible arm and 23% end mass with a target end point position of 45 degrees	74
Figure 4.49: LQRA3 end point response of the flexible arm and 64% end mass with a target end point position of 45 degrees	76
Figure 4.50: LQRA3 torque response of the flexible arm and 64% end mass with a target end point position of 45 degrees	76
Figure 5.1: Schematic diagram of experimental station	82
Figure 5.2: Experimental station showing the electronic equipment . . .	83
Figure 5.3: Experimental station with the flexible arm	83
Figure 5.4: Experimental PD end point response of the unloaded arm with a target end point position of 45 degrees	89
Figure 5.5: Experimental PD hub position response of the unloaded arm with a target end point position of 45 degrees	89
Figure 5.6: Experimental PD end point response of the flexible arm and 23% load with a target end point position of 45 degrees . . .	90

Figure 5.7:	Experimental PD hub position response of the flexible arm and 23% load with a target end point position of 45 degrees	90
Figure 5.8:	Experimental PD end point response of the flexible arm and 64% load with a target end point position of 45 degrees	91
Figure 5.9:	Experimental PD hub position response of the flexible arm and 64% load with a target end point position of 45 degrees	91
Figure 5.10:	Experimental PD end point response of the unloaded arm with a target end point position of 90 degrees	93
Figure 5.11:	Experimental PD hub position response of the unloaded arm with a target end point position of 90 degrees	93
Figure 5.12:	Experimental PD end point response of the flexible arm and 23% load with a target end point position of 90 degrees	94
Figure 5.13:	Experimental PD hub position response of the flexible arm and 23% load with a target end point position of 90 degrees	94
Figure 5.14:	Experimental PD end point response of the flexible arm and 64% load with a target end point position of 90 degrees	95
Figure 5.15:	Experimental PD hub position response of the flexible arm and 64% load with a target end point position of 90 degrees	95
Figure 5.16:	NLFC first mode gain as a function of hub position	96
Figure 5.17:	Experimental FC end point response of the unloaded arm with a target end point position of 45 degrees	97
Figure 5.18:	Experimental FC hub position response of the unloaded arm with a target end point position of 45 degrees	98

Figure 5.19: Experimental FC end point response of the flexible arm and
23% load with a target end point position of 45 degrees . . . 100

Figure 5.20: Experimental FC hub position response of the flexible arm
and 23% load with a target end point position of 45 degrees . 101

Figure 5.21: Experimental FC end point response of the flexible arm and
64% load with a target end point position of 45 degrees . . . 102

Figure 5.22: Experimental FC hub position response of the flexible arm
and 64% load with a target end point position of 45 degrees . 103

Figure 5.23: Experimental FC end point response of the unloaded arm with
a target end point position of 90 degrees 104

Figure 5.24: Experimental FC hub position response of the unloaded arm
with a target end point position of 90 degrees 105

Figure 5.25: Experimental FC end point response of the flexible arm and
23% load with a target end point position of 90 degrees . . . 106

Figure 5.26: Experimental FC hub position response of the flexible arm
and 23% load with a target end point position of 90 degrees . 107

Figure 5.27: Experimental FC end point response of the flexible arm and
64% load with a target end point position of 90 degrees . . . 109

Figure 5.28: Experimental FC hub position response of the flexible arm
and 64% load with a target end point position of 90 degrees . 110

ACKNOWLEDGMENTS

I would like to thank my friend and advisor Marty Vanderploeg for providing support and encouragement, as well as needed laughs. I would also like to thank Professors Bernard, Flugrad, Pierson, and Huston for their input while serving on my committee.

Many thanks go to my friends and past and present colleagues in 0095E and 0095D, Jim Baustian, Alan Lynch, Alan Hufnagel, Paul Warner, Don Dusenberry, Jeff Dorr, Craig Weiss, Chaeyoun Oh, Terran Boyland, Afshin Mikali, Jim Troy, Todd Teske, Jim Lynch, and Chris Venteicher for providing technical assistance and welcomed diversions. A special thanks goes to my squash and golfing partner Jeff Trom.

I would like to thank my family for their love and support. Finally, a very special thanks goes to my wife, Jill, for her love, support, and diversions during the course of this research.

DESCRIPTION OF NOMENCLATURE

The nomenclature in this dissertation requires a brief explanation. Three types of variables are discussed: scalars, vectors, and matrices. Scalar variables are defined by lower or upper case letters (e.g., a , A). Row and column matrices are defined by a lower case bold letter (e.g., \mathbf{a}). Matrices are defined by an upper case bold letter (e.g., \mathbf{A}). Transposes of vectors or matrices are denoted by a superscript “ T ” (e.g., \mathbf{A}^T). Differentiation with respect to time is denoted by one or more dots (e.g., $\ddot{\mathbf{A}}$). Differentiation with respect to the space variable x is denoted by a prime (e.g., \mathbf{A}').

1. INTRODUCTION

To increase the efficiency of robots, it is useful to make them lighter and faster. However, light robots can be difficult to control due to significant elastic motions. The first research dealing with flexible robots was concerned with robots placed in space. Since it is expensive to launch heavy payloads into space and robots need not support their own weight or payload weight, space-based robots are structurally light. Although control algorithms for these robots are necessarily complex, the need for complexity is lessened somewhat because space-based robots are not subject to any significant gravity fields. Since earth-based robots operate in a strong gravity field, the challenge of controlling flexible earth-based robots is even more difficult than the challenge of controlling space-based robots.

This thesis presents a model of a flexible robot arm that includes gravitational effects. Several algorithms are presented to control the model. An experimental implementation of a flexible robot in a vertical plane is presented with results from various control algorithms.

The objectives of this thesis are to develop control algorithms for a one arm flexible robot in gravity using mathematical models, and to demonstrate their feasibility in a test bed. The primary contribution is the demonstration of accurate, feasible, and stable control algorithms for a flexible robot arm with various payloads in gravity

using no end point position feedback. The feedback to control the arm is obtained from hub position and velocity sensors and strain gages on the arm. The strains are used to determine the magnitudes of the flexible modes.

This thesis includes the following chapters: Chapter 2 reviews the existing work in the area of control of flexible robots. Chapter 3 develops an analytical model of the robot arm. Chapter 4 develops algorithms for controlling the arm and presents numerical results. Chapter 5 presents the experimental test bed and the measured results. Chapter 6 presents conclusions.

2. LITERATURE REVIEW

The pressure to increase productivity has resulted in widespread use of robots on the factory floor. Most of the robots in current use are massive when compared to their payload. One reason for this is to reduce unwanted vibrations due to elastic deformation. However, the large mass of the arm slows the response of the robot. One potential solution is to use larger, more powerful actuators, but this has negative cost and energy implications. A better solution is to use lighter robot arms and design the control algorithm to take into account the flexibility of the arm. This chapter reviews the literature which has focused on the use of manipulators with flexible arms.

In the past few years, many researchers have investigated flexible beams. Concurrently, many researchers have been investigating the control of flexible robots. To develop control algorithms for these systems, several key assumptions are generally made. The robot arm is usually modelled as a Euler-Bernoulli beam with either pinned-free or clamped-free boundary conditions. The Euler-Bernoulli beam model assumes no rotary inertia or shear deformation effects. With few exceptions, gravity is assumed to have no effect on the vibration of the arm.

This literature review concentrates on combined simulated and experimental control results. A selected group of simulation only papers will also be reviewed.

Book [1] gives an introductory overview of the control of flexible robots. After presenting several sources of compliance in a robot, some representative control strategies are presented. Lastly, a bracing strategy is introduced in which the robot arm braces itself against the work piece during final, high accuracy movements.

In a later paper, Book [2] qualitatively summarized the advantages and disadvantages of lighter weight arms. The lighter arms allow higher gross motion speeds, lower cost, improved energy efficiency, but introduce vibrations and static droop which necessitate complicated control and design steps. Bracing the robot against the work piece or a work bench and using secondary actuators for precision work was suggested as a way to gain stability. This would be similar to a person resting their hand on a table while writing.

2.1 Theoretical Studies

This section presents a selection of theoretical studies. One of the pioneering efforts in this area was presented by Book et al. [3]. They investigated a two-arm robot model in which both arms were assumed to be flexible. An Euler-Bernoulli model of the flexible arms was used. Three control laws were developed. Two control laws were based on rigid arm dynamics while the third included flexibility. The control laws were developed using a pole-placement algorithm. These laws resulted in some of the feedback gains being too large to implement. Generally, their methodology was to control the rigid body motion and let the vibration damp out. The controller including the flexibility effects yielded higher torques and could go unstable in certain configurations.

Singh and Schy [4] developed the equations of motion for a three link robot where the last link was assumed to be flexible. The flexibility in both transverse directions was modelled with three clamped-free mode shapes. Modal coupling, gravity, and torsion were ignored. The control law was based on the invertability of the input-output map for large motions and a linear controller for flexible motions. Simulations attained steady state after about nine seconds. Other than nominal end masses resulted in large overshoots and oscillations, and response time doubled to 18 seconds.

Skaar and Tucker [5] presented simulations of a single flexible horizontal robot arm. They used the Euler-Bernoulli beam model to derive the equations of motion. A convolution integral approach to control points on the arm rather than mode shapes was developed. An optimal control with specified end state was developed.

Singh and Schy [6] presented a simulation of a three link robot in which only the final link is flexible. The model did not include gravity effects. Clamped-free mode shapes were used to model the flexible link. They developed a two part control algorithm. The first part was a nonlinear law based on the inversion of the input (torque) to output (joint angles) map. A linear-quadratic control law was used to damp the vibration of the flexible link. The simulated control algorithm yielded good results with a variety of end masses. It was found that better results are achieved overall when the design is based on the largest end mass.

Korolov and Chen [7] presented several simulations of a horizontal flexible robot arm. They constructed a control algorithm that was able to account for variations in natural frequencies. The robot arm remained stable under a variety of different loadings.

Schmitz [8] developed nonlinear equations of motion for a two-link robot using Kanes' method. Gravitational effects were ignored. The first link was rigid and the second was flexible. The second arm was modelled with three clamped-free mode shapes. A proportional-derivative (PD) controller based on the hub angle was shown to be asymptotically stable. Simulations showed a full state linear quadratic regulator (LQR) controller to be better than the PD controller. A drawing of an earth-based horizontal experimental station under construction was shown. To eliminate torsion due to gravitational forces, the end of each arm traveled on an air pad.

Nathan and Singh [9] developed a controller for a two arm robot. Both arms were assumed to be flexible. The control law consisted of two distinct phases. In the first, the joint angles were driven along a trajectory utilizing a proportional-integral-derivative (PID) control law, without regard for the flexible motion of the arms. As the joint angles approached the final states, the controller was switched so that the flexibility was considered. This reduced the vibrations of the arms created by the first phase of the control law. Numerical results showed good trajectory tracking with only small errors introduced when the control was switched to the second phase.

Yeung and Chen [10] presented a single arm flexible robot in both the vertical and horizontal planes. The beam was modelled using assumed modes. They used a sliding mode controller in regulator, ramp, and parabola tracking situations. This method required that the system poles be placed so that payload changes do not drastically affect the results.

Castelazo and Lee [11] presented several simulations of a single horizontal flexible arm modelled under Euler-Bernoulli assumptions with pinned-free mode shapes. They proposed a nonlinear control law in which the damping is varied as a function

of position. In this way, the damping was small at the beginning of the control cycle and increased as the arm approached the target state. As a starting point, a linear-quadratic control was developed. The dominant pole was then moved, resulting in a smaller rise time but larger overshoot. The overshoot was then remedied using the position sensitive damping scheme.

Asada et al. [12] developed the equations of motion for an multiple link horizontal flexible robot. A “virtual link coordinate system” was introduced. In this system, one local coordinate extends from the base of the link to the endpoint of that link. The equations were first developed in the standard coordinate system (where one local coordinate is tangent to the base of the link) and then transformed into the new coordinate system. This choice of coordinate system was said to greatly simplify the equations of motion because the vibration of one link does not affect the other links. Through simulation, they demonstrated a feed forward algorithm to damp vibrations during trajectory following.

Chang and Park [13] presented a theoretical study of a single flexible arm in a vertical plane. They developed equations of motion based on the “equivalent rigid link system.” Euler-Bernoulli assumptions were the basis of the model for the flexible arm. Clamped-free mode shapes were used to model flexibility. Finite element techniques were used to relate general arm deflections to the end point deflection and angle. A computed torque method was used to determine the control input. Simplified actuator dynamics were also included in the model. Simulations demonstrated a stable system with no overshoot.

Yuan and Lin [14] presented a simulation study of a two link flexible robot in the vertical plane. Flexibility was modelled by the assumed modes method. The

quasistatic droop induced by gravity was considered. A two part linear controller was developed. Tracking control was developed for large motions while smaller motion vibrations were reduced using an LQR controller. The LQR was shown to reduce the vibrations of the arms while only slightly degrading the tracking ability of the robot.

Chiou and Shahinpoor [15] developed a hybrid force and position controller for a horizontal two arm flexible robot. One mode shape was used to model the flexibility of each arm. The flexibility of the first arm was found to be dominant over the flexibility of the second arm. This paper indicated that, unlike rigid arm robots, flexible arm robots do tend to become unstable as the force feedback gains are increased.

Choura et al. [16] presented three different beam models of varying complexity. The simplest was used when the hub velocity was low. A feed forward method was developed to eliminate individual modes of vibration. Simulations showed good results for higher modes, but limited success for the lower modes. As indicated by the authors, this technique would need to be used in conjunction with a feedback controller in an actual implementation.

Cetinkunt and Wu [17] presented a theoretical study of a horizontal single flexible arm robot. An Euler-Bernoulli model was used in conjunction with the assumed modes method. A lattice filter was used for parameter identification in a predictive adaptive control scheme. The simulation results showed good responses as long as the frequency of the reference response was below the first natural frequency of the arm.

2.2 Theoretical and Experimental Studies

Fukuda and Kuribayashi [18] presented a horizontal two arm robot in which the first arm was rigid and the second was flexible. The assumed modes method was used in developing the equations of motion. In the experimental system, strain gages were used to estimate the magnitudes of each mode shape. A fault tolerant controller was also developed. The flexible body controller yielded improved results over a rigid body controller.

Cannon and Schmitz [19] presented a single flexible arm robot operating in the horizontal plane. The flexible arm was modelled using an Euler-Bernoulli model with pinned-free mode shapes. The parameters in the theoretical model were determined experimentally. A discretized linear quadratic controller was used to experimentally reposition a flexible arm. The digital controller and compensator operated at 50 Hz. The arm had a fundamental frequency of 0.5 Hz. The controller was able to reposition the end point of the arm 10 cm (approximately 10 degrees) in 0.7 seconds. An optical sensor was used to determine the tip location in the feedback loop.

Fukuda [20] presented a horizontal two arm flexible robot modelled using the assumed modes method. The experimental robot arms had fundamental frequencies of 4.1 and 1.1 Hz respectively. Three modes were used to model each beam. The steady state solution was reached in approximately ten seconds. The effects of end masses were not considered.

Hastings and Book [21] implemented a horizontal single arm robot. The flexibility of the arm was modelled with two clamped-free mode shapes. The first two natural frequencies were 2.0 and 13.5 Hz. Strain gages were placed at the base and midpoint of the arm. The magnitudes of the mode shapes were determined from

these strains. Results for runs of unknown joint angle magnitude were given. Gains designed for no payload and a known, but unspecified payload were used in the control law. The unloaded case exhibited no overshoot. The case designed for the known payload mass exhibited a small amount of overshoot while the case of four times the known mass using the previous gains resulted in significant overshoot and residual oscillation.

Sakawa et al. [22] presented a horizontal single flexible arm robot modelled with the Euler-Bernoulli assumptions. Strain gages were used for vibration measurement. A linear-quadratic approach was taken to determine the controller gains. The results for varying gains showed good target state, with some overshoot. For the 0.6 Hz arm, the settling times were from about three seconds to 5.5 seconds.

Rovner and Cannon [23], using the same robot arm as Cannon and Schmitz [19], presented a horizontal plane robot arm with two different end masses. They developed an adaptive control strategy. The strategy was to develop a learning sequence and observe the time response. By assuming a certain robot arm model, the model parameters could be determined and the linear-quadratic control algorithm “tuned” for the best results. The control algorithms using the identified parameters were slightly degraded from those using the known values.

Chalhoub and Ulsoy [24] presented a three link robot in which only the third link was assumed to be flexible. Static deflection of the flexible arm due to gravity was not considered. Simulation results in which the flexible arm was modelled with two modes in each direction were presented. However, the control assumed only one mode. Thus, observation and control spillover effects were studied. Numerical results indicated that the second mode would become unstable in the absence of structural

damping. However, with a very small amount of structural damping, the second mode was marginally stable. Experiments were conducted for flexible motion in the horizontal plane. The results showed a marked improvement in settling time and maximum deflection when the controller included the effects of flexible motion.

Kotnik et al. [25] also developed a single arm horizontal robot. Three linear control laws were developed. The laws were based on end point position feedback, full state with observer feedback, and end point acceleration feedback, respectively. Experimental results showed that only the full state linear-quadratic regulator did not have steady state errors. However, even with full state feedback, it did oscillate about the target point. The advantage of the acceleration feedback was that it did not require the use of a camera in the feedback loop. For a 25 degree slew angle, this scheme settled in approximately 2.5 seconds and exhibited a steady state error of two to three degrees with significant overshoot.

Chang and Kirkland [26] presented the experimental extension of Chang and Park's work [13] along with some additional theoretical work. A simplified control algorithm was used in the experimental station. A potentiometer was used to measure the hub position. Both analog and digital filters were used to condition the position signal. A velocity estimator was used instead of measuring the hub angular velocity. Strain gages were used to measure the flexibility of the arm. The experimental results gave less overshoot, but longer settling times than the simulations indicated for the 2 Hz arm. A control algorithm based on rigid body assumptions was also constructed. The controller that included flexibility effects required less torque than the rigid body controller.

Singer and Seering [27] presented a method of modifying or “shaping” the desired trajectory so that residual vibrations of a flexible arm were eliminated. The method was based on convolving impulses that remove residual vibrations with the actual reference trajectory. The method was demonstrated on a single arm system and a coupled two arm system. The experimental system had fundamental frequencies of 2.45 and 6.4 Hz. Residual vibrations were greatly reduced, although rise time was greater than response times for a non-shaped command response. In real time tracking problems, the 2.45 Hz system showed a shaped input that was approximately 0.15 seconds behind the non-shaped input. However, the residual vibrations of the shaped command response were very small.

Oakley and Barratt [28] presented a horizontal two arm flexible robot. The flexibility was modelled with the assumed modes method. A nominal linear quadratic controller with an observer was designed for the robot. This controller was then modified so that additional time and frequency response constraints would be met. The new controller was appended to the LQG controller as a finite impulse response digital filter in which the weightings were obtained by accounting for the additional constraints. Experimental results showed the augmented controller had faster rise times and better trajectory following compared to the nominal LQG controller.

Park and Asada [29] developed and implemented a torque transmission mechanism for a flexible horizontal single arm robot. The torque application point was effectively moved from the base of the arm to a point well out on the arm. The dynamics of the arm was demonstrated to change substantially as the torque application point was moved outward. The flexible arm was converted into a minimum phase system. The experiments confirmed the minimum phase behavior. With this mod-

ification, design of control algorithms was simplified. Root locus diagrams showed increased stability as the torque application point was moved outward.

Chiou and Shahinpoor [30] extended and experimentally implemented their previous numerical study [15]. A one link flexible arm was implemented with various force feedback controllers. It was found that the impact of the end of the arm against the work piece had a profound destabilizing effect. The delay introduced by the sensors and actuator also had destabilizing effects.

Schoenwald et al. [31] developed and implemented a minimum time optimal controller for a two arm horizontal flexible robot. The arms were modelled using finite element methods. The open loop control law using only the torque curves from the simulated model resulted in large errors. A feedforward design was then implemented in which the torque from the model was modified based on the measured state. A starting point for the feedforward gains was found by employing linear-quadratic control concepts. The gains were then tuned by hand on the actual system. The highest gains were placed on the joint angles and velocities. Placing higher gains on the elastic deflection gains resulted in an unstable system.

3. ANALYTICAL ROBOT MODEL

This chapter derives the equations of motion for a flexible arm robot operating in a gravity field. The robot arm is assumed to move in a vertical plane. A diagram of the robot is given in Figure 3.1. The model includes an end mass that represents a payload and end effector.

Energy methods will be used to derive nonlinear and linearized equations of motion for the flexible arm system. The following sections will develop the kinetic and potential energies.

3.1 Kinetic Energy

The kinetic energy of the system can be written as the sum of several parts. The kinetic energy associated with the mass of the base is:

$$T_s = \frac{1}{2} J \dot{\theta}^2 \quad (3.1)$$

where J is the moment of inertia of the mass of the base about the pivot point of the arm. The kinetic energy associated with the flexibility of the arm is given by:

$$T_b = \int \frac{1}{2} \dot{\mathbf{r}}_p \cdot \dot{\mathbf{r}}_p \, dm \quad (3.2)$$

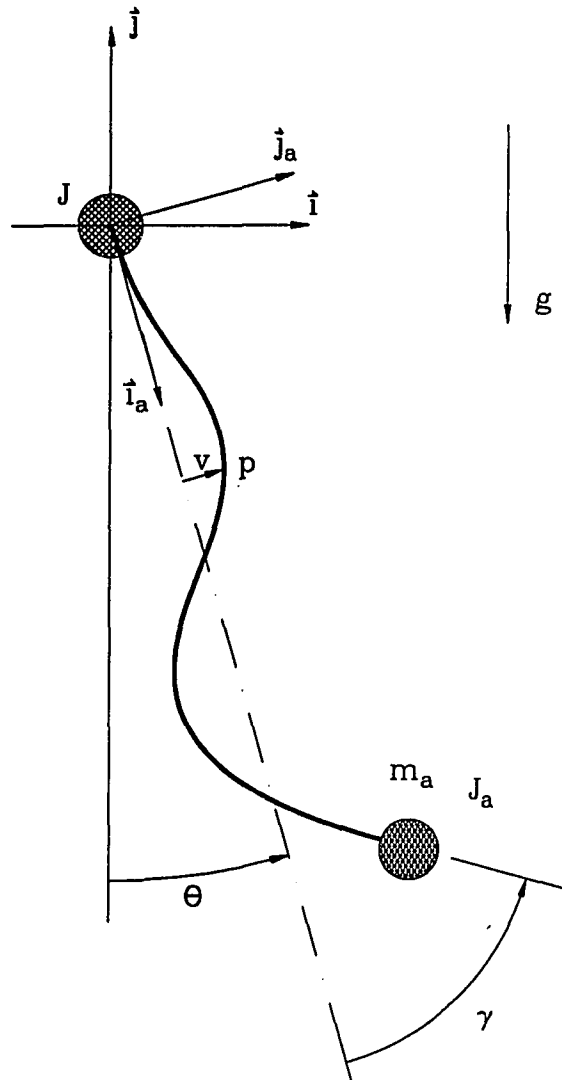


Figure 3.1: Diagram of flexible arm and end mass

By assuming the density of the arm varies only with distance along the arm, x , an infinitesimal mass may be simplified as:

$$dm = \rho A dx \quad (3.3)$$

The generalized vector, \mathbf{r}_p , to any point p on the arm is:

$$\mathbf{r}_p = (x \sin \theta + v \cos \theta) \vec{i} + (v \sin \theta - x \cos \theta) \vec{j} \quad (3.4)$$

where \vec{i} and \vec{j} are fixed unit vectors. By assuming the arm does not shorten as it deflects, differentiation of equation 3.4 with respect to time gives:

$$\dot{\mathbf{r}}_p = (x \cos \theta \dot{\theta} - v \sin \theta \dot{\theta} + \dot{v} \cos \theta) \vec{i} + (x \sin \theta \dot{\theta} + v \cos \theta \dot{\theta} + \dot{v} \sin \theta) \vec{j} \quad (3.5)$$

Substituting equations 3.3 and 3.5 into equation 3.2 results in:

$$T_b = \int_0^l \frac{\rho A}{2} (\dot{v}^2 + x^2 \dot{\theta}^2 + v^2 \dot{\theta}^2 + 2x\dot{v}\dot{\theta}) dx \quad (3.6)$$

The kinetic energy of the end mass is:

$$T_a = \frac{1}{2} m_a \dot{\mathbf{r}}_l \cdot \dot{\mathbf{r}}_l + \frac{1}{2} J_a (\dot{\gamma}_l + \dot{\theta})^2 \quad (3.7)$$

An approximation for γ_l can be found:

$$\gamma_l \approx \left. \frac{\partial v}{\partial x} \right|_l = v'_l \quad (3.8)$$

Therefore, the kinetic energy due to the end mass can be written as:

$$T_a = \frac{1}{2} m_a (\dot{v}_l^2 + l^2 \dot{\theta}^2 + v_l^2 \dot{\theta}^2 + 2l\dot{v}_l\dot{\theta}) + \frac{1}{2} J_a \left(\dot{\theta} + \frac{d}{dt} v'_l \right)^2 \quad (3.9)$$

Thus, the kinetic energy of the arm with end mass is:

$$T = T_s + T_b + T_a \quad (3.10)$$

$$T = \frac{1}{2} J \dot{\theta}^2 + \int_0^l \frac{\rho A}{2} (\dot{v}^2 + x^2 \dot{\theta}^2 + v^2 \dot{\theta}^2 + 2x\dot{v}\dot{\theta}) dx + \frac{1}{2} m_a (\dot{v}_l^2 + l^2 \dot{\theta}^2 + v_l^2 \dot{\theta}^2 + 2l\dot{v}_l\dot{\theta}) + \frac{1}{2} J_a \left(\dot{\theta} + \frac{d}{dt} v'_l \right)^2 \quad (3.11)$$

3.2 Potential Energy

The potential energy of the system also can be written as the sum of several parts. The elastic energy of the flexible arm is given by the Euler-Bernoulli beam model as:

$$V_e = \int_0^l \frac{EI}{2} (v'')^2 dx \quad (3.12)$$

The gravitational energy is given by:

$$V_g = \int gy \, dm \quad (3.13)$$

where y is measured along the fixed unit vector \vec{j} . By assuming the arm does not shorten as it deflects and density varies only with x , equation 3.13 can be rewritten as:

$$V_g = \int_0^l \rho Ag (v \sin \theta - x \cos \theta) dx \quad (3.14)$$

The potential energy of the end mass is due to gravity and is given by:

$$V_a = m_{ag} (v_l \sin \theta - l \cos \theta) \quad (3.15)$$

Thus, the potential energy of the flexible arm system is:

$$V = V_e + V_g + V_a \quad (3.16)$$

$$V = \int_0^l \frac{EI}{2} (v'')^2 dx + \int_0^l \rho Ag (v \sin \theta - x \cos \theta) dx + m_{ag} (v_l \sin \theta - l \cos \theta) \quad (3.17)$$

3.3 Assumed Modes

The displacement v , which is a function of time, can be thought of as the sum of the product of an infinite number of time varying coordinates and spatial vary-

ing coordinates. This is known as the assumed modes model. It can be written mathematically as:

$$v(x, t) = \sum_{i=1}^{\infty} d_i(t) \psi_i(x) \quad (3.18)$$

where $\psi_i(x)$ are the assumed modes. The infinite series is truncated to yield a finite order system:

$$v(x, t) = \sum_{i=1}^n d_i(t) \psi_i(x) = \mathbf{d}^T \boldsymbol{\psi} \quad (3.19)$$

By substituting equation 3.19 into equation 3.11 and taking the appropriate derivatives, the kinetic energy of the system can be rewritten as:

$$\begin{aligned} T = & \int_0^l \frac{\rho A}{2} \left(\dot{\mathbf{d}}^T \boldsymbol{\Psi} \dot{\mathbf{d}} + x^2 \dot{\theta}^2 + \mathbf{d}^T \boldsymbol{\Psi} \mathbf{d} \dot{\theta}^2 + 2x \dot{\mathbf{d}}^T \boldsymbol{\psi} \dot{\theta} \right) dx + \frac{1}{2} J \dot{\theta}^2 \\ & \frac{1}{2} m_a \left(\dot{\mathbf{d}}^T \boldsymbol{\Psi}_l \dot{\mathbf{d}} + l^2 \dot{\theta}^2 + \mathbf{d}^T \boldsymbol{\Psi}_l \mathbf{d} \dot{\theta}^2 + 2l \dot{\mathbf{d}}^T \boldsymbol{\psi}_l \dot{\theta} \right) dx + \\ & \frac{1}{2} J_a \left(\dot{\theta}^2 + 2\dot{\theta} \dot{\mathbf{d}}^T \boldsymbol{\psi}'_l + \dot{\mathbf{d}}^T \boldsymbol{\Psi}'_l \dot{\mathbf{d}} \right) \end{aligned} \quad (3.20)$$

Where

$$\boldsymbol{\Psi} = \boldsymbol{\psi} \boldsymbol{\psi}^T \quad (3.21)$$

By substituting equation 3.19 into equation 3.17 and taking the appropriate derivatives, the potential energy of the system can be rewritten as:

$$\begin{aligned} V = & \int_0^l \frac{EI}{2} \mathbf{d}^T \boldsymbol{\Upsilon} \mathbf{d} dx + \int_0^l \rho A g \left(\mathbf{d}^T \boldsymbol{\psi} \sin \theta - x \cos \theta \right) dx + \\ & m_a g \left(\mathbf{d}^T \boldsymbol{\psi}_l \sin \theta - l \cos \theta \right) \end{aligned} \quad (3.22)$$

Where

$$\boldsymbol{\Upsilon} = \boldsymbol{\psi}'' \boldsymbol{\psi}''^T \quad (3.23)$$

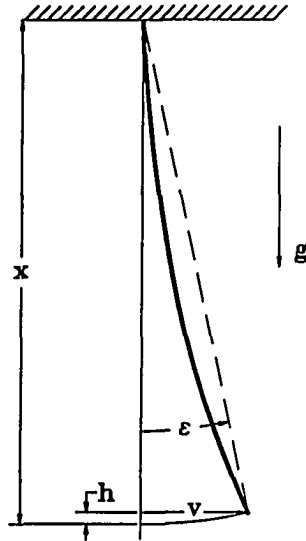


Figure 3.2: Diagram showing shortening effects due to transverse displacement

3.4 Gravitational Correction Term

One additional effect must be included to accurately model the flexible arm. The potential energy derived from vertical displacements as the arm deflects laterally induces additional potential energy not accounted for in equation 3.14 [32]. This effect is illustrated in Figure 3.2. This additional term can be written as:

$$V_g = \int hg \cos \theta \, dm \quad (3.24)$$

This effect is assumed to be significant only for the first mode. Since the energy required to laterally deflect the arm a given amount increases significantly in higher order mode shapes, the longitudinal deflection due to these modes is considered to be small. For the first mode, h can be approximated by the following:

$$h \approx x(1 - \cos \epsilon) \approx x \left(1 - 1 + \frac{\epsilon^2}{2} \right) = \frac{x\epsilon^2}{2} \quad (3.25)$$

Where ϵ is:

$$\tan \epsilon = \frac{v}{x} \quad (3.26)$$

For small ϵ ,

$$\epsilon \approx \frac{v}{x} \quad (3.27)$$

This results in:

$$h \approx \frac{v^2}{2x} \quad (3.28)$$

The kinetic energy due to this effect depends on:

$$\dot{h} = \frac{1}{2} \left(\frac{2v\dot{v}}{x} - \frac{v^2\dot{x}}{x^2} \right) \quad (3.29)$$

Both of the terms in equation 3.29 are small. Thus, the kinetic energy contribution due to this effect is neglected. The potential energy due to vertical displacements as the arm deflects can be estimated as:

$$V_g = \int_0^l \frac{\rho Ag v^2}{2x} \cos \theta dx \quad (3.30)$$

This expression is only valid for the first mode. Therefore, let:

$$v = \mathbf{d}^T \boldsymbol{\xi} \quad (3.31)$$

where $\boldsymbol{\xi}$ is defined as:

$$\boldsymbol{\xi}^T = \left(\psi_1 \quad 0 \quad \dots \quad 0 \right) \quad (3.32)$$

With the addition of the above component, the potential energy for the flexible arm system is:

$$\begin{aligned} V = & \int_0^l \frac{EI}{2} \mathbf{d}^T \boldsymbol{\gamma} \mathbf{d} dx + \int_0^l \rho Ag \left(\mathbf{d}^T \boldsymbol{\psi} \sin \theta - x \cos \theta \right) dx + \\ & \int_0^l \frac{\rho Ag}{2x} \mathbf{d}^T \boldsymbol{\Xi} \mathbf{d} \cos \theta dx + m_{ag} \left(\mathbf{d}^T \boldsymbol{\psi}_l \sin \theta - l \cos \theta \right) + \\ & \frac{m_{ag}}{2l} \mathbf{d}^T \boldsymbol{\Xi}_l \mathbf{d} \cos \theta \end{aligned} \quad (3.33)$$

where Ξ is defined as:

$$\Xi = \xi \xi^T \quad (3.34)$$

3.5 Equations of Motion

With the kinetic and potential energies expressed above, the equations of motion of the system may be obtained by using Lagrange's equation:

$$\frac{d}{dt} \left(\frac{\partial T}{\partial \dot{\mathbf{q}}} \right) - \frac{\partial T}{\partial \mathbf{q}} + \frac{\partial V}{\partial \mathbf{q}} = \mathbf{f} \quad (3.35)$$

where

$$\mathbf{q}^T = \left(\theta \quad d_1 \quad d_2 \quad \dots \quad d_n \right) \quad (3.36)$$

and

$$\mathbf{f}^T = \left(M \quad 0 \quad \dots \quad 0 \right) \quad (3.37)$$

where M is the moment applied at the hub. After taking the derivatives and collecting terms, the equations of motion of the flexible arm and end mass system are:

$$\begin{bmatrix} M \\ \mathbf{0} \end{bmatrix} = \begin{bmatrix} \int_0^l \rho A x^2 dx + J + m_a l^2 + J_a & \int_0^l \rho A x \psi^T dx + m_a l \psi_l^T + J_a \psi_l'^T \\ \int_0^l \rho A x \psi dx + m_a l \psi_l + J_a \psi_l' & \int_0^l \rho A \Psi dx + m_a \Psi_l + J_a \Psi_l' \end{bmatrix} \begin{bmatrix} \ddot{\theta} \\ \ddot{\mathbf{d}} \end{bmatrix} \\ + \begin{bmatrix} 0 & \mathbf{0} \\ \mathbf{0} & \int_0^l EI \Upsilon dx \end{bmatrix} \begin{bmatrix} \theta \\ \mathbf{d} \end{bmatrix} \\ + \begin{bmatrix} \int_0^l \rho A (\ddot{\theta} \mathbf{d}^T \Psi \mathbf{d} + 2\dot{\theta} \dot{\mathbf{d}}^T \Psi \mathbf{d}) dx + \int_0^l \rho A g (\mathbf{d}^T \psi \cos \theta + x \sin \theta) dx \\ - \int_0^l \rho A \dot{\theta}^2 \Psi \mathbf{d} dx + \int_0^l \rho A g \psi \sin \theta dx \end{bmatrix}$$

$$\begin{aligned}
& + m_a \left[\begin{array}{c} \ddot{\theta} \mathbf{d}^T \Psi_l \mathbf{d} + 2\dot{\theta} \dot{\mathbf{d}}^T \Psi_l \mathbf{d} + g (\mathbf{d}^T \psi_l \cos \theta + l \sin \theta) \\ -\dot{\theta}^2 \Psi_l \mathbf{d} + g \psi_l \sin \theta \end{array} \right] \\
& + g \left[\begin{array}{c} -\int_0^l \frac{\rho A}{2x} \mathbf{d}^T \Xi \mathbf{d} \sin \theta dx - \frac{m_a}{2l} \mathbf{d}^T \Xi_l \mathbf{d} \sin \theta \\ \int_0^l \frac{\rho A}{x} \Xi \mathbf{d} \cos \theta dx + \frac{m_a}{l} \Xi_l \mathbf{d} \cos \theta \end{array} \right] \quad (3.38)
\end{aligned}$$

3.6 Boundary Conditions

At $x = 0$, the arm is clamped. Thus, the geometric boundary conditions are:

$$v(0, t) = 0 \quad (3.39)$$

$$v'(0, t) = 0 \quad (3.40)$$

Applying moment and shear relations to the free end of the arm gives the natural boundary equations. These are found to be:

$$EIv'' + J_a \left(\ddot{\theta} + \frac{d^2}{dt^2} (v')_l \right) = 0 \quad (3.41)$$

$$(EIv'')'_l + m_a (v\dot{\theta}^2 - g \sin \theta - \ddot{v} - l\ddot{\theta})_l = 0 \quad (3.42)$$

Substituting the assumed modes model into the above equations results in:

$$\psi(0) = 0 \quad (3.43)$$

$$\psi'(0) = 0 \quad (3.44)$$

$$EI \mathbf{d}^T \psi''(l) + J_a \left(\ddot{\theta} + \ddot{\mathbf{d}}^T \psi'(l) \right) = 0 \quad (3.45)$$

$$EI \mathbf{d}^T \psi'''(l) + m_a \left(\mathbf{d}^T \psi(l) \dot{\theta}^2 - g \sin \theta - \ddot{\mathbf{d}}^T \psi(l) - l\ddot{\theta} \right) = 0 \quad (3.46)$$

3.7 Linearization

The nonlinear vector equation of the form $g(\ddot{\mathbf{q}}, \dot{\mathbf{q}}, \mathbf{q}, f, t) = \mathbf{0}$ may be linearized about any operating point $\mathbf{q}^* = (\ddot{\mathbf{q}}_0, \dot{\mathbf{q}}_0, \mathbf{q}_0, f_0, t)$ by the following:

$$\delta \mathbf{g} = \left. \frac{\partial \mathbf{g}}{\partial \ddot{\mathbf{q}}} \right|_{\mathbf{q}^*} \delta \ddot{\mathbf{q}} + \left. \frac{\partial \mathbf{g}}{\partial \dot{\mathbf{q}}} \right|_{\mathbf{q}^*} \delta \dot{\mathbf{q}} + \left. \frac{\partial \mathbf{g}}{\partial \mathbf{q}} \right|_{\mathbf{q}^*} \delta \mathbf{q} + \left. \frac{\partial \mathbf{g}}{\partial f} \right|_{\mathbf{q}^*} \delta f = \mathbf{0} \quad (3.47)$$

This can also be expressed as the following:

$$\mathbf{M}_l \ddot{\mathbf{q}}_l + \mathbf{C}_l \dot{\mathbf{q}}_l + \mathbf{K}_l \mathbf{q}_l = -\mathbf{f}_l f_l \quad (3.48)$$

where \mathbf{M}_l , \mathbf{C}_l , and \mathbf{K}_l are the linearized mass, damping, and stiffness matrices, respectively. Thus, the linearized equations of motion are:

$$\begin{aligned} \begin{bmatrix} M \\ \mathbf{0} \end{bmatrix} = & \begin{bmatrix} \int_0^l \rho A x^2 dx + J + m_a l^2 & \int_0^l \rho A x \psi^T dx + m_a l \psi_l^T + J_a \psi_l'^T \\ + J_a + \left. \frac{\partial p_1}{\partial \theta} \right|_{\mathbf{q}^*} & \int_0^l \rho A \Psi dx + m_a \Psi_l + J_a \Psi_l' \end{bmatrix} \begin{bmatrix} \Delta \ddot{\theta} \\ \Delta \ddot{d} \end{bmatrix} \\ & + \begin{bmatrix} \left. \frac{\partial p_1}{\partial \theta} \right|_{\mathbf{q}^*} & \left. \frac{\partial p_1}{\partial d} \right|_{\mathbf{q}^*} \\ \left. \frac{\partial p_2}{\partial \theta} \right|_{\mathbf{q}^*} & \mathbf{0} \end{bmatrix} \begin{bmatrix} \Delta \dot{\theta} \\ \Delta \dot{d} \end{bmatrix} \\ & + \begin{bmatrix} \left. \frac{\partial p_1}{\partial \theta} \right|_{\mathbf{q}^*} & \left. \frac{\partial p_1}{\partial d} \right|_{\mathbf{q}^*} \\ \left. \frac{\partial p_2}{\partial \theta} \right|_{\mathbf{q}^*} & \int_0^l E I \Upsilon dx + \left. \frac{\partial p_2}{\partial d} \right|_{\mathbf{q}^*} \end{bmatrix} \begin{bmatrix} \Delta \theta \\ \Delta d \end{bmatrix} \quad (3.49) \end{aligned}$$

where p_1 and p_2 are defined from equation 3.38 to be:

$$\begin{aligned}
 \begin{bmatrix} p_1 \\ p_2 \end{bmatrix} &= \\
 &\begin{bmatrix} \int_0^l \rho A (\ddot{\theta} \mathbf{d}^T \Psi \mathbf{d} + 2\dot{\theta} \dot{\mathbf{d}}^T \Psi \mathbf{d}) dx + \int_0^l \rho A g (\mathbf{d}^T \psi \cos \theta + x \sin \theta) dx \\ - \int_0^l \rho A \dot{\theta}^2 \Psi \mathbf{d} dx + \int_0^l \rho A g \psi \sin \theta dx \end{bmatrix} \\
 &+ m_a \begin{bmatrix} \ddot{\theta} \mathbf{d}^T \Psi_l \mathbf{d} + 2\dot{\theta} \dot{\mathbf{d}}^T \Psi_l \mathbf{d} + g (\mathbf{d}^T \psi_l \cos \theta + l \sin \theta) \\ - \dot{\theta}^2 \Psi_l \mathbf{d} + g \psi_l \sin \theta \end{bmatrix} \\
 &+ g \begin{bmatrix} - \int_0^l \frac{\rho A}{2x} \mathbf{d}^T \Lambda \mathbf{d} \sin \theta dx - \frac{m_a}{2l} \mathbf{d}^T \Lambda_l \mathbf{d} \sin \theta \\ \int_0^l \frac{\rho A}{x} \Lambda \mathbf{d} \cos \theta dx + \frac{m_a}{l} \Lambda_l \mathbf{d} \cos \theta \end{bmatrix} \quad (3.50)
 \end{aligned}$$

The non-zero partial derivatives are:

$$\frac{\partial p_1}{\partial \theta} = \int_0^l \rho A \mathbf{d}^T \Psi \mathbf{d} dx + m_a \mathbf{d}^T \Psi_l \mathbf{d} \quad (3.51)$$

$$\frac{\partial p_1}{\partial \dot{\theta}} = \int_0^l 2\rho A \dot{\mathbf{d}}^T \Psi \mathbf{d} dx + 2m_a \dot{\mathbf{d}}^T \Psi_l \mathbf{d} \quad (3.52)$$

$$\frac{\partial p_1}{\partial \dot{\mathbf{d}}} = \int_0^l 2\rho A \dot{\theta} \mathbf{d}^T \Psi dx + 2m_a \dot{\theta} \mathbf{d}^T \Psi_l \quad (3.53)$$

$$\frac{\partial p_2}{\partial \dot{\mathbf{d}}} = - \int_0^l 2\rho A \dot{\theta} \Psi \mathbf{d} dx - 2m_a \dot{\theta} \Psi_l \mathbf{d} \quad (3.54)$$

$$\begin{aligned}
 \frac{\partial p_1}{\partial \theta} &= \int_0^l \rho A g (-\psi^T \mathbf{d} \sin \theta + x \cos \theta) dx \\
 &+ m_a g (-\psi_l^T \mathbf{d} \sin \theta + l \cos \theta) \\
 &+ g \left(- \int_0^l \frac{\rho A}{2x} \mathbf{d}^T \Upsilon \mathbf{d} \cos \theta dx - \frac{m_a}{2l} \mathbf{d}^T \Upsilon_l \mathbf{d} \cos \theta \right) \quad (3.55)
 \end{aligned}$$

$$\begin{aligned}
 \frac{\partial p_1}{\partial \mathbf{d}} &= \int_0^l \rho A (2\ddot{\theta} \mathbf{d}^T \Psi + 2\dot{\theta} \dot{\mathbf{d}}^T \Psi) dx + \int_0^l \rho A g \psi^T \cos \theta dx \\
 &+ m_a (2\ddot{\theta} \mathbf{d}^T \Psi_l + 2\dot{\theta} \dot{\mathbf{d}}^T \Psi_l + g \psi_l^T \cos \theta) \\
 &+ g \left(- \int_0^l \frac{\rho A}{x} \mathbf{d}^T \Upsilon \sin \theta dx - \frac{m_a}{l} \mathbf{d}^T \Upsilon_l \sin \theta \right) \quad (3.56)
 \end{aligned}$$

$$\begin{aligned} \frac{\partial p_2}{\partial \theta} &= \int_0^l \rho A g \psi \cos \theta \, dx + m_a g \psi_l \cos \theta \\ &\quad + g \left(- \int_0^l \frac{\rho A}{x} \mathcal{R} d \sin \theta \, dx - \frac{m_a}{l} \mathcal{R}_l d \sin \theta \right) \end{aligned} \quad (3.57)$$

$$\begin{aligned} \frac{\partial p_2}{\partial d} &= - \int_0^l \rho A \dot{\theta}^2 \Psi \, dx - m_a \dot{\theta}^2 \Psi_l \\ &\quad + g \left(\int_0^l \frac{\rho A}{x} \mathcal{R} \cos \theta \, dx + \frac{m_a}{l} \mathcal{R}_l \cos \theta \right) \end{aligned} \quad (3.58)$$

With the equations of motion linearized, the boundary conditions given by equations 3.43 through 3.46 should also be linearized. The geometric boundary conditions 3.43 and 3.44 are already linear. However, the natural boundary conditions are not. The procedure to linearize the boundary conditions is again given by equation 3.47. Thus, equation 3.45 can be linearized to:

$$\left[J_a \mid J_a (\psi'_l)^T \right] \begin{bmatrix} \Delta \bar{\theta} \\ \Delta \bar{d} \end{bmatrix} + \left[0 \mid EI (\psi''_l)^T \right] \begin{bmatrix} \Delta \theta \\ \Delta d \end{bmatrix} = 0 \quad (3.59)$$

The useful portion of the above equation deals with the time varying coordinates of the beam which can be written as:

$$J_a (\psi'_l)^T \Delta \bar{d} + EI (\psi''_l)^T \Delta d = 0 \quad (3.60)$$

By assuming that the time varying coordinates are harmonic, i.e.

$$\Delta d_i = c \sin \omega_i t + e \cos \omega_i t \quad (3.61)$$

$$\Delta \dot{d}_i = c \omega_i \cos \omega_i t - e \omega_i \sin \omega_i t \quad (3.62)$$

$$\Delta \ddot{d}_i = -c \omega_i^2 \sin \omega_i t - e \omega_i^2 \cos \omega_i t \quad (3.63)$$

and that the assumed mode shapes are orthogonal gives:

$$EI \psi''_i(l) - J_a \omega_i^2 \psi'_i(l) = 0 \quad (3.64)$$

Linearizing the boundary condition as given by equation 3.46 gives:

$$\begin{aligned} & \left[-m_a l \mid -m_a \psi_l^T \right] \begin{bmatrix} \frac{\Delta \ddot{\theta}}{\Delta \ddot{d}} \end{bmatrix} + \left[2m_a \dot{\theta} \psi_l^T d \mid 0 \right] \begin{bmatrix} \frac{\Delta \dot{\theta}}{\Delta \dot{d}} \end{bmatrix} \\ & + \left[-m_a g \cos \theta \mid EI (\psi_l''')^T + m_a \dot{\theta}^2 \psi_l^T \right] \begin{bmatrix} \frac{\Delta \theta}{\Delta d} \end{bmatrix} = 0 \quad (3.65) \end{aligned}$$

Evaluating equation 3.65 at $\dot{\theta} = 0$ gives:

$$-m_a \psi_l^T \Delta \ddot{d} + EI (\psi_l''')^T \Delta d = 0 \quad (3.66)$$

By again assuming Δd is harmonic and the assumed mode shapes are orthogonal yields:

$$m_a \omega_i^2 \psi_i(l) + EI \psi_i'''(l) = 0 \quad (3.67)$$

Thus, the boundary conditions for the robot arm with an end mass are:

$$\psi_i(0) = 0 \quad (3.68)$$

$$\psi_i'(0) = 0 \quad (3.69)$$

$$EI \psi_i''(l) - J_a \omega_i^2 \psi_i'(l) = 0 \quad (3.70)$$

$$m_a \omega_i^2 \psi_i(l) + EI \psi_i'''(l) = 0 \quad (3.71)$$

3.8 Assumed Mode Shapes

The mode shapes used in this thesis are the normal modes of a cantilever beam with an end mass. Previous studies have shown that these mode shapes give good results over a broad range of end masses and arm lengths [32]. They are represented by:

$$\psi_i(x) = C_{1,i} \sin(\lambda_i x) + C_{2,i} \cos(\lambda_i x) + C_{3,i} \sinh(\lambda_i x) + C_{4,i} \cosh(\lambda_i x) \quad (3.72)$$

Substituting these assumed mode shapes into the geometric boundary conditions, equations 3.68 and 3.69, results in the following relationships:

$$C_{2,i} + C_{4,i} = 0 \quad (3.73)$$

$$C_{1,i} + C_{3,i} = 0 \quad (3.74)$$

After substituting the mode shapes into the first natural boundary condition, equation 3.70, the following expression relating $C_{1,i}$ and $C_{2,i}$ can be obtained:

$$\frac{C_{1,i}}{C_{2,i}} = \frac{-\cos(\lambda_i l) - \cosh(\lambda_i l) + \left(\frac{J_a \omega_i^2}{EI \lambda_i}\right) (\sin(\lambda_i l) + \sinh(\lambda_i l))}{\sin(\lambda_i l) + \sinh(\lambda_i l) + \left(\frac{J_a \omega_i^2}{EI \lambda_i}\right) (\cos(\lambda_i l) - \cosh(\lambda_i l))} \quad (3.75)$$

Similar substitutions into the second natural boundary condition result in:

$$\frac{C_{1,i}}{C_{2,i}} = \frac{-\sin(\lambda_i l) + \sinh(\lambda_i l) + \left(\frac{m_a \omega_i^2}{EI \lambda_i^3}\right) (-\cos(\lambda_i l) + \cosh(\lambda_i l))}{-\cos(\lambda_i l) - \cosh(\lambda_i l) + \left(\frac{m_a \omega_i^2}{EI \lambda_i^3}\right) (\sin(\lambda_i l) - \sinh(\lambda_i l))} \quad (3.76)$$

By setting equations 3.75 and 3.76 equal, a characteristic equation can be developed. In developing this equation, it is useful to recall that the partial differential equation governing the transverse vibrations of the beam have the form

$$y''''(x) - \beta^4 y(x) = 0 \quad (3.77)$$

Thus, the eigenvalue solution, which relates λ_i to ω_i , yields:

$$\lambda_i^4 = \frac{\rho A \omega_i^2}{EI} \quad (3.78)$$

The resultant characteristic equation is:

$$\begin{aligned} & \frac{1}{\lambda_i l} \left[1 + \frac{1}{\cos(\lambda_i l) \cosh(\lambda_i l)} \right] \\ & - \eta (\lambda_i l)^2 [\tan(\lambda_i l) + \tanh(\lambda_i l)] \\ & + \beta [\tanh(\lambda_i l) - \tan(\lambda_i l)] \\ & + \beta \eta (\lambda_i l)^3 \left[\frac{1}{\cos(\lambda_i l) \cosh(\lambda_i l)} - 1 \right] = 0 \end{aligned} \quad (3.79)$$

where β and η are defined to be:

$$\beta = \frac{ma}{\rho Al} \quad (3.80)$$

$$\eta = \frac{Ja}{\rho Al^3} \quad (3.81)$$

The characteristic equation must be solved for each beam and end mass combination under consideration. After it is solved, the dependent set of equations can be solved to obtain the constants $C_{1,i}$ through $C_{4,i}$. Since the equations are underdetermined, $C_{1,i}$ is set to 1 and the other three constants are solved.

3.9 Static Equilibrium

Since the main thrust of this work is to develop and implement control algorithms which change the state of a flexible robot arm from an initial state to a final resting state, it is necessary to compute the initial and final equilibrium positions. This section develops the equations necessary to obtain equilibrium positions. The equations of motion previously developed can be succinctly written:

$$\mathbf{f}(\ddot{\theta}, \ddot{\mathbf{d}}, \dot{\theta}, \dot{\mathbf{d}}, \theta, \mathbf{d}) = \mathbf{g}(M) \quad (3.82)$$

By definition, at static equilibrium, all velocities and accelerations are zero. Thus, equation 3.82 reduces to:

$$\mathbf{f}(\theta, \mathbf{d}) = \mathbf{g}(M) \quad (3.83)$$

This is a system of $n + 1$ equations with $n + 2$ unknowns, where n is the number of modes used to model the flexibility. The unknowns are θ , \mathbf{d} , and M . An additional equation is needed for a solution. This additional equation is derived by selecting the end point position. For this work, we will define this position with an angle θ_l as shown in Figure 3.3.

By incorporating the vertical deflection into equation 3.4, the vector locating any point along the beam, \mathbf{r}_p , may be written as:

$$\mathbf{r}_p = [(x - h) \sin \theta + v \cos \theta] \vec{i} + [v \sin \theta - (x - h) \cos \theta] \vec{j} \quad (3.84)$$

Applying the assumed modes model results in the following substitutions:

$$v = \mathbf{d}^T \boldsymbol{\psi} \quad (3.85)$$

and

$$h = \frac{\mathbf{d}^T \boldsymbol{\Xi} \mathbf{d}}{2x} \quad (3.86)$$

Thus, equation 3.84 evaluated at the end point of the beam gives:

$$\mathbf{r}_l = \left[\left(l - \frac{\mathbf{d}^T \boldsymbol{\Xi}_l \mathbf{d}}{2l} \right) \sin \theta + \left(\mathbf{d}^T \boldsymbol{\psi}_l \right) \cos \theta \right] \vec{i} + \left[\left(\mathbf{d}^T \boldsymbol{\psi}_l \right) \sin \theta - \left(l - \frac{\mathbf{d}^T \boldsymbol{\Xi}_l \mathbf{d}}{2l} \right) \cos \theta \right] \vec{j} \quad (3.87)$$

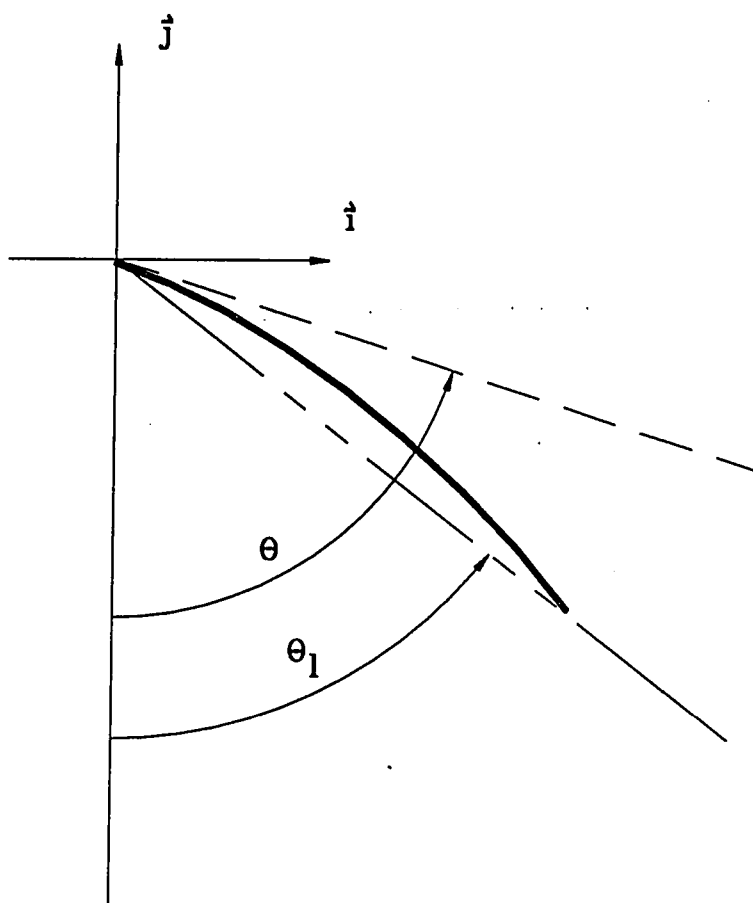


Figure 3.3: Schematic diagram showing the end point angle at static equilibrium

The angle of an imaginary line from the hub through the end point is related to the position of the end point by:

$$\tan \theta_l = \frac{\left[\left(l - \frac{d^T \Xi_l d}{2l} \right) \sin \theta + (d^T \psi_l) \cos \theta \right]}{- \left[(d^T \psi_l) \sin \theta - \left(l - \frac{d^T \Xi_l d}{2l} \right) \cos \theta \right]} \quad (3.88)$$

The static equilibrium solution may be obtained by solving equations 3.83 and 3.88. This is a system of $n + 2$ equations and $n + 2$ unknowns. The required hub torque M may be solved for by specifying the desired end point angle, θ_l , and the static equilibrium states θ , d .

3.10 Calculation of Strain

In an experimental setting, the direct measurement of the mode shape magnitudes is not possible. Therefore, this section develops an approximate relationship between mode shapes and strains. Strain measurement was selected because strain gages are relatively accurate, stable and easy to work with.

For a beam in bending, the following relationship holds [33]:

$$\frac{d^2 v}{dx^2} = \frac{d\theta}{dx} = \frac{1}{\rho} = \frac{M}{EI} \quad (3.89)$$

The strain at the surface of the robot arm is given by:

$$\varepsilon = \frac{u}{\rho} = u \left(\frac{d^2 v}{dx^2} \right) = uv'' \quad (3.90)$$

where u is the distance from the neutral axis of the robot arm to the surface. Applying the assumed modes model to the transverse motion of the robot arm gives:

$$v(x, t) = \sum d_i(t) \psi_i(x) = d^T \psi \quad (3.91)$$

$$v' = d\psi' \quad (3.92)$$

$$v'' = d\psi'' \quad (3.93)$$

which results in:

$$\varepsilon = u d^T \psi'' = u \psi''^T d \quad (3.94)$$

Thus, assuming that strain gages are placed at positions l_1, l_2, \dots, l_i on the robot arm, the following equations apply:

$$\varepsilon_1 = u \psi_{l_1}''^T d \quad (3.95)$$

$$\varepsilon_2 = u \psi_{l_2}''^T d \quad (3.96)$$

$$\vdots = \vdots$$

$$\varepsilon_i = u \psi_{l_i}''^T d \quad (3.97)$$

If the number of modes is set to be the same as the number of strain gages, the following matrix equation results:

$$\begin{bmatrix} \varepsilon_1 \\ \varepsilon_2 \\ \vdots \\ \varepsilon_i \end{bmatrix} = \begin{bmatrix} \psi_1''(l_1) & \psi_2''(l_1) & \cdots & \psi_i''(l_1) \\ \psi_1''(l_2) & \psi_2''(l_2) & \cdots & \psi_i''(l_2) \\ \vdots & \vdots & \ddots & \vdots \\ \psi_1''(l_i) & \psi_2''(l_i) & \cdots & \psi_i''(l_i) \end{bmatrix} \begin{bmatrix} \tilde{d}_1 \\ \tilde{d}_2 \\ \vdots \\ \tilde{d}_i \end{bmatrix} \quad (3.98)$$

This is a linear system that can be solved assuming all of the strain gages are placed at different locations along the beam. The matrix is time invariant. Thus, it needs to be decomposed or inverted only once.

4. CONTROL ALGORITHMS

This chapter develops schemes to control the end point of an elastic robot arm. The robot is assumed to move in a vertical plane from a known initial state to a specified target state. Both the initial and final states are taken as static equilibrium states.

The direct measurement of the end point position over the range of the robot arm is a very complex and expensive challenge. One possible solution is to use a real time vision system. These systems are very expensive and may have difficulty in dirty environments. In this thesis, the position of the end point is not used as a feedback quantity.

To facilitate the design of the control schemes, it is reasonable to linearize the nonlinear equations of motion given by equation 3.38 about the final static equilibrium state x_0 , as described in Chapter 3. The resulting linear second order system is then transformed into a linear first order system of the form

$$\dot{x}_l = Ax_l + bu_l \quad (4.1)$$

where A is a time invariant matrix and b is a time invariant row vector. The vector x_l is the linearized state vector:

$$x_l(t) = x(t) - x_0 \quad (4.2)$$

Thus, x_l is the difference of the state and the final static equilibrium state. It may be expanded to:

$$x_l = \begin{bmatrix} \theta - \theta_o \\ \dot{\theta} - \dot{\theta}_o \\ d_1 - d_{1o} \\ \dot{d}_1 - \dot{d}_{1o} \\ d_2 - d_{2o} \\ \dot{d}_2 - \dot{d}_{2o} \\ \vdots \\ d_n - d_{no} \\ \dot{d}_n - \dot{d}_{no} \end{bmatrix} \quad (4.3)$$

where d_i is the magnitude of the i th mode shape. The state vector is of dimension $2(n + 1)$ where n is the number of modes used to model the elastic motion of the arm. The initial conditions for the linearized system are:

$$x_l(0) = x(0) - x_o \quad (4.4)$$

The linearized control torque, u_l is the difference of the present control torque and the final static equilibrium control torque:

$$u_l(t) = u(t) - u_o \quad (4.5)$$

The output equation for the system is:

$$y_l = Cx_l \quad (4.6)$$

where C is a time invariant matrix that depends on the desired, or assumed, output. The vector y_l is the difference of the present output and final static equilibrium

output y_o :

$$y_l(t) = y(t) - y_o \quad (4.7)$$

At the desired target state \mathbf{x}_o , all of the linearized variables are zero.

Since the control problem will be implemented experimentally with a digital computer, it is necessary to develop the discretized versions of the system equations. As given by [34], for zero-order-hold sampling, the discretized versions of equations 4.1 and 4.7 will have the form:

$$\mathbf{x}(i+1) = \mathbf{A}_d \mathbf{x}(i) + \mathbf{b}_d u(i) \quad (4.8)$$

$$y(i) = \mathbf{C} \mathbf{x}(i) \quad (4.9)$$

where

$$\mathbf{A}_d = \exp(\mathbf{A}h) \quad (4.10)$$

$$\mathbf{b}_d = \int_0^h \exp(\mathbf{A}s) ds \mathbf{b} \quad (4.11)$$

where h is the sampling interval. In this work, h is taken to be 0.001 seconds. This corresponds to a discrete system operating at 1000 Hz. This choice of sampling interval will be more fully explained in Chapter 5.

It is also noted in [34] that the eigenvalues of the discretized system are related to the eigenvalues of the continuous system by:

$$\lambda_i(\mathbf{A}_d) = \exp(\lambda_i(\mathbf{A})h) \quad (4.12)$$

where $\lambda_i(\mathbf{A}_d)$ represents the i th eigenvalue of the discretized system and $\lambda_i(\mathbf{A})$ represents the i th eigenvalue of the continuous system.

Table 4.1: Physical parameters of the robot arm

cross sectional area	0.0469 in^2
area moment of inertia	$1.526 \times 10^{-5} \text{ in}^4$
length	40.875 in
neutral axis to outer fiber	0.03125 in
modulus of elasticity	$10.11 \times 10^6 \text{ lb / in}^2$
mass density	$2.419 \times 10^{-4} \text{ lb s}^2 / \text{in}^4$
base mass inertia	$4.51 \times 10^{-3} \text{ in lb s}^2$
gravity	386.2 in / s^2

Table 4.2: Physical parameters of the end masses

identifier	mass ($\text{lb s}^2 / \text{in}$)	inertia (in lb s^2)	% of arm mass
a	1.054×10^{-4}	1.165×10^{-5}	23
b	2.939×10^{-4}	2.832×10^{-5}	64

4.1 Model Parameters

Physical parameters must be entered into the model to run simulations and develop control algorithms. The parameters of the robot arm used in this study are given by Table 4.1. The end mass parameters are given by Table 4.2.

The fundamental natural frequency of the unloaded aluminum arm while vibrating about a hub angle of zero is 0.59 Hz. The arm has fundamental natural frequencies of 0.55 Hz and 0.53 Hz when loaded with 23% and 64% end masses, respectively.

The target states for the flexible arm are given in Table 4.3. These values were computed by solving the static equilibrium problem given by equations 3.83 and 3.88

Table 4.3: Flexible arm target static equilibrium states

θ_1	Quantity	Unloaded	23% end mass	64% end mass
45°	M	2.678	3.929	6.264
	θ	0.965	1.086	1.395
	d_1	-2.712	-5.926	-16.404
	d_2	-0.059	-0.100	-0.136
90°	M	3.653	5.307	8.463
	θ	1.821	1.997	2.428
	d_1	-3.762	-8.281	-22.362
	d_2	-0.070	-0.103	-0.091

for the cases of 45 and 90 degree end point positions. These values will be used as the desired target static equilibrium states in the simulation of the control algorithms.

All of the simulations will start from an initial hub angle of zero, with the arm straight down. The full nonlinear equations are used to model the arm, even though linear control laws are used.

4.2 Strain Gage Placement

The question still remains of where to place the strain gages on the robot arm. The magnitudes of the recreated mode shapes \tilde{d}_j , given by equation 3.98, are not exact. The determination of the optimal locations can be facilitated through a minimization problem. The performance index

$$J = \sum_{j=1}^i |d_j| (\tilde{d}_j - d_j)^2 \quad (4.13)$$

is minimized at various static equilibrium points with the robot arm described in Table 4.1 and the end mass payloads in Table 4.2. This function is used to minimize

the observation spillover. Figures 4.1 and 4.2 give the results of these calculations. The dimensionless position in the plots is the position of the gage, measured from the base of the arm, divided by the length of the arm. Thus, a dimensionless position of zero would imply the base of the arm, while a value of one would imply the tip of the arm. As can be seen, with the end masses and number of modes taken into account, there is not an overall optimal location for the strain gages. However, all of the optimums are located in the same general areas. In this research, the strain gages are placed at 0.122 and 0.480.

4.3 A Practical Consideration

An important limitation is placed on the control algorithms discussed in this chapter. The maximum magnitude of the control torque is set to 8.5 in-lbs, the value at which the aluminum arm was found to plastically deform. This limit will be imposed upon the control torque derived from the control algorithms.

4.4 Proportional-Derivative Controller

As a starting point, a proportional and derivative (PD) controller is designed to control the angle of the hub to the specified target state using only hub position and hub velocity feedback. This controller is designed assuming a rigid arm when computing the required feedback gains. The linearized system matrices for the rigid arm about the equilibrium point are input into MATRIXx [35]. A pole placement technique, with poles at $-4.442 \pm 4.442j$, is used to determine the necessary feedback gains for the continuous system. Feedback gains for the discretized system with analogous poles are also attained. It should be noted that the specified poles correspond

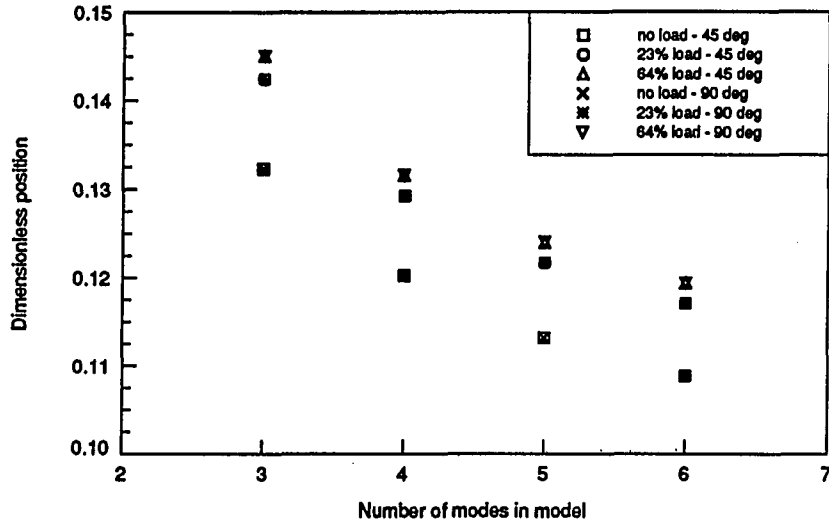


Figure 4.1: Optimal locations of the first strain gage

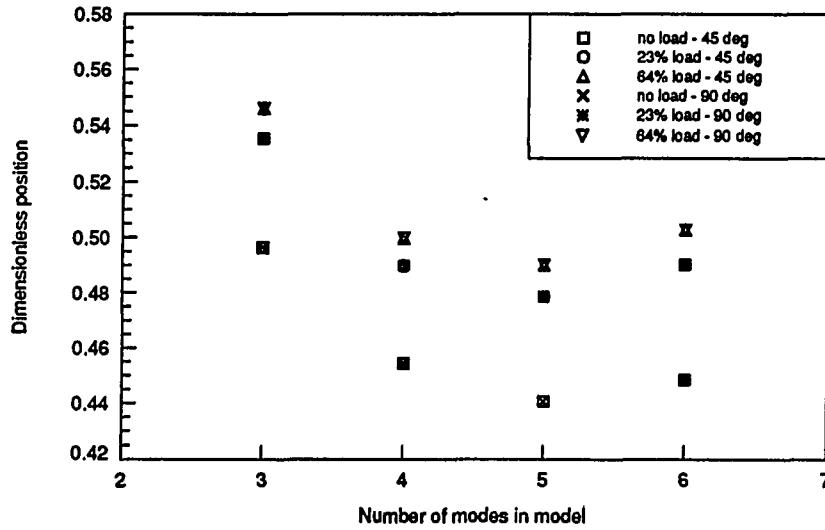


Figure 4.2: Optimal locations of the second strain gage

to a 1 Hz system with a damping ratio of 0.707. These values result in the fastest responses for the PD controller with the torque limitation.

The end point response obtained from commanding the rigid arm with and without the end masses to an angle of 45 degrees are given in Figure 4.3. The torque response is given in Figure 4.4. In this case, the hub angle and end point angle are identical. The angular position responses show an overshoot of approximately two degrees and rise times of about 0.5 seconds for the unloaded and 23% end mass cases. The 64% end mass cases shows a slightly longer rise time of 0.6 seconds. The settling times are approximately 1 second. The torque curves in Figure 4.4 clearly show the 8.5 in-lb torque limit. This limitation also results in the slightly slower responses of the mass loaded arms.

The PD controller using the same gains is then simulated using flexible arm dynamics. Three modes were used to model the flexibility. The target states are shifted to take into account the static droop of the arm, as specified in Table 4.3. The end point positions for the unloaded, 23% load, and 64% load are given in Figures 4.5, 4.7, and 4.9, respectively. The torque responses are given in Figures 4.6, 4.8, and 4.10 for each of the cases. Continuous and discrete flexible models, along with the reference rigid model responses, are given in each plot. In each case, the 1000 Hz discrete model is practically identical to the continuous model.

Figure 4.5 shows the unloaded end point response has a 14 degree overshoot, rise time of 0.4 seconds, and a settling time of approximately 2.5 seconds. Figure 4.6 shows the torque response for the flexible arm is not as smooth as the rigid arm. Neither case is restrained by the 8.5 in-lb limit. The steady state torques are not the

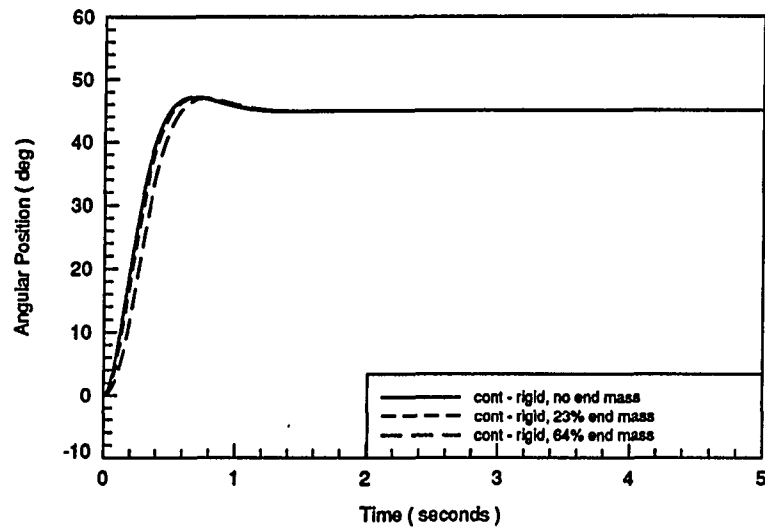


Figure 4.3: PD end point response of a rigid arm with a target end point position of 45 degrees

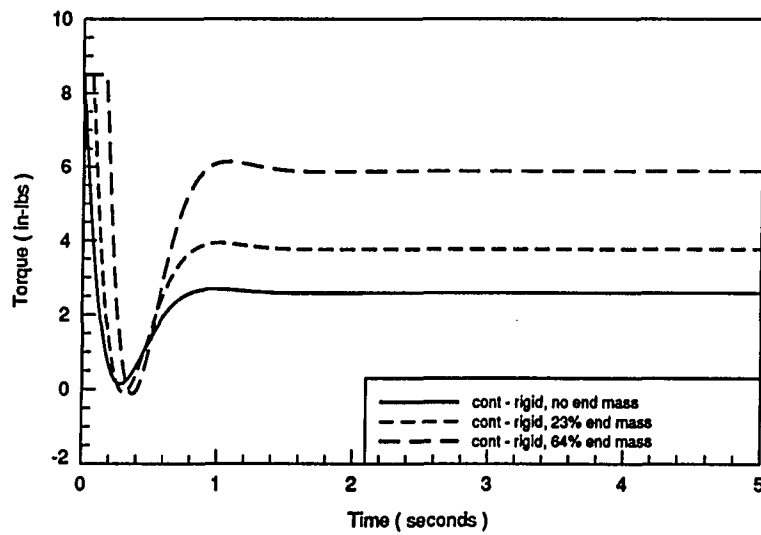


Figure 4.4: PD torque response of a rigid arm with a target end point position of 45 degrees

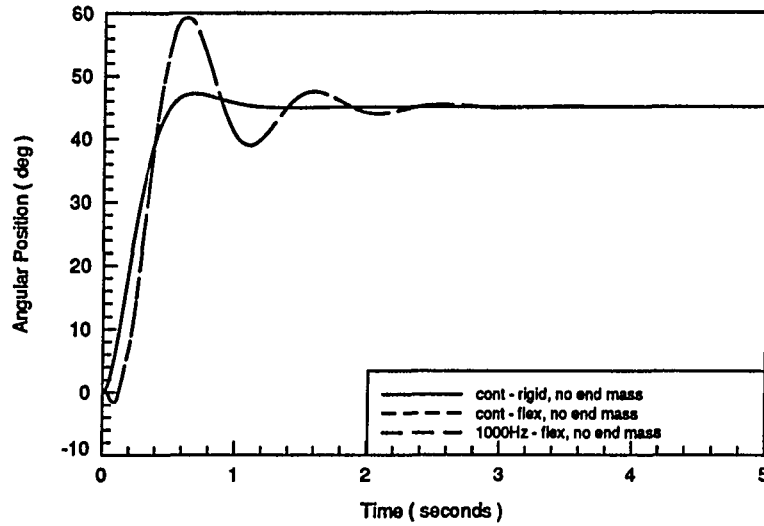


Figure 4.5: PD end point response of the unloaded flexible arm with a target end point position of 45 degrees

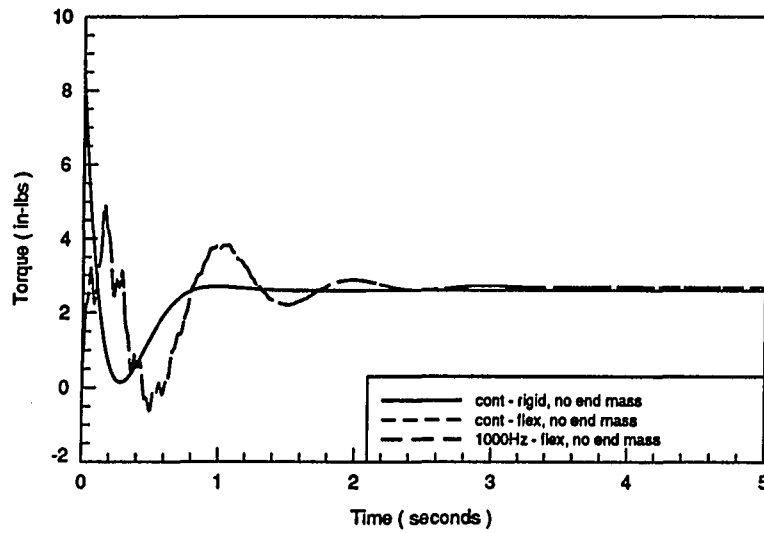


Figure 4.6: PD torque response of the unloaded flexible arm with a target end point position of 45 degrees

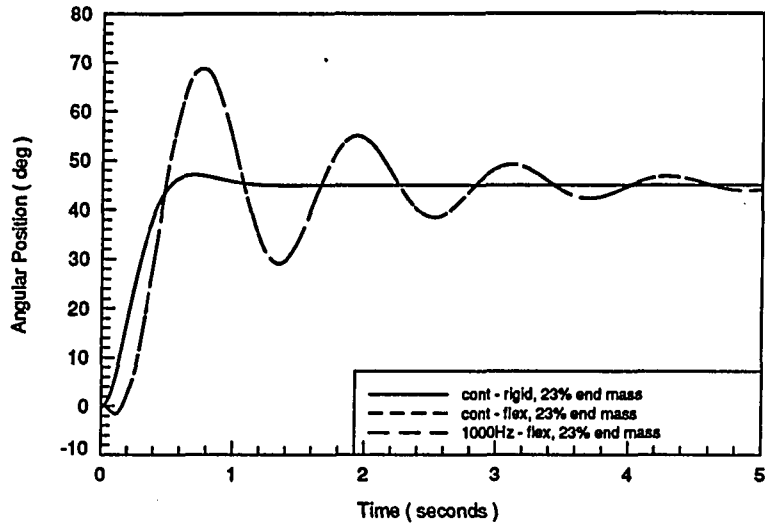


Figure 4.7: PD end point response of the flexible arm and 23% load with a target end point position of 45 degrees

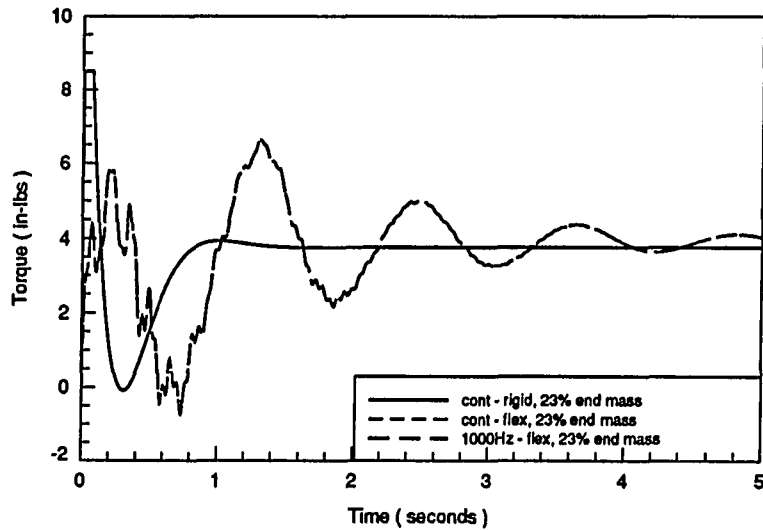


Figure 4.8: PD torque response of the flexible arm and 23% load with a target end point position of 45 degrees

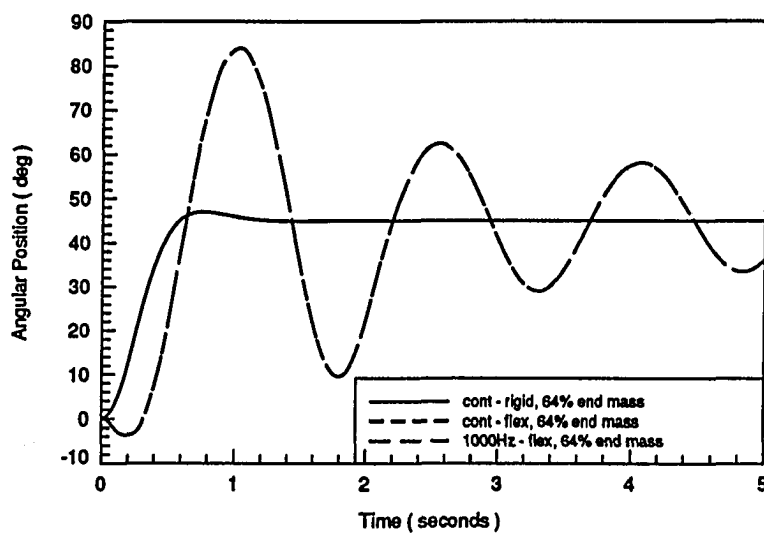


Figure 4.9: PD end point response of the flexible arm and 64% load with a target end point position of 45 degrees

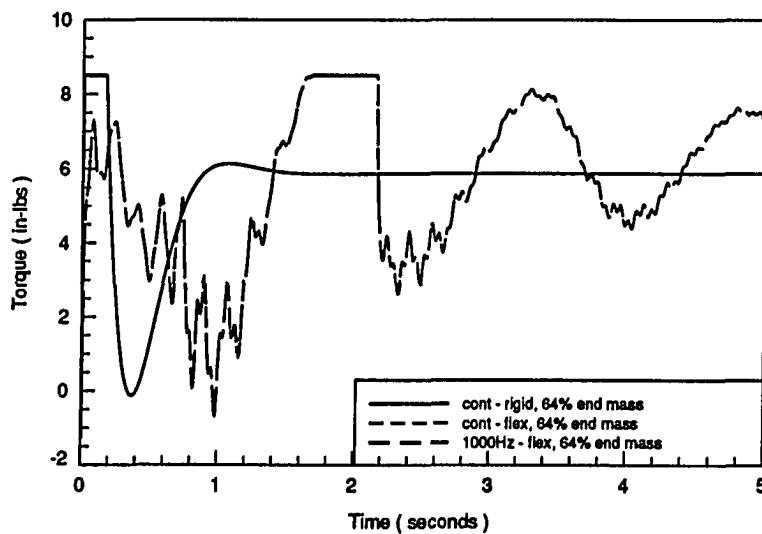


Figure 4.10: PD torque response of the flexible arm and 64% load with a target end point position of 45 degrees

same due to the different steady state targets necessary to maintain the target end point angle of 45 degrees.

Figure 4.7 shows the 23% loaded flexible arm end point response has a 25 degree overshoot, rise time of 0.5 seconds, and a settling time of more than 5 seconds. Figure 4.8 shows the torque response for the flexible arm is also not as smooth as the rigid case. The torque for the flexible case is limited only at the initial time. The rigid case was limited for about the first 0.1 seconds.

Figure 4.9 shows the 64% load end point response. The response indicates an overshoot of almost 42 degrees and significant residual vibrations. The torque response given in Figure 4.10 shows that the torque in the flexible case is limited for approximately 0.5 seconds while trying to control the overshoot.

A similar procedure is followed for the 90 degree target end point position. Figure 4.11 gives the end point responses for the rigid arm with various end masses. The unloaded and 23% end mass cases show overshoots of 6 degrees and settling times of 1.2 seconds. The rise times are 0.4 and 0.5 seconds, respectively. The 64% end mass case shows a much slower rise time of 0.7 seconds and a settling time of 2.8 seconds. The overshoot is 4 degrees. The slower times are explained by the torque responses given in Figure 4.12. The 64% end mass case is significantly restrained by the 8.5 in-lb limit.

Figures 4.13, 4.15, and 4.17 give the end point responses for the flexible arm with different end masses. Again, the 1000 Hz discrete responses are practically identical to the continuous responses. The corresponding torque responses are given by Figures 4.14, 4.16, and 4.18.

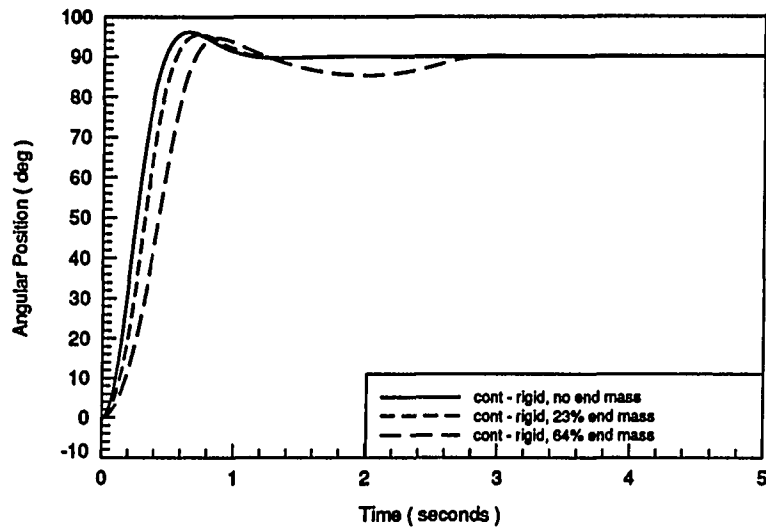


Figure 4.11: PD end point response of a rigid arm with a target end point position of 90 degrees

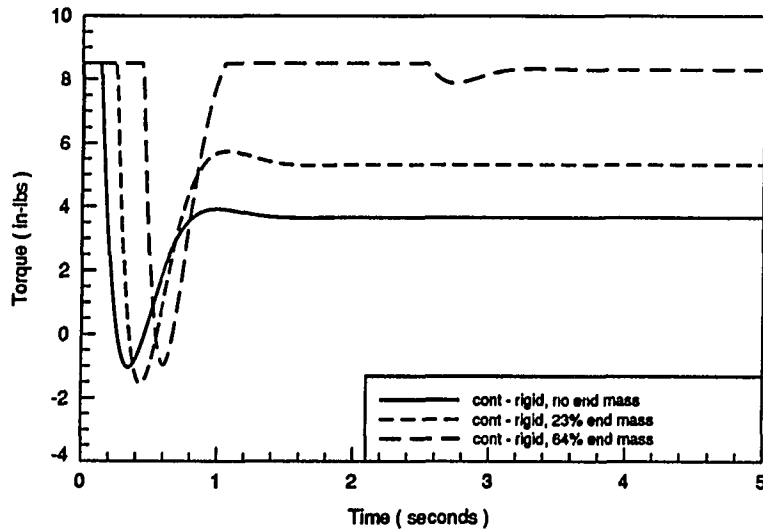


Figure 4.12: PD torque response of a rigid arm with a target end point position of 90 degrees

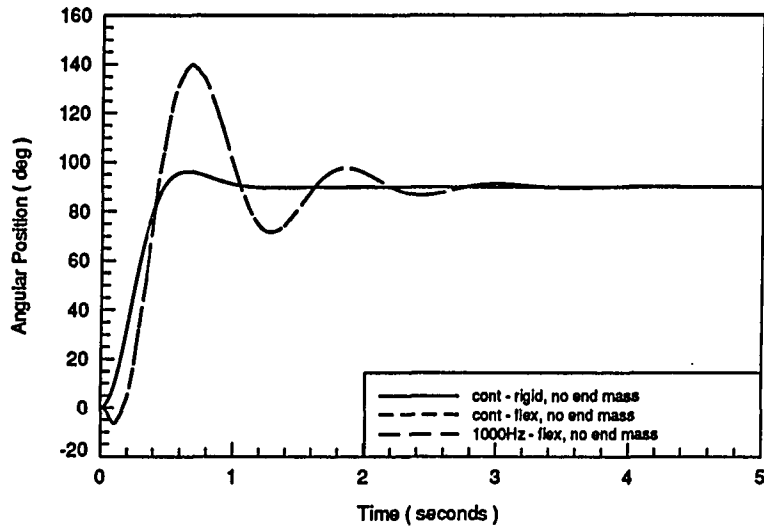


Figure 4.13: PD end point response of the unloaded flexible arm with a target end point position of 90 degrees

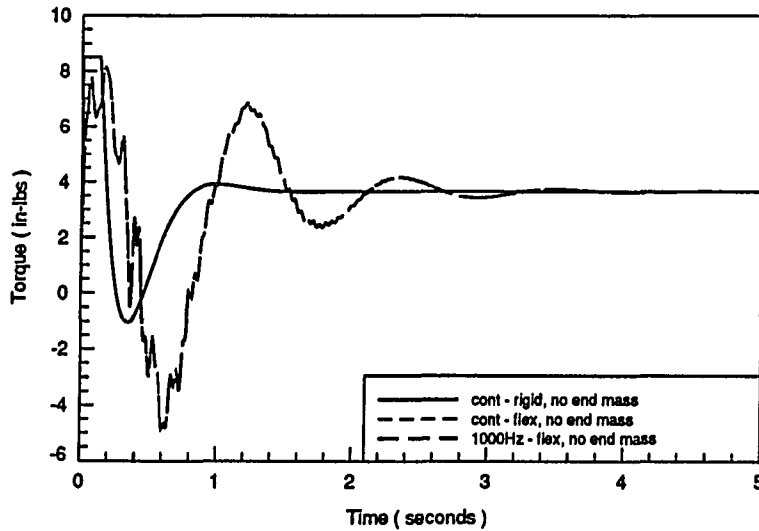


Figure 4.14: PD torque response of the unloaded flexible arm with a target end point position of 90 degrees

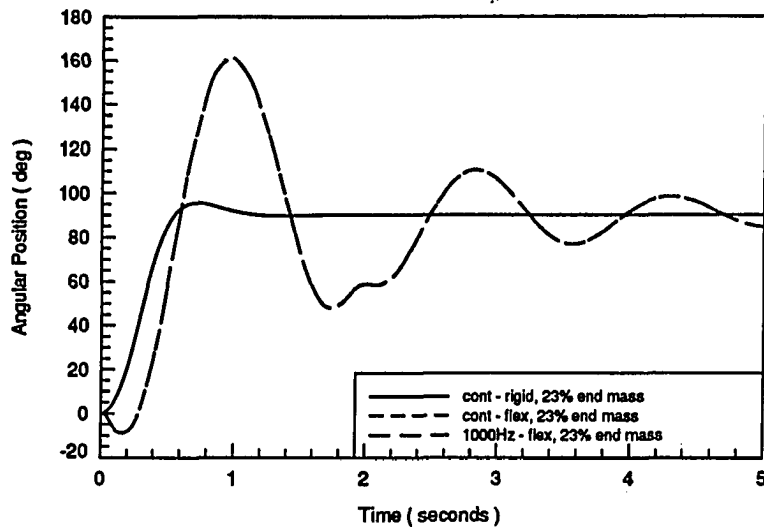


Figure 4.15: PD end point response of the flexible arm and 23% load with a target end point position of 90 degrees

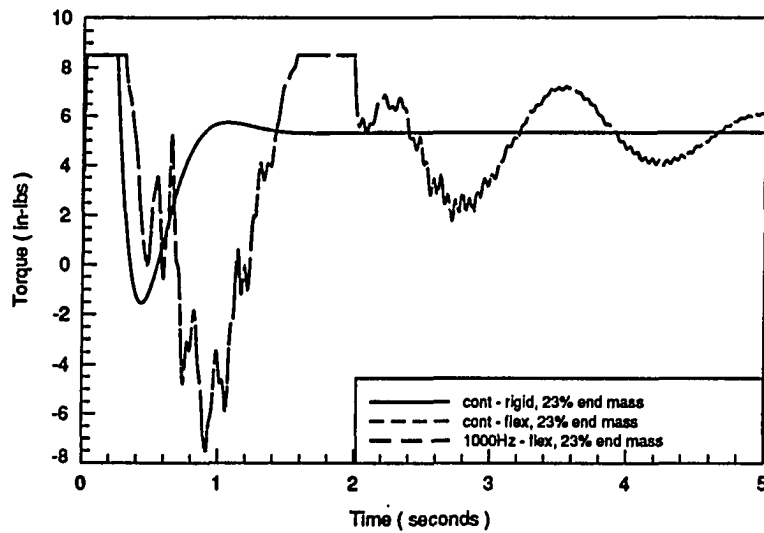


Figure 4.16: PD torque response of the flexible arm and 23% load with a target end point position of 90 degrees

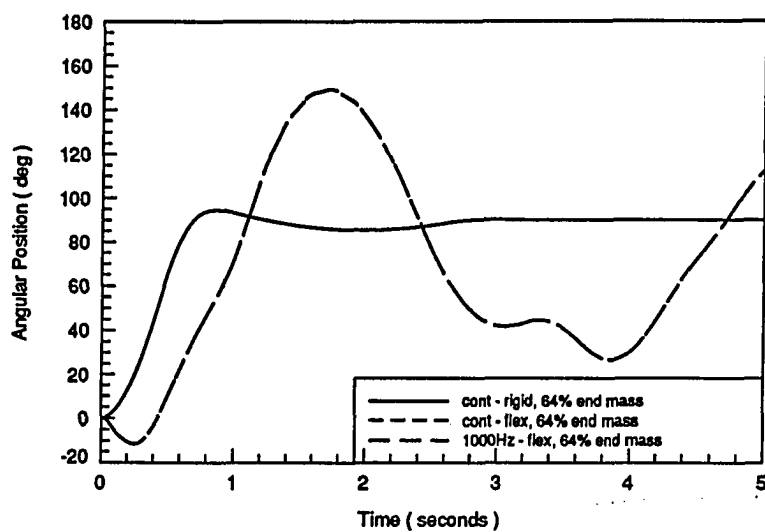


Figure 4.17: PD end point response of the flexible arm and 64% load with a target end point position of 90 degrees

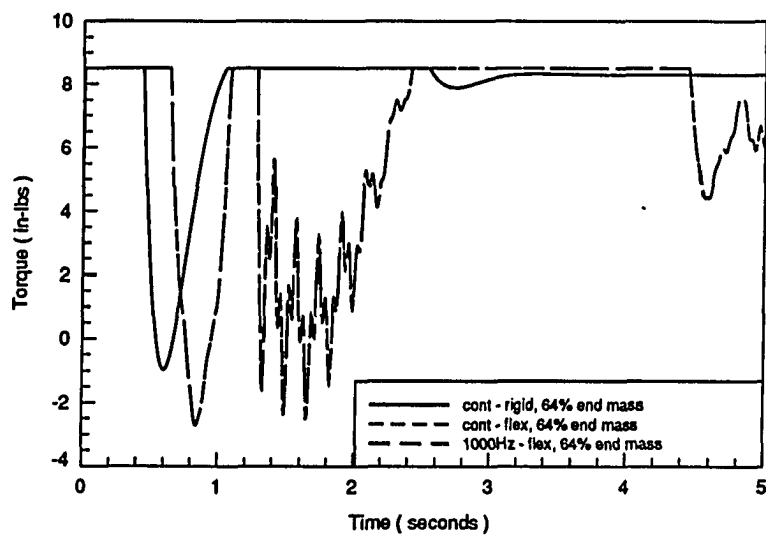


Figure 4.18: PD torque response of the flexible arm and 64% load with a target end point position of 90 degrees

Figure 4.13 shows the unloaded end point response. The response gives a rise time of 0.4 seconds and an overshoot of 50 degrees. The settling time is approximately 2.5 seconds. Figure 4.14 gives the torque response. The flexible arm torque is not restrained by the 8.5 in-lb limit.

Figure 4.15 shows the 23% mass loaded end point response. Figure 4.16 gives the corresponding torque response. The end point has a rise time of 0.6 seconds and a 70 degree overshoot. The torque response shows that the 8.5 in-lb limit is reached on two separate occasions.

Figure 4.17 shows the 64% mass loaded end point response. The end point has significant overshoot and the response has not settled after 5 seconds. Figure 4.18 shows that the torque response is severely limited by the 8.5 in-lb limit. This limit severely hampers the desired results of this controller.

4.5 Linear Quadratic Regulator

The previous section presented a feedback control algorithm that did not include flexibility effects of the arm. This is used as a basis to evaluate improvements from including flexibility in the control algorithm. This section develops an algorithm that does include feedback from the state variables describing the flexibility of the arm, as well as the hub angle and velocity.

A linear quadratic regulator [36] is developed using the linearized state equations, restated here for clarity:

$$\dot{x}_l = Ax_l + bu_l \quad (4.14)$$

$$y_l = Cx_l \quad (4.15)$$

with initial conditions of:

$$\mathbf{x}_l(0) = \mathbf{x}(0) - \mathbf{x}_o \quad (4.16)$$

It is assumed that the entire state is measurable. Since \mathbf{x}_l , u_l , and \mathbf{y}_l are equal to zero at the target state, a linear quadratic regulator may be developed by minimizing the following performance index:

$$J = \frac{1}{2} \int_0^\infty \left(\mathbf{x}_l^T \mathbf{Q} \mathbf{x}_l + u_l^T R u_l \right) dt \quad (4.17)$$

subject to equations 4.14, 4.15, and 4.16. The matrix \mathbf{Q} is symmetric, positive semi-definite and R is positive. The amounts of control effort and state variable responses are controlled by the choices of \mathbf{Q} and R .

The optimal time invariant feedback gain row vector is given by:

$$\mathbf{k} = \frac{\mathbf{b}^T \mathbf{P}}{R} \quad (4.18)$$

where \mathbf{P} is a positive definite matrix obtained by solving the following nonlinear algebraic matrix Riccati equation:

$$\mathbf{0} = \mathbf{A}^T \mathbf{P} + \mathbf{P} \mathbf{A} - \frac{\mathbf{P} \mathbf{b} \mathbf{b}^T \mathbf{P}}{R} + \mathbf{Q} \quad (4.19)$$

MATRIXx [35] was used to solve the linear quadratic optimal control problem. The optimal feedback control law is given by:

$$u_l = -\mathbf{k} \mathbf{x}_l \quad (4.20)$$

Note that this problem must be solved for each end point and end mass combination. It also must be solved for each choice of \mathbf{Q} and R .

The choices of \mathbf{Q} and R have profound effects upon the response of the system. As a starting point, the following values are used for \mathbf{Q} and R :

$$\text{diag}(\mathbf{Q}) = \left(\begin{array}{cccccccc} 0.5 & 0.1 & 0.01 & 0.001 & 0.001 & 0.0001 & 0.0001 & 0.00001 \end{array} \right) \quad (4.21)$$

$$R = 0.001 \quad (4.22)$$

The Riccati equation is solved using these weighting factors and the resulting feedback gains implemented in a simulation. This control algorithm will be referred to as LQRA. The full nonlinear equations of motion are used to model the robot arm. In this situation, the gain vector will be used to control a nonlinear system. Thus, the control obtained by the above procedure will not be an optimal control law. It is an optimal control law for the linearized system, not the nonlinear system.

Figures 4.19 and 4.20 give the end point and torque responses of the unloaded arm with a target end point angle of 45 degrees. The plots give the results of three different continuous time simulations. The full state feedback case using the actual magnitudes of the mode shapes is shown as the solid line. The velocities of the mode shapes are quantities that are very difficult to determine experimentally. Thus, the case of not feeding back the velocities of the mode shapes is given in the figures. The third simulation result given in Figures 4.19 and 4.20 is the case of feeding back the recreated mode shapes obtained from the strains as given by equation 3.98. In this case, two strain gages are assumed. Thus, only the first two recreated mode shapes are available for feedback. Figure 4.19 shows all three cases give approximately the same results. The rise time is slightly longer than 1 second. The full state feedback shows a settling time of 2 seconds. The other cases do not exhibit the pause and settle in about 1.5 seconds. The torque responses of all three are very similar.

The same weighting factors are then applied to the model with 23% end mass. The Riccati equation is solved and new feedback gains obtained for each of the cases. Figures 4.21 and 4.22 give the end point and torque responses for this case. The full state feedback case shows a rise time of 0.9 seconds, an overshoot of 4 degrees, and a

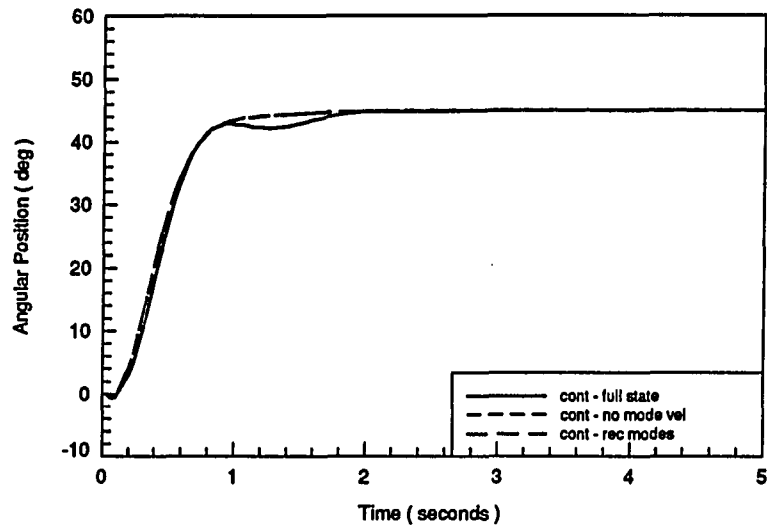


Figure 4.19: LQRA end point response of the unloaded flexible arm with a target end point position of 45 degrees

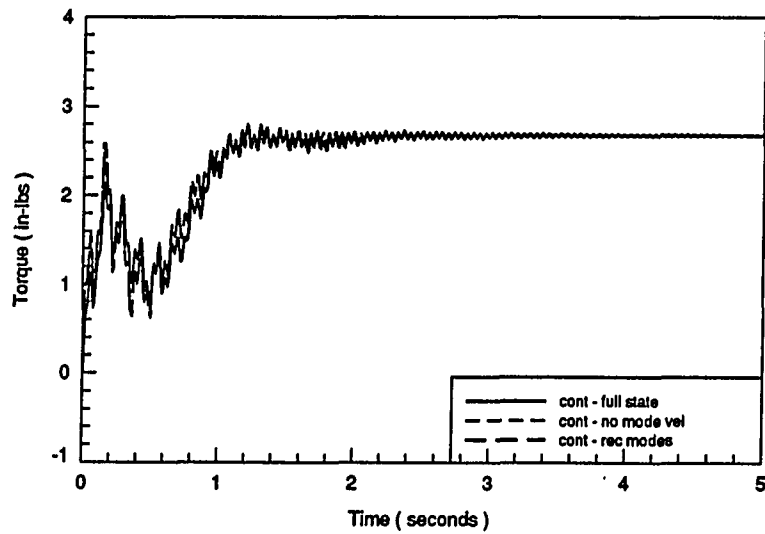


Figure 4.20: LQRA torque response of the unloaded flexible arm with a target end point position of 45 degrees

settling time of approximately 2.5 seconds. Figure 4.22 shows the torque responses. The modal velocity feedback terms in the full state algorithm reduces spikes seen in the other two responses.

Figures 4.23 and 4.24 give the end point and torque responses for the 64% end mass case. The full state feedback end point response shows a rise time of 0.85 seconds with an overshoot of 13 degrees. The other cases exhibit a rise time of 0.75 seconds with an overshoot of 17 degrees. None of the responses settle before the end of the five second simulation. The torque response shows that the modal velocity feedback terms again limit the spikes in the torque response. However, the 8.5 in-lb limit is not reached.

The figures show quite different responses using the same weighting factors for the different end masses. To get a better end point response for the 64% end mass case, new weighting factors are implemented. The matrix Q is set to:

$$\text{diag}(Q) = \begin{pmatrix} 0.5 & 0.75 & 0.01 & 0.001 & 0.001 & 0.0001 & 0.0001 & 0.00001 \end{pmatrix} \quad (4.23)$$

and R is left unchanged:

$$R = 0.001 \quad (4.24)$$

The Riccati equation is solved using the new weighting factors and the resulting feedback gains implemented for each end mass. This algorithm will be referred to as LQRB.

Figures 4.25 and 4.26 give the responses for the 64% mass loaded arm with a target end point position of 45 degrees. Figure 4.25 shows the full state feedback case reaches the target end point position at about 1.2 seconds, but then falls back 5 degrees before returning to the target value. The settling time is about 3 seconds.

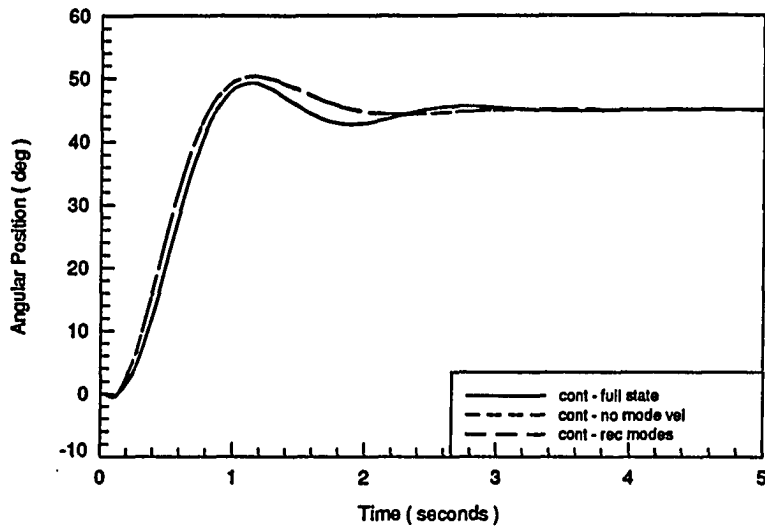


Figure 4.21: LQRA end point response of the flexible arm and 23% end mass with a target end point position of 45 degrees

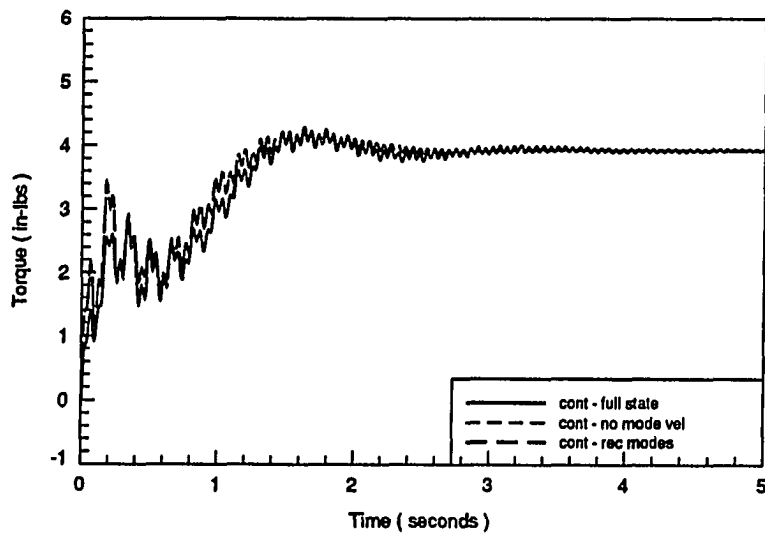


Figure 4.22: LQRA torque response of the flexible arm and 23% end mass with a target end point position of 45 degrees

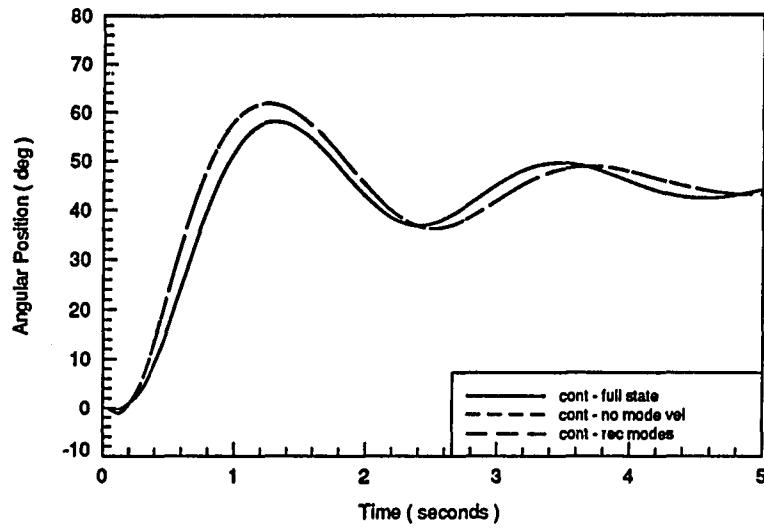


Figure 4.23: LQRA end point response of the flexible arm and 64% end mass with a target end point position of 45 degrees

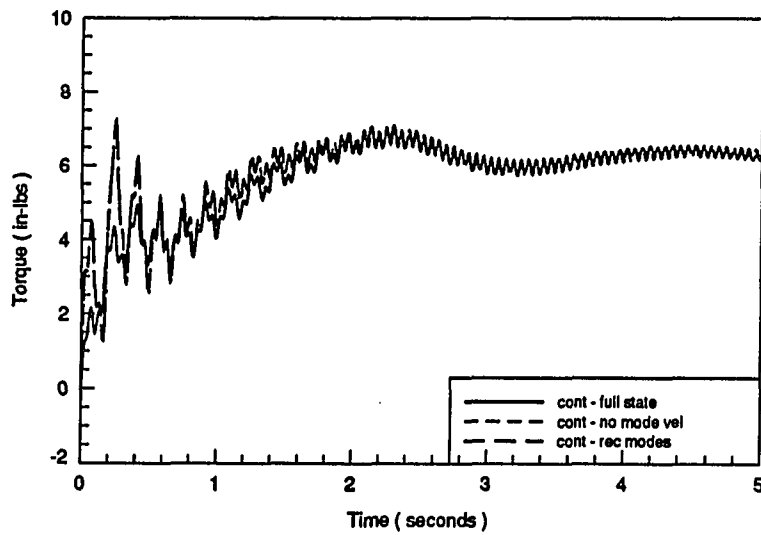


Figure 4.24: LQRA torque response of the flexible arm and 64% end mass with a target end point position of 45 degrees

The cases of no modal velocity feedback shows a very slight overshoot with a settling time of 2.6 seconds. Figure 4.26 shows that the torque responses are not limited by the 8.5 in-lb cap.

The drawback to using the feedback gains obtained using these weighting factors is the very slow endpoint response times for the unloaded and 23% mass loaded arms. Figures 4.27 and 4.28 give the end point responses for the unloaded and 23% mass loaded cases, respectively. Both figures show responses with no overshoot or oscillation. However, the response time is about 4 seconds.

For best performance, the weighting factors should be modified for each end mass. The effects of changing the target state while using the previous weighting factors is now investigated. The weighting factors given by equations 4.21 and 4.22 are used. The target end point position is 90 degrees. New feedback gains are obtained by solving the Riccati equation with the new state equations. This control algorithm will be referred to as LQRA.

Figures 4.29 and 4.30 give the responses of the end point of the arm and the torque applied to the hub. Figure 4.29 shows the response of the full state feedback has a rise time of 0.8 seconds, an overshoot of 1 degree followed by a slight oscillation. The settling time is about 2 seconds. The other two responses have a rise time of 1 second and do not oscillate. Figure 4.30 shows the torque responses are not limited by the 8.5 in-lb cap.

Figures 4.31 and 4.32 give the responses for the arm with 23% end mass. Figure 4.31 shows the end point responses have rise times of 0.8 seconds. The full state response has an overshoot of 10 degrees with a settling time of 2 seconds. The other two responses show an overshoot of 8 degrees but a longer settling time of 2.5 seconds.

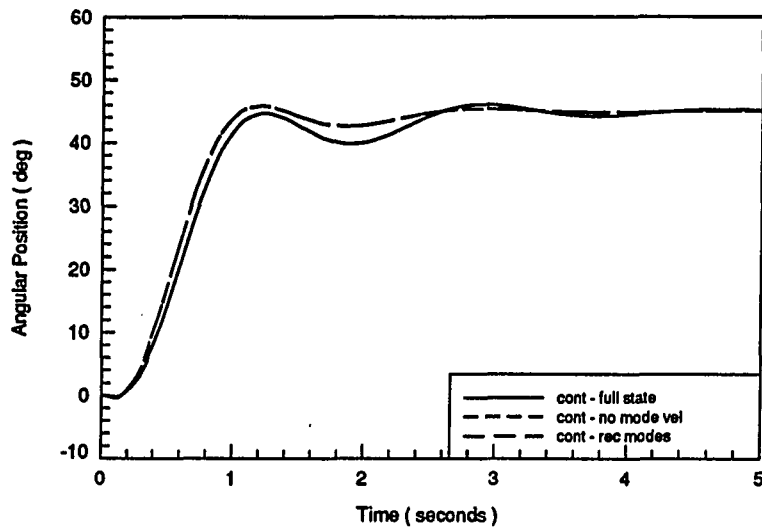


Figure 4.25: LQRB end point response of the flexible arm and 64% end mass with a target end point position of 45 degrees

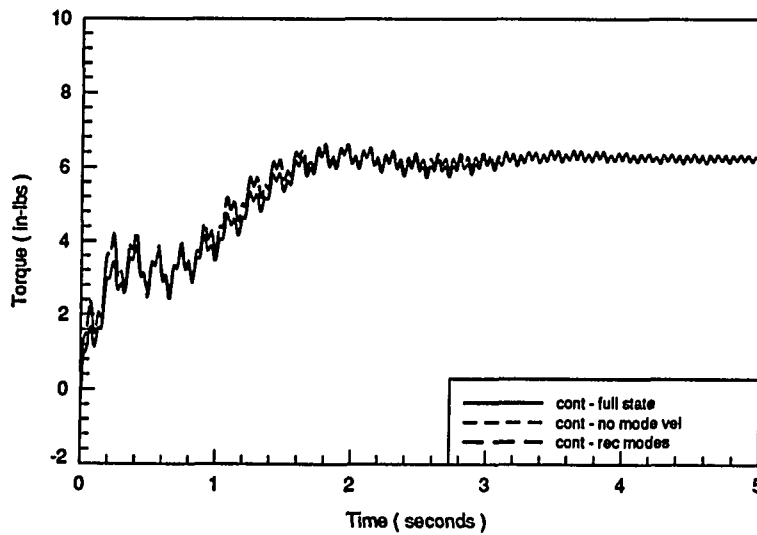


Figure 4.26: LQRB torque response of the flexible arm and 64% end mass with a target end point position of 45 degrees

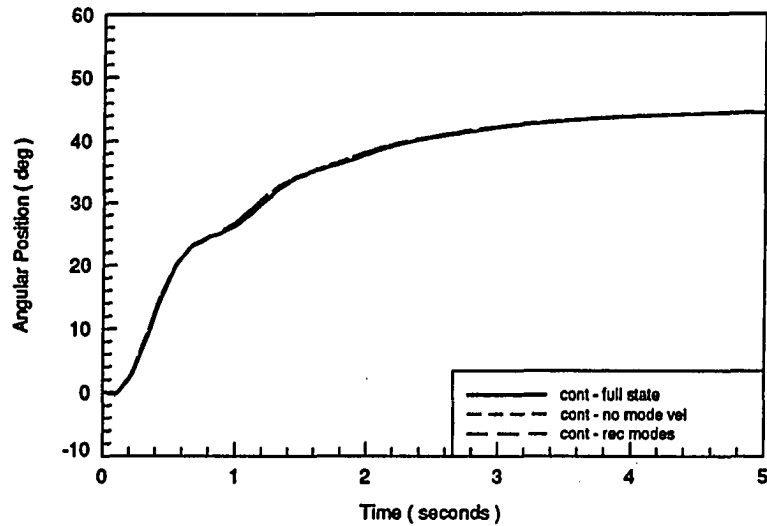


Figure 4.27: LQRB end point response of the unloaded flexible arm with a target end point position of 45 degrees

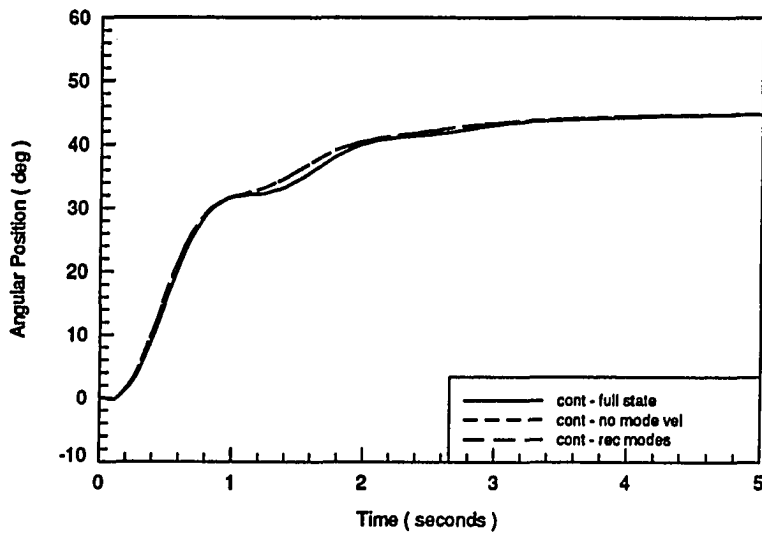


Figure 4.28: LQRB end point response of the flexible arm and 23% end mass with a target end point position of 45 degrees

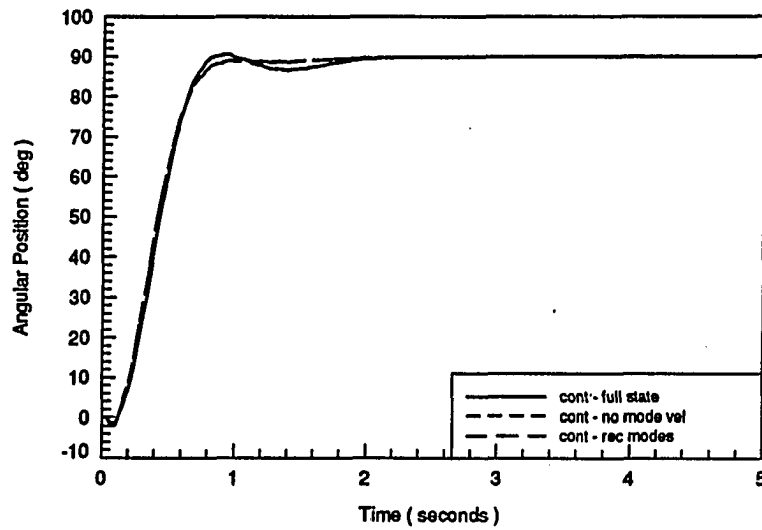


Figure 4.29: LQRA end point response of the unloaded flexible arm with a target end point position of 90 degrees

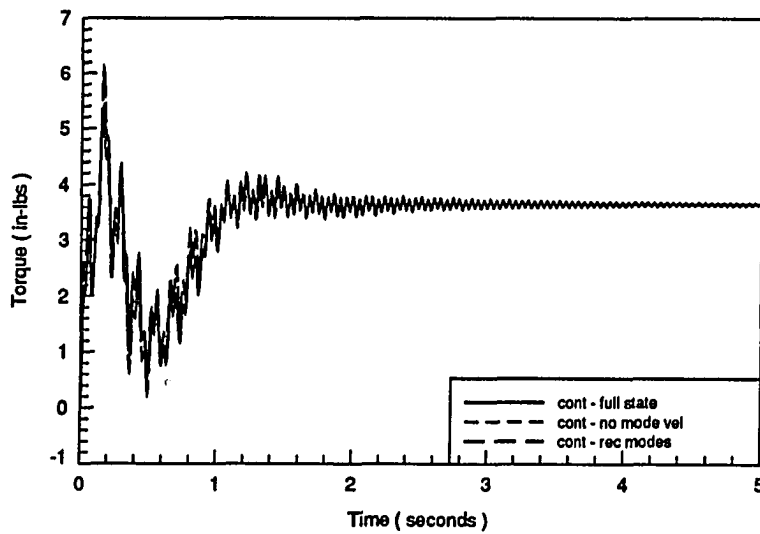


Figure 4.30: LQRA torque response of the unloaded flexible arm with a target end point position of 90 degrees

Figure 4.32 shows the torque responses are not limited by the 8.5 in-lb restriction.

Figures 4.33 and 4.34 give the responses for the flexible arm with 64% end mass. Figure 4.33 shows the responses of the end point. The rise time for all the cases is approximately 0.9 seconds. The full state algorithm shows a response with an overshoot of 24 degrees and that is slowly settling out. The other two cases show a slightly larger overshoot of 26 degrees and a slow decay down to the target state. Figure 4.34 shows the torque responses are limited by the 8.5 in-lb cap.

The weighting factors given in equations 4.23 and 4.24 are now implemented with a target end point position of 90 degrees. Figures 4.35 and 4.36 give the responses of the end points for the unloaded and 23% mass loaded arms, respectively. The responses are slow with response times of approximately 4 seconds, but no overshoot or oscillation.

Figures 4.37 and 4.38 give the end point and torque responses for the 64% end mass and arm. The full state feedback case shows a response time of 0.9 seconds and an overshoot of 17 degrees. The other cases have a response time of 0.95 seconds and a 15 degree overshoot. The responses do not settle within 5 seconds. Figure 4.38 shows the torque responses are limited by the 8.5 in-lb limit.

4.6 Linear Quadratic Regulator with Prescribed Degree of Stability

The previous section developed the linear quadratic regulator problem. This section extends the problem to include a prescribed degree of stability of α , where α is a non-negative number.

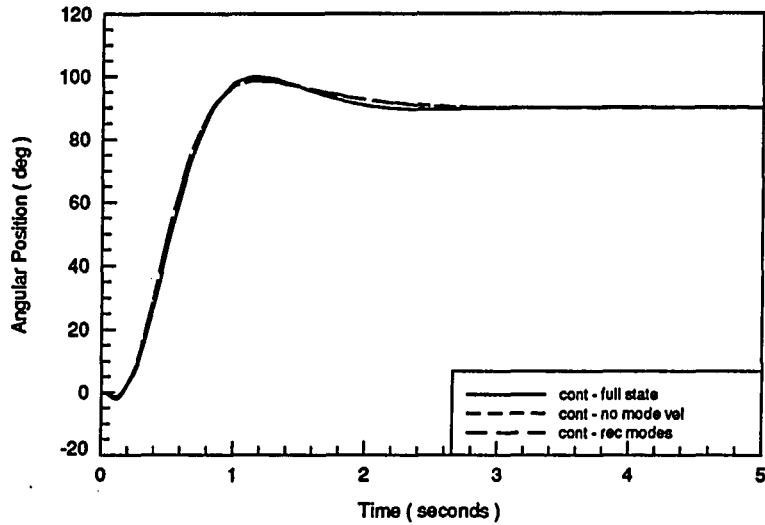


Figure 4.31: LQRA end point response of the flexible arm and 23% end mass with a target end point position of 90 degrees

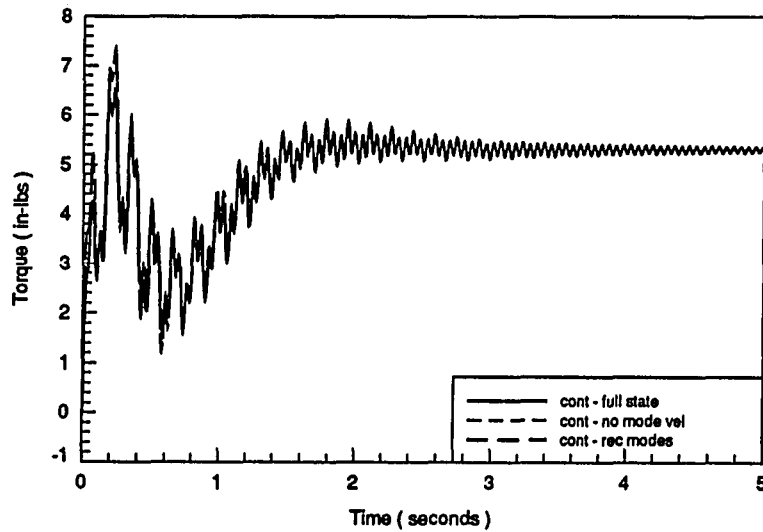


Figure 4.32: LQRA torque response of the flexible arm and 23% end mass with a target end point position of 90 degrees

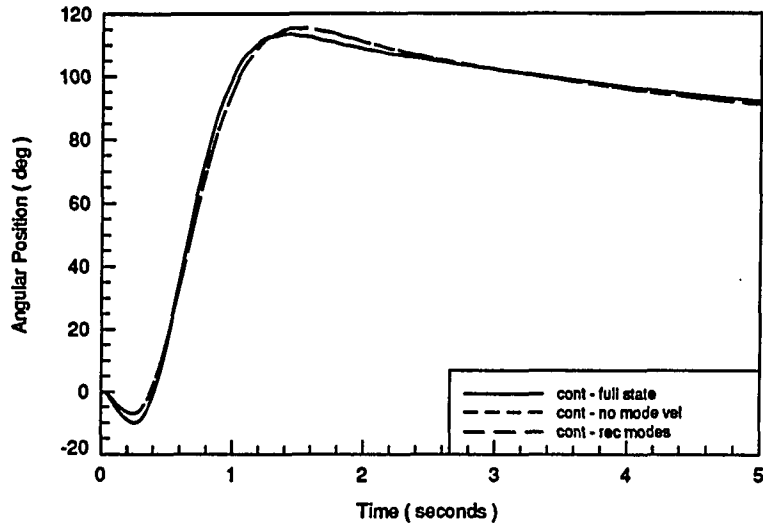


Figure 4.33: LQRA end point response of the flexible arm and 64% end mass with a target end point position of 90 degrees

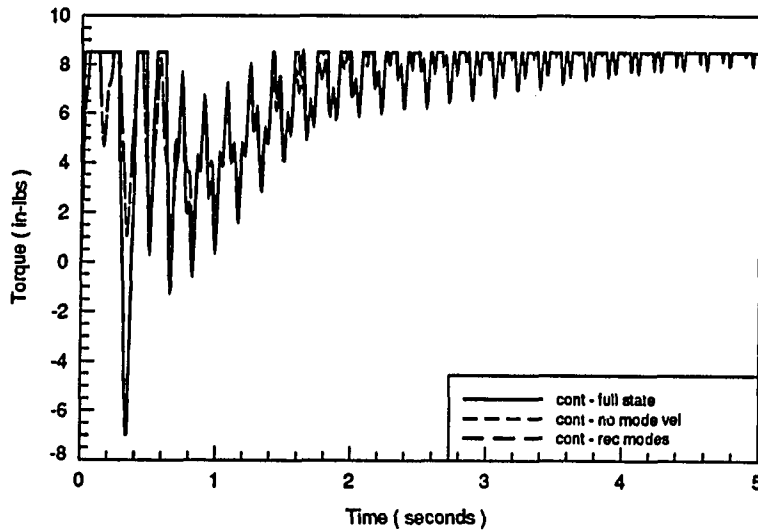


Figure 4.34: LQRA torque response of the flexible arm and 64% end mass with a target end point position of 90 degrees

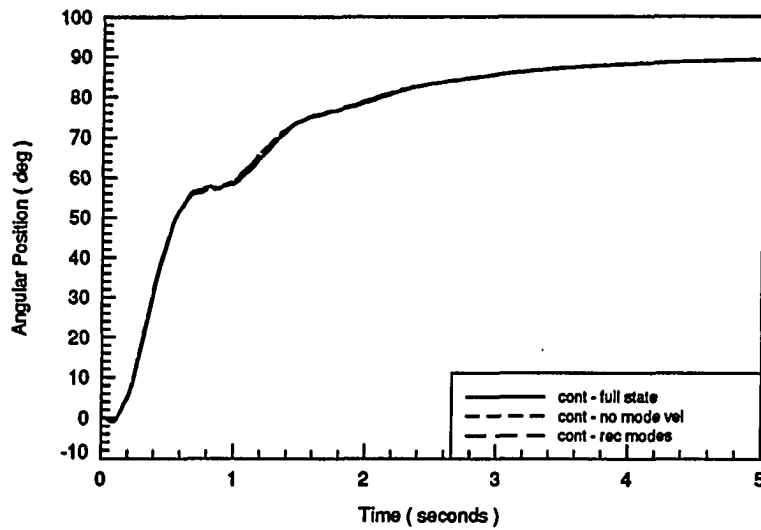


Figure 4.35: LQRB end point response of the unloaded flexible arm with a target end point position of 90 degrees

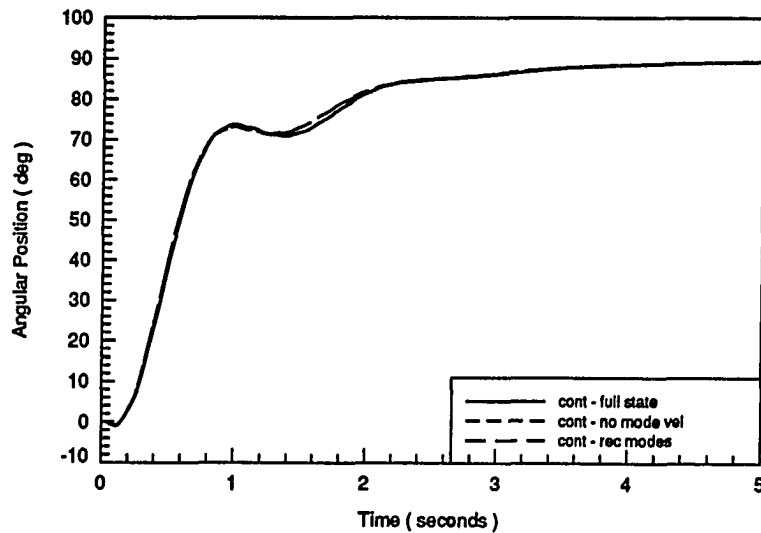


Figure 4.36: LQRB end point response of the flexible arm and 23% end mass with a target end point position of 90 degrees

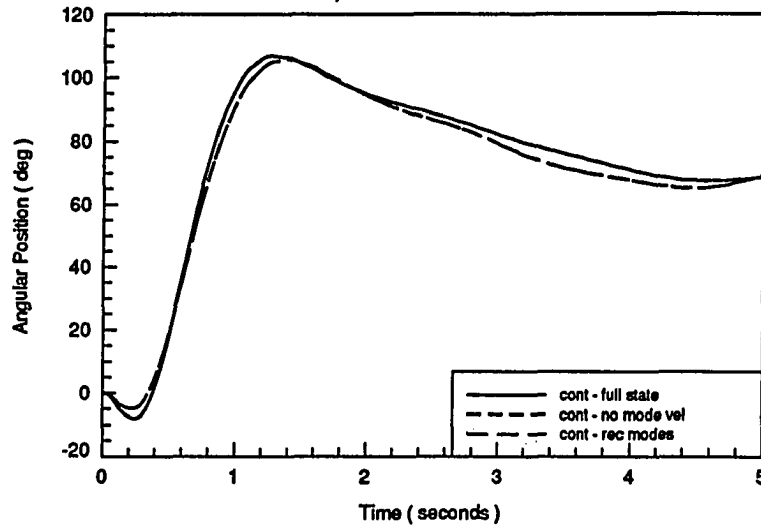


Figure 4.37: LQRB end point response of the flexible arm and 64% end mass with a target end point position of 90 degrees

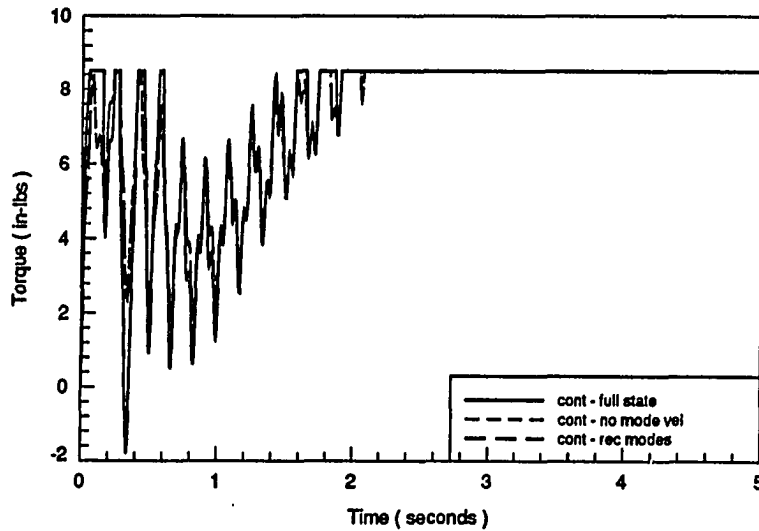


Figure 4.38: LQRB torque response of the flexible arm and 64% end mass with a target end point position of 90 degrees

The optimal control problem is restated here for clarity:

$$\min J = \frac{1}{2} \int_0^{\infty} \left(\mathbf{x}_l^T \mathbf{Q} \mathbf{x}_l + u_l^T R u_l \right) dt \quad (4.25)$$

subject to:

$$\dot{\mathbf{x}}_l = \mathbf{A} \mathbf{x}_l + \mathbf{b} u_l \quad (4.26)$$

$$\mathbf{y}_l = \mathbf{C} \mathbf{x}_l \quad (4.27)$$

$$\mathbf{x}_l(0) = \mathbf{x}(0) - \mathbf{x}_o \quad (4.28)$$

To induce a prescribed degree of stability [37] into the above problem, the performance index is modified to:

$$\bar{J} = \frac{1}{2} \int_0^{\infty} \left(\mathbf{x}_l^T \mathbf{Q} \mathbf{x}_l + u_l^T R u_l \right) e^{2\alpha t} dt \quad (4.29)$$

with new states, control, and outputs defined as:

$$\bar{\mathbf{x}} = \mathbf{x}_l e^{\alpha t} \quad (4.30)$$

$$\bar{u} = u_l e^{\alpha t} \quad (4.31)$$

$$\bar{\mathbf{y}} = \mathbf{y}_l e^{\alpha t} \quad (4.32)$$

The performance index given by equation 4.29 can be rewritten as:

$$\bar{J} = \frac{1}{2} \int_0^{\infty} \left(\bar{\mathbf{x}}^T \mathbf{Q} \bar{\mathbf{x}} + \bar{u}^T R \bar{u} \right) dt \quad (4.33)$$

Differentiating the newly defined state, $\bar{\mathbf{x}}$, with respect to time gives:

$$\dot{\bar{\mathbf{x}}} = \dot{\mathbf{x}}_l e^{\alpha t} + \alpha \mathbf{x}_l e^{\alpha t} \quad (4.34)$$

Multiplying the linearized state equation by $e^{\alpha t}$ gives

$$\dot{\mathbf{x}}_l e^{\alpha t} = \mathbf{A} \mathbf{x}_l e^{\alpha t} + \mathbf{b} u_l e^{\alpha t} \quad (4.35)$$

Making the appropriate substitutions into equation 4.35 gives the new linear dynamic system equation:

$$\dot{\tilde{\mathbf{x}}} = (\mathbf{A} + \alpha\mathbf{I})\tilde{\mathbf{x}} + \mathbf{b}\tilde{u} \quad (4.36)$$

Which can be written as:

$$\dot{\tilde{\mathbf{x}}} = \tilde{\mathbf{A}}\tilde{\mathbf{x}} + \mathbf{b}\tilde{u} \quad (4.37)$$

The initial conditions have remained unchanged since $e^{\alpha 0} = 1$:

$$\tilde{\mathbf{x}}(0) = \mathbf{x}_l(0) = \mathbf{x}(0) - \mathbf{x}_o \quad (4.38)$$

The new output equation is found to be:

$$\tilde{y} = \mathbf{C}\tilde{\mathbf{x}} \quad (4.39)$$

This optimal control problem is solved by finding the solution to the following matrix Riccati equation:

$$\mathbf{0} = \tilde{\mathbf{A}}^T\tilde{\mathbf{P}} + \tilde{\mathbf{P}}\tilde{\mathbf{A}} - \frac{\tilde{\mathbf{P}}\mathbf{b}\mathbf{b}^T\tilde{\mathbf{P}}}{R} + \mathbf{Q} \quad (4.40)$$

where the only change from the previous Riccati equation has been the substitution of $\tilde{\mathbf{A}}$ for \mathbf{A} . MATRIXx is again used to solve the above equation for $\tilde{\mathbf{P}}$. The new optimal feedback law is given by:

$$\tilde{u} = -\frac{\mathbf{b}^T\tilde{\mathbf{P}}}{R}\tilde{\mathbf{x}} = -\tilde{\mathbf{k}}\tilde{\mathbf{x}} \quad (4.41)$$

Factoring $e^{\alpha t}$ from equation 4.41 results in:

$$u_l = -\frac{\mathbf{b}^T\tilde{\mathbf{P}}}{R}\mathbf{x}_l = -\tilde{\mathbf{k}}\mathbf{x}_l \quad (4.42)$$

From an intuitive stand point, this method artificially induces negative damping and spring rates into the dynamic equations. The resulting control law must

counteract this artificial instability. Thus, when the control law is implemented on the original system, the poles are moved further from the origin and the damping is increased.

The stability parameter, α , is assigned a value of 2. The weighting factors given by equations 4.21 and 4.22 are used. The modified Riccati equation is solved and the resulting feedback gains used in simulations using the full nonlinear equations to model the robot arm. This choice of α and weighting factors will be referred to as LQRA2. A target end point position of 45 degrees is used.

Figures 4.39 and 4.40 give the responses of the end points and the torques for the unloaded arm. Figure 4.39 shows the full state feedback case has a rise time of 0.7 seconds with no overshoot. The other cases show a rise time of 0.6 seconds, 1 degree overshoot, and a settling time of 1.4 seconds. Figure 4.40 shows the torque response for the full state feedback case is smooth. In this case, the recreated mode shape case shows a torque response that is not identical to the case of feeding back all of the actual mode shapes. The response from the recreated mode shape case shows oscillations due to the third mode of vibration.

Figures 4.41 and 4.42 show the responses of the flexible arm and 23% end mass. Figure 4.41 gives the responses of the end points. The full state feedback case shows a rise time of 0.9 seconds and no overshoot. The other responses show a rise time of 0.8 seconds, 1 degree overshoot, and a settling time of 2 seconds. Figure 4.42 gives the torque responses. Again, the full state model gives the smoothest response. The response from the recreated mode shapes show oscillations that may be attributed to the third mode spilling over into the observed first and second modes. The responses are not limited by the torque cap.

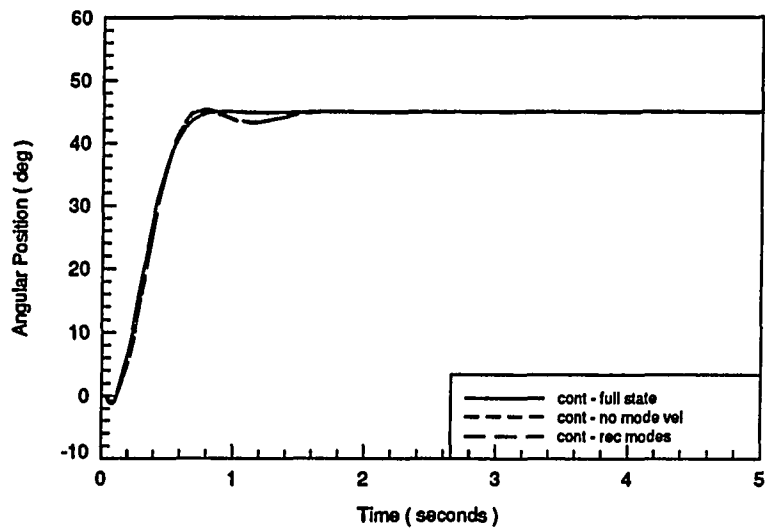


Figure 4.39: LQRA2 end point response of the unloaded flexible arm with a target end point position of 45 degrees

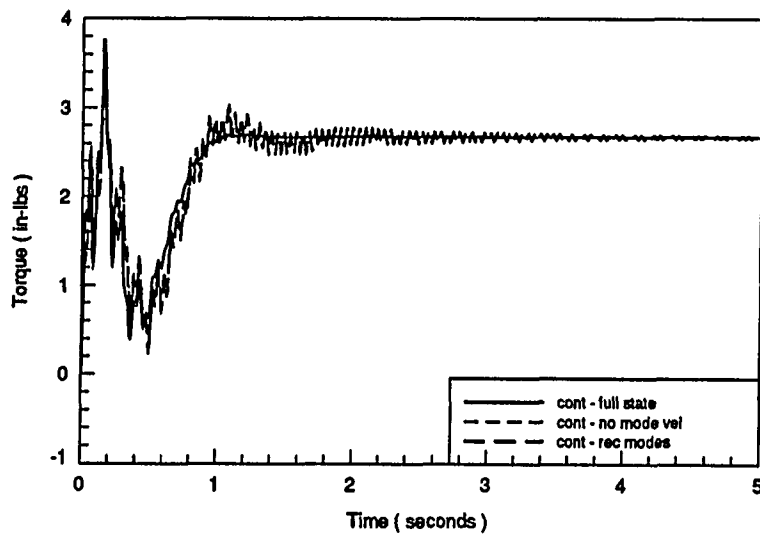


Figure 4.40: LQRA2 torque response of the unloaded flexible arm with a target end point position of 45 degrees

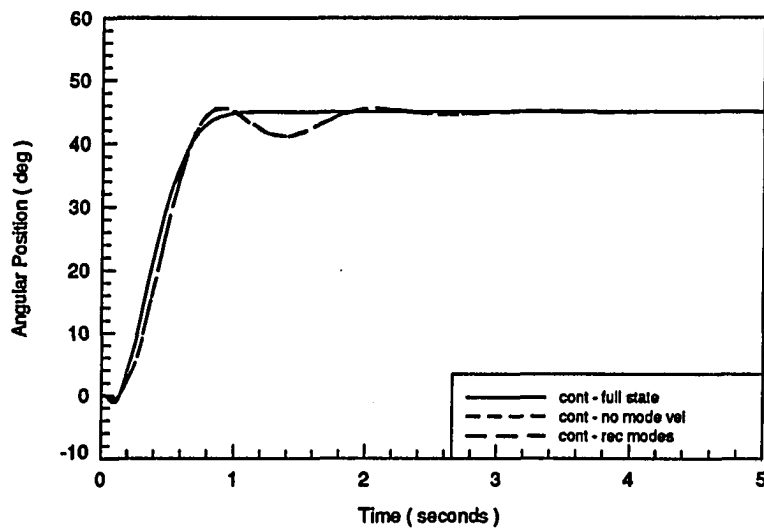


Figure 4.41: LQRA2 end point response of the flexible arm and 23% end mass with a target end point position of 45 degrees

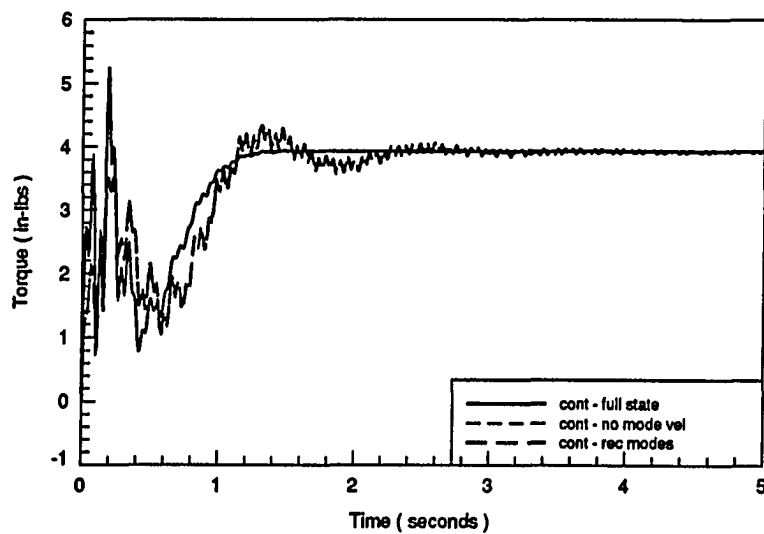


Figure 4.42: LQRA2 torque response of the flexible arm and 23% end mass with a target end point position of 45 degrees

Figures 4.43 and 4.44 show the responses of the flexible arm and 64% end mass. Figure 4.43 shows the full state response has a rise time of 1.6 seconds and no overshoot. The other responses show a rise time of 1.1 seconds and oscillations. These responses have not settled by the end of the 5 second simulation. Figure 4.44 gives the torque responses. The full state feedback case is limited by the 8.5 in-lb limit. The other cases are not.

The stability parameter is now increased to 3. The weighting factors given in equations 4.21 and 4.22 are used again. The modified Riccati equation is solved for each of the end masses. A target end point position of 45 degrees is assumed. This algorithm will be referred to as LQRA3.

Figures 4.45 and 4.46 give the end point and torque responses for the unloaded arm. Figure 4.45 shows the full state feedback law gives a rise time of 0.7 seconds with no overshoot. The other cases have a rise time of 0.5 seconds, and overshoot of 3 degrees and a settling time of 2 seconds. Figure 4.46 gives the torque responses. The full state feedback law gave the smoothest response and highest peak torque of 5 in-lbs. The case of feeding back the recreated states resulted in a small amount of oscillation due to observation spillover.

Figures 4.47 and 4.48 give the end point and torque responses for the 23% end mass and arm. Figure 4.47 gives the end point responses. The full state feedback shows a rise time of 0.9 seconds with no overshoot. The other cases have a rise time of 0.6 seconds, 5 degree overshoot, and a settling time of 4 seconds. Figure 4.48 shows the torque response of the full state feedback case is affected for short periods by the 8.5 in-lb limit. The other cases are not affected by the limit.

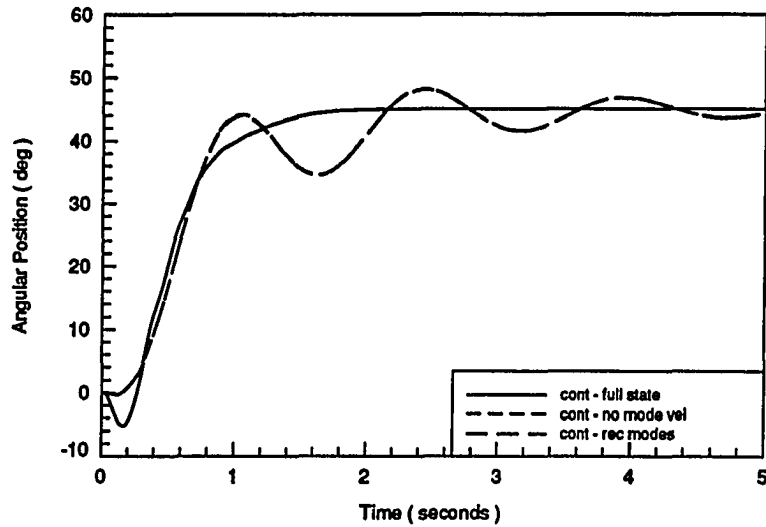


Figure 4.43: LQRA2 end point response of the flexible arm and 64% end mass with a target end point position of 45 degrees

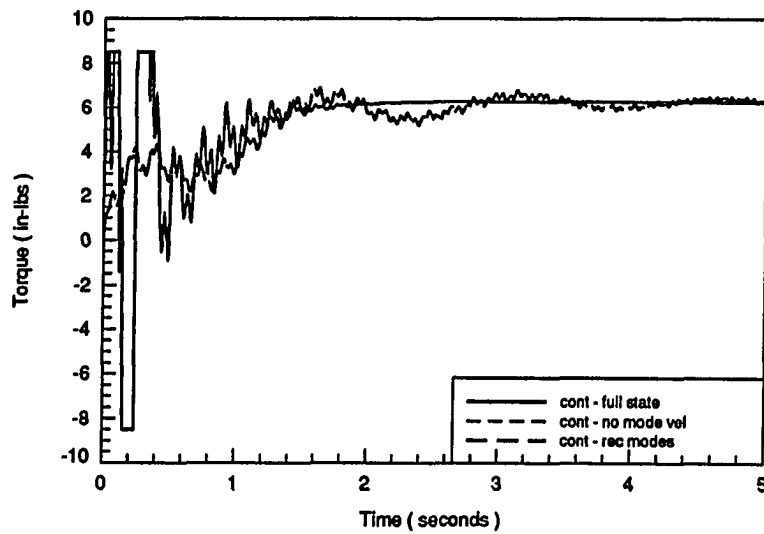


Figure 4.44: LQRA2 torque response of the flexible arm and 64% end mass with a target end point position of 45 degrees

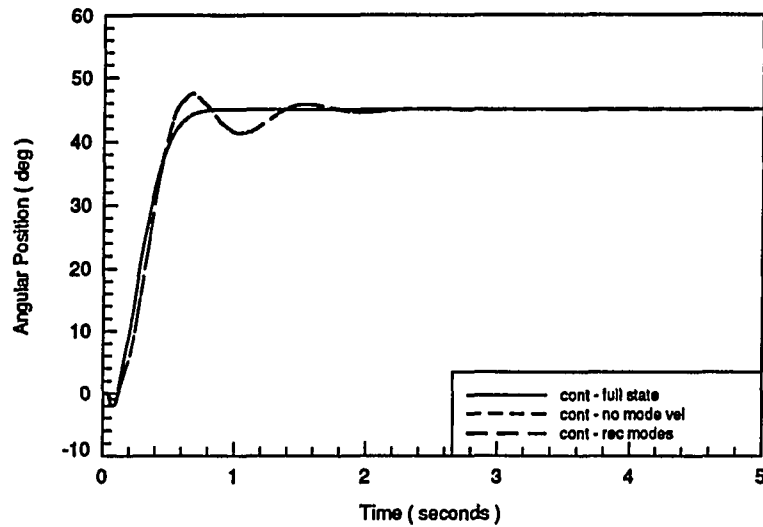


Figure 4.45: LQRA3 end point response of the unloaded flexible arm with a target end point position of 45 degrees

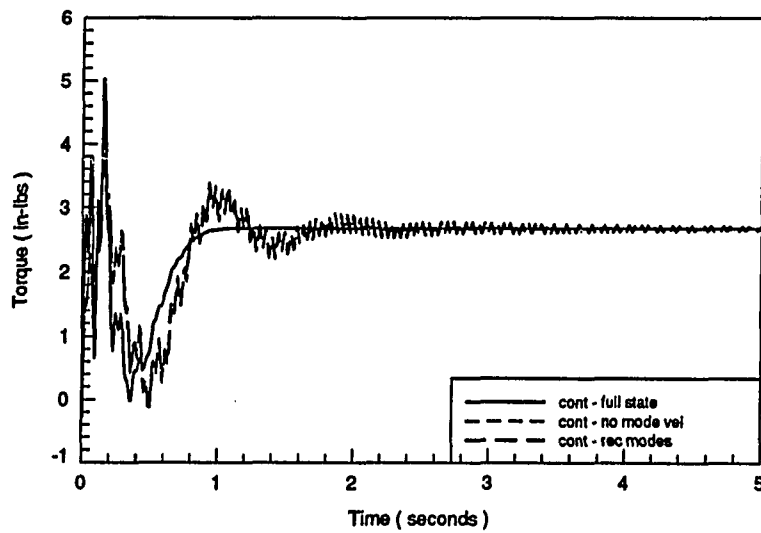


Figure 4.46: LQRA3 torque response of the unloaded flexible arm with a target end point position of 45 degrees

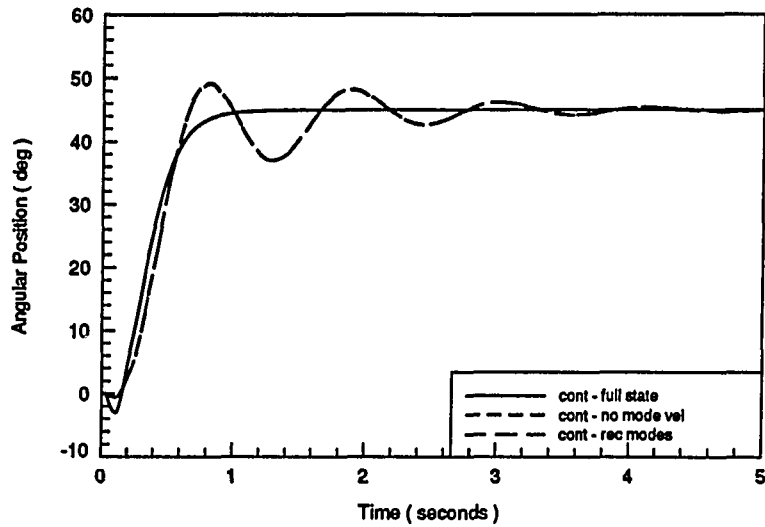


Figure 4.47: LQRA3 end point response of the flexible arm and 23% end mass with a target end point position of 45 degrees

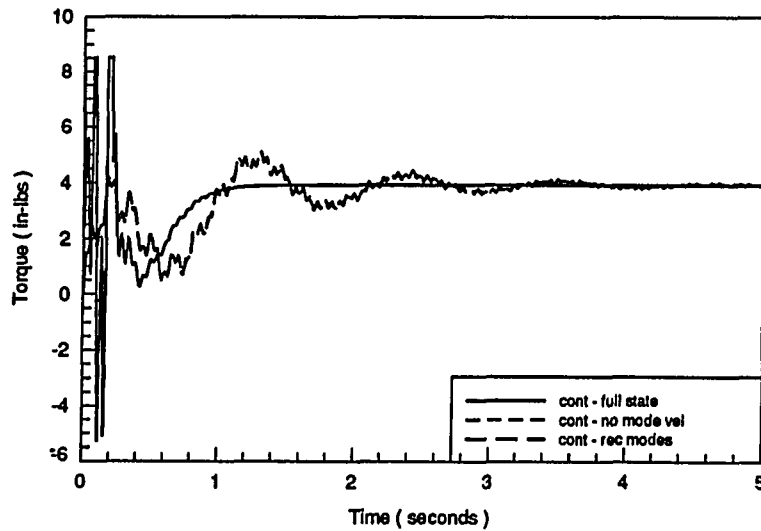


Figure 4.48: LQRA3 torque response of the flexible arm and 23% end mass with a target end point position of 45 degrees

Figures 4.49 and 4.50 show the responses for the 64% end mass case. Figure 4.49 shows the response of the end point. The full state feedback case is unstable. The other cases have a rise time of 0.8 seconds and an initial overshoot of 8 degrees. The response has not settled at the end of the 5 second simulation. Figure 4.50 shows the torque response of the full state feedback case is affected by the 8.5 in-lb limit. The other cases are not limited.

4.7 Summary of Results

Tables 4.4, 4.5, 4.6, 4.7, and 4.8, summarize the results of the control algorithms. The PD controller has larger overshoots and settling times than the LQR controllers. The LQR controllers are sensitive to the weighting factors in Q and R . It was found that the best results are obtained when the weighting factors are modified for each payload. The final target state also affects the best weighting factors, but to a smaller degree. The LQR with prescribed degree of stability can result in better responses. However, large values of α produce unstable results in nonlinear simulations with the torque limitation.

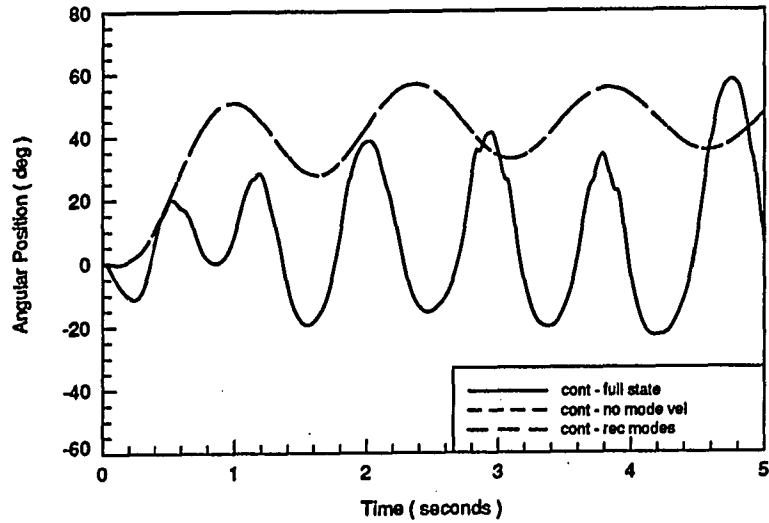


Figure 4.49: LQRA3 end point response of the flexible arm and 64% end mass with a target end point position of 45 degrees

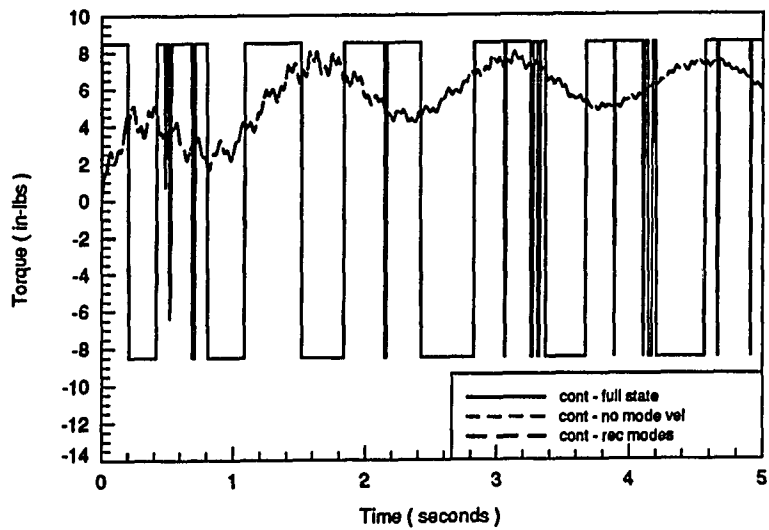


Figure 4.50: LQRA3 torque response of the flexible arm and 64% end mass with a target end point position of 45 degrees

Table 4.4: Summary of the responses of the flexible arm and payloads using the PD control algorithm

target end point (deg)	payload (% of arm mass)	rise time (sec)	overshoot (deg) (%)		settling time (sec)	torque limited
45	0	0.4	14	31	2.5	no
45	23	0.5	25	56	>5	no
45	64	0.5	42	93	>5	yes
90	0	0.4	50	56	2.5	no
90	23	0.6	70	78	>5	no
90	64	0.7	60	67	>5	yes

Table 4.5: Summary of the responses of the flexible arm and payloads using the LQRA control algorithm

control algorithm	target end point (deg)	payload (% of arm mass)	rise time (sec)	overshoot		settling time (sec)	torque limited
				(deg)	(%)		
full state	45	0	1.0	0	0	2.0	no
no mode vel	45	0	1.0	0	0	1.5	no
rec mode	45	0	1.0	0	0	1.5	no
full state	45	23	0.9	4	9	2.5	no
no mode vel	45	23	0.85	6	13	2.0	no
rec mode	45	23	0.85	6	13	2.0	no
full state	45	64	0.85	13	29	>5	no
no mode vel	45	64	0.75	17	38	>5	no
rec mode	45	64	0.75	17	38	>5	no
full state	90	0	0.8	1	1	2.0	no
no mode vel	90	0	1.0	0	0	1.0	no
rec mode	90	0	1.0	0	0	1.0	no
full state	90	23	0.8	10	11	2.0	no
no mode vel	90	23	0.8	8	9	2.5	no
rec mode	90	23	0.8	8	9	2.5	no
full state	90	64	0.9	24	27	>5	yes
no mode vel	90	64	0.9	26	29	>5	yes
rec mode	90	64	0.9	26	29	>5	yes

Table 4.6: Summary of the responses of the flexible arm and payloads using the LQRB control algorithm

control algorithm	target end point (deg)	payload (% of arm mass)	rise time (sec)	overshoot		settling time (sec)	torque limited
				(deg)	(%)		
full state	45	0	4.0	0	0	4.0	no
no mode vel	45	0	4.0	0	0	4.0	no
rec mode	45	0	4.0	0	0	4.0	no
full state	45	23	4.0	0	0	4.0	no
no mode vel	45	23	4.0	0	0	4.0	no
rec mode	45	23	4.0	0	0	4.0	no
full state	45	64	1.2	0	0	3.0	no
no mode vel	45	64	1.0	1	2	2.6	no
rec mode	45	64	1.0	1	2	2.6	no
full state	90	0	4.0	0	0	4.0	no
no mode vel	90	0	4.0	0	0	4.0	no
rec mode	90	0	4.0	0	0	4.0	no
full state	90	23	4.0	0	0	4.0	no
no mode vel	90	23	4.0	0	0	4.0	no
rec mode	90	23	4.0	0	0	4.0	no
full state	90	64	0.9	17	19	>5	yes
no mode vel	90	64	0.95	15	17	>5	yes
rec mode	90	64	0.95	15	17	>5	yes

Table 4.7: Summary of the responses of the flexible arm and payloads using the LQRA2 control algorithm

control algorithm	target end point (deg)	payload (% of arm mass)	rise time (sec)	overshoot		settling time (sec)	torque limited
				(deg)	(%)		
full state	45	0	0.7	0	0	0.7	no
no mode vel	45	0	0.6	1	2	1.4	no
rec mode	45	0	0.6	1	2	1.4	no
full state	45	23	0.9	0	0	0.9	no
no mode vel	45	23	0.8	1	2	2.0	no
rec mode	45	23	0.8	1	2	2.0	no
full state	45	64	1.6	0	0	1.6	yes
no mode vel	45	64	1.1	5	11	>5	no
rec mode	45	64	1.1	5	11	>5	no

Table 4.8: Summary of the responses of the flexible arm and payloads using the LQRA3 control algorithm

control algorithm	target end point (deg)	payload (% of arm mass)	rise time (sec)	overshoot		settling time (sec)	torque limited	
				(deg)	(%)			
full state	45	0	0.7	0	0	0.7	no	
no mode vel	45	0	0.5	3	7	2.0	no	
rec mode	45	0	0.5	3	7	2.0	no	
full state	45	23	0.9	0	0	0.9	yes	
no mode vel	45	23	0.6	5	11	4.0	no	
rec mode	45	23	0.6	5	11	4.0	no	
full state	45	64	unstable					yes
no mode vel	45	64	0.8	8	18	>5	no	
rec mode	45	64	0.8	8	18	>5	no	

5. EXPERIMENTAL TEST BED AND RESULTS

This chapter describes the experimental test bed and calibration procedure and presents experimental results. Section 5.1 gives the description of the experimental test bed. Section 5.2 describes the instrument calibration procedure. Section 5.3 presents experimental results from the PD control algorithm. Section 5.4 presents the experimental results from control algorithms that use modal feedback. Section 5.5 gives a summary of the experimental results.

5.1 Description of Experimental Test Bed

A schematic diagram of the experimental rig is shown in Figure 5.1. Photographs are given in Figures 5.2 and 5.3. The main component of the experimental system is a Zenith 386/33 personal computer with a 30387 math coprocessor. The digital to analog and analog to digital board in the personal computer is a National Instruments AT-MIO-16-L9. This board has the capacity to sample eight differential channels and output two analog signals.

The brushless DC servo motor and controller are Electrocraft models S4050 and BRU200, respectively. The motor has a stall torque of 60 inch-pounds, which is more than sufficient for this application. The motor system has a 1 millisecond delay that is inherent in the system and cannot be changed. The torque frequency response of

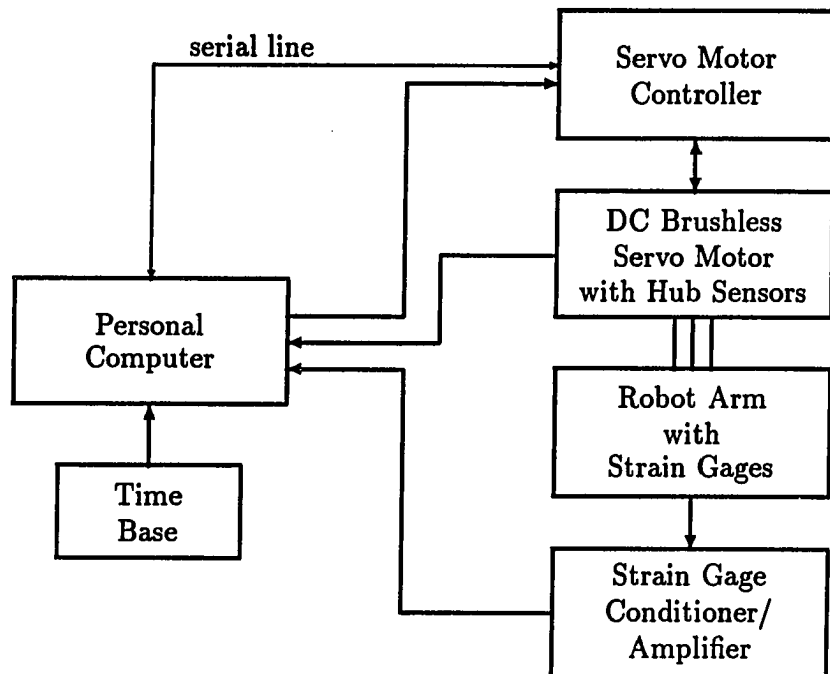


Figure 5.1: Schematic diagram of experimental station

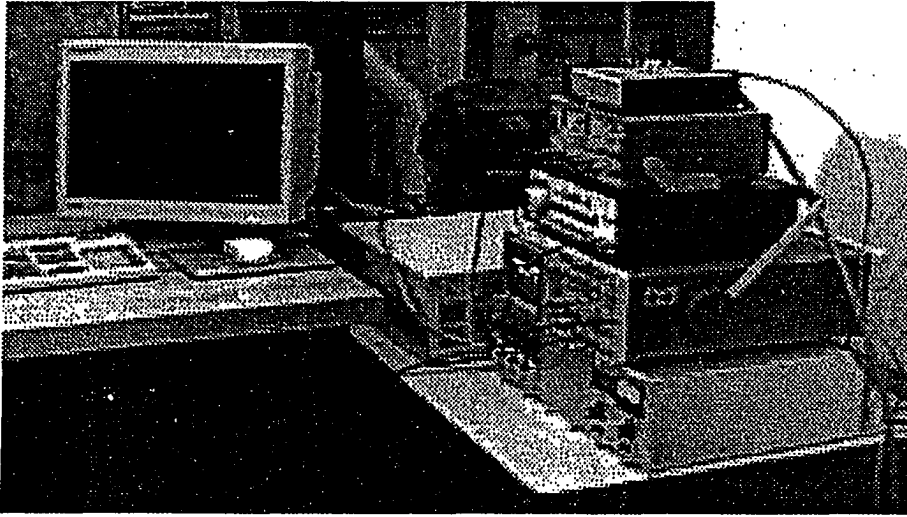


Figure 5.2: Experimental station showing the electronic equipment

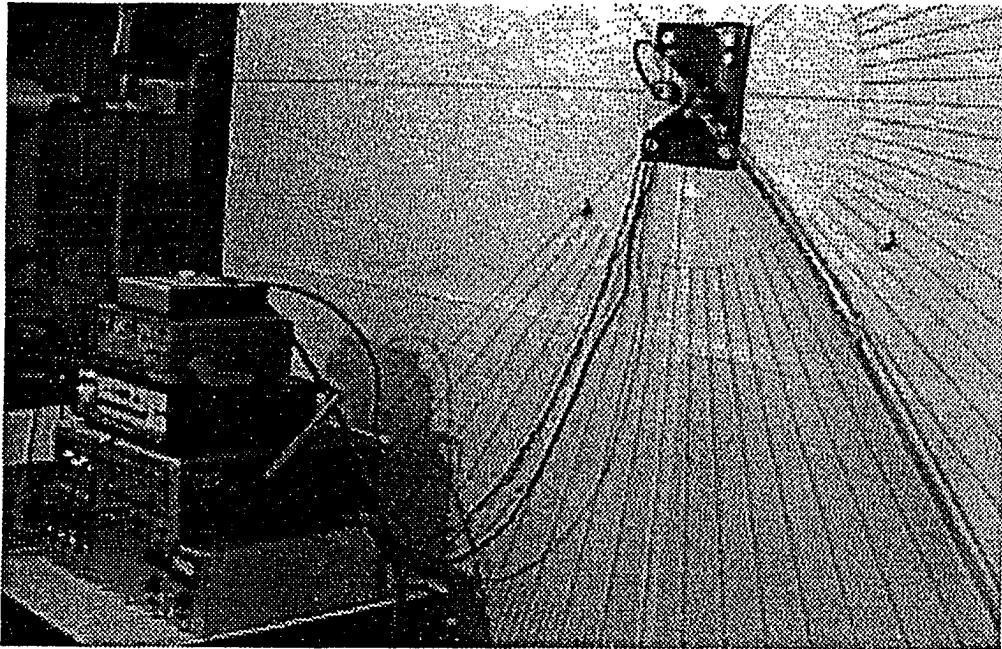


Figure 5.3: Experimental station with the flexible arm

the motor-controller system is flat until 10 Hz. From this point on, the magnitude drops significantly. The phase response also degrades around 10 Hz. The maximum time lag occurs at approximately 25 Hz.

The motor does have an integral optical encoder for position and velocity measurement. However, it has a resolution of only 240 pulses per revolution. This was determined to be of insufficient accuracy. To determine the position of the hub, a Beckman Instruments 500 ohm single turn potentiometer is mounted to the back of the motor. The potentiometer has a resolution of approximately 0.2 degrees. The dead point in the potentiometer is located in a position outside of the expected range of travel.

To obtain the hub velocity, the optical encoder again could not be used for the expected range of motion. Also, tachometers could not be used due to the low speeds. A gear train could have been implemented to increase the speeds, but the drawbacks of backlash, friction, and inertia were considered to be too great. Various methods of obtaining a velocity signal from the position signal were experimented with including analog filtering and differentiation followed by digital filtering, analog filtering followed by digital differentiation and filtering. After much experimentation, these methods were dropped in favor of installing a small dc motor on the main servo motor shaft. The small motor, used as a generator, develops a voltage signal proportional to the velocity of the shaft.

The strain gages are Measurements Group, Micro-Measurements Division EA-06-250BF-350. The strain gage conditioner/amplifier is a Measurements Group, Instruments Division 2120A.

The time base in Figure 5.1 is used to trigger the computer. In practice a variable frequency square wave generator is used. When the rising edge of the square wave is detected, all of the inputs are sampled and passed to the control algorithm. The required operations are performed and a control signal output. The output is then converted to an analog signal by the D-A board and output to the servo motor controller.

The software supplied with the data acquisition board is rather slow when used in this control application. Using it as supplied to repetitively sample eight differential channels, perform 1000 multiplies, and output a voltage, results in a maximum operating frequency of approximately 100 Hz. By writing software that directly accesses specific memory locations and by disabling all unnecessary computer functions, the maximum operating frequency while performing 1000 multiplies is increased by a factor of three to approximately 300 Hz.

For this work, the number of multiplies is minimized and the computer is able to operate at 1000 Hz with some dead time in each cycle. The maximum operating frequency could be increased to approximately 1500 Hz, but 1000 Hz allows for possible increases in the number of multiplies used for the control algorithm.

For purposes of evaluating system performance, the position of the end point is determined by examining video taken of the robot arm during the control cycles. The examination is performed off-line frame by frame. This gives a reasonably accurate record of the motion of the end point.

5.2 Calibration Procedure

This section describes the procedure used to calibrate the instruments. This is a multi-step process that must be completed in sequential order. The steps are:

1. Load a file containing the target static equilibrium state, feedback gains, and matrix to convert the measured strains to magnitudes of mode shapes into the control program.
2. Calibrate the potentiometer. The position signal is sampled with the hub positioned at zero and again with the hub positioned at 90 degrees. These two readings are used to determine the offset and scaling factor necessary to convert the voltage signal into angular position.
3. Calibrate the dc electric generator. The voltage signal is sampled when the hub is stationary. This determines the constant offset to add to the signal to zero the angular velocity. To determine the scaling factor to convert the voltage signal to angular velocity, the arm is raised to some value greater than 100 degrees and dropped. While the arm is moving downward, the angular position and velocity signals are sampled at 1000 Hz. The angular velocity signal is numerically integrated between the angles of 90 and 0 degrees. This quantity is set equal to the change in angular position. This may be written as:

$$\theta_1 - \theta_2 = c_v \sum_i v(i) \delta t \quad (5.1)$$

In this application, equation 5.1 can be rewritten as:

$$c_v = \frac{-\frac{\pi}{2}}{\sum_i v(i) \times 0.001} \quad (5.2)$$

4. Calibrate the strain gages. The hub is positioned to zero with the arm at rest. Data is taken to determine the offsets that are necessary to obtain the zero points. The hub is then repositioned so that the end point of the arm is at 90 degrees. The strain signals are sampled and compared to known strain values. This establishes the scaling factor necessary to convert the voltage signals into strains.
5. If desired, the recorder can be enabled. When in use, the sampled quantities are placed in an array while the arm is being controlled. After the control cycle is finished, the data is written to the hard drive.
6. If desired, the feedback gains and target static equilibrium states may be changed interactively.

After this procedure has been completed, the control algorithms are implemented in the test bed. The 8.5 in-lb limit discussed in Chapter 4 is enforced during the experiments. The next section presents the results obtained from using the PD control algorithm.

5.3 Proportional-Derivative Experimental Results

This section presents the experimental results obtained from the PD control laws developed in Chapter 4.

Figures 5.4 and 5.5 give the responses of the end point and hub of the unloaded arm with a target end point of 45 degrees. Results of two control algorithms are given. The first uses only hub position feedback while the other uses both hub position and velocity feedback. Figure 5.4 shows the end point response of the unloaded arm. The

position only response gives a rise time of 0.3 seconds, an overshoot of 36 degrees, and a steady state error of 3 degrees. The PD control algorithm gives a rise time of 0.45 seconds, an overshoot of 8 degrees, steady state error of -7 degrees, and a settling time of 4 seconds.

Figures 5.6 and 5.7 give the responses of the end point and hub of the flexible arm and 23% end mass with a target position of 45 degrees. The position only control shows a rise time of 0.3 seconds, a 43 degrees overshoot, and a steady state error of 2 degrees. The PD controller gives a rise time of 0.5 seconds, 5 degree overshoot, and a steady state error of 3 degrees. The settling time is 4 seconds.

Figures 5.8 and 5.9 give the responses of the end point and hub of the flexible arm and 64% end mass with a target position of 45 degrees. In this case, the plots give three responses. The PD controller using the gains developed in the numerical development for this case resulted in slightly unstable responses. This can be seen in Figure 5.9. The response labeled "pd control unstable" shows high frequency motion. This motion does not damp out. The velocity gain is decreased by 25% in the second PD control response curves. In this case, the arm does not exhibit the high frequency vibration. Figure 5.8 shows the position only end point response has a rise time of 0.5 seconds, overshoot of 37 degrees, and steady state error of 7 degrees. The stable PD controller gives a rise time of 0.6 seconds and overshoot of 13 degrees. The steady state error is 11 degrees.

Figures 5.10 and 5.11 give the responses for the unloaded arm with a target position of 90 degrees. The position only controller gives a response time of 0.4 seconds, 55 degree overshoot, and a settling time of approximately 3.8 seconds. The steady state error is 2 degrees. The PD controller shows a response time of 0.5 sec-

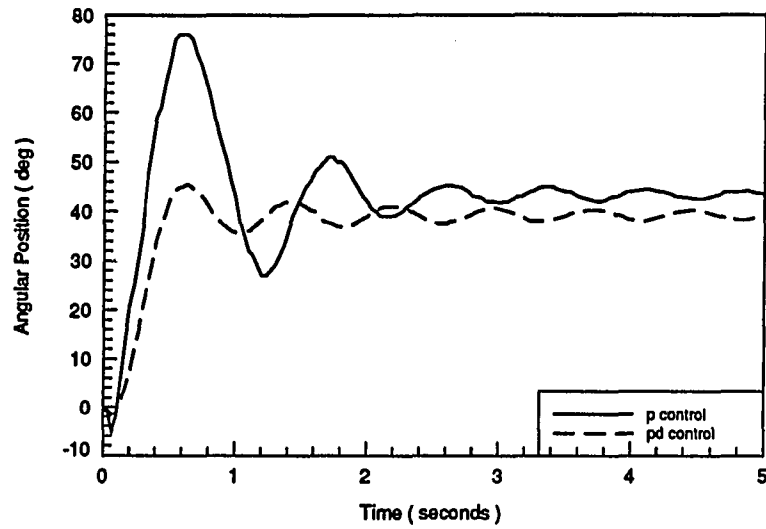


Figure 5.4: Experimental PD end point response of the unloaded arm with a target end point position of 45 degrees

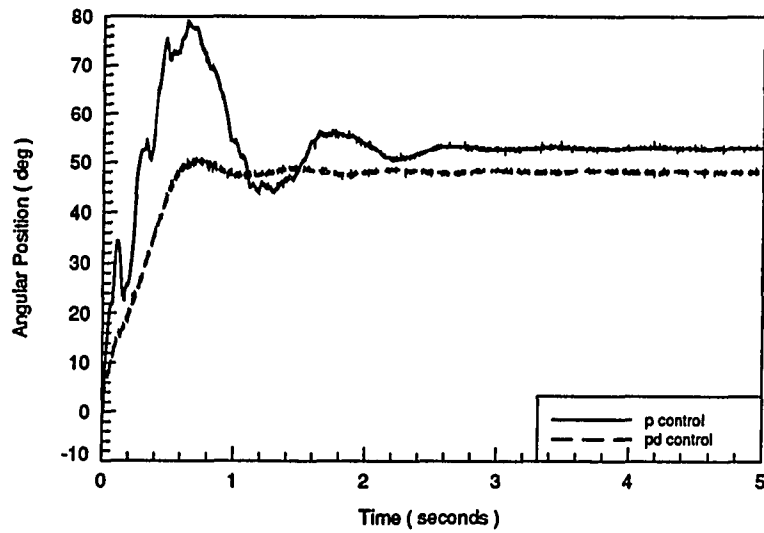


Figure 5.5: Experimental PD hub position response of the unloaded arm with a target end point position of 45 degrees

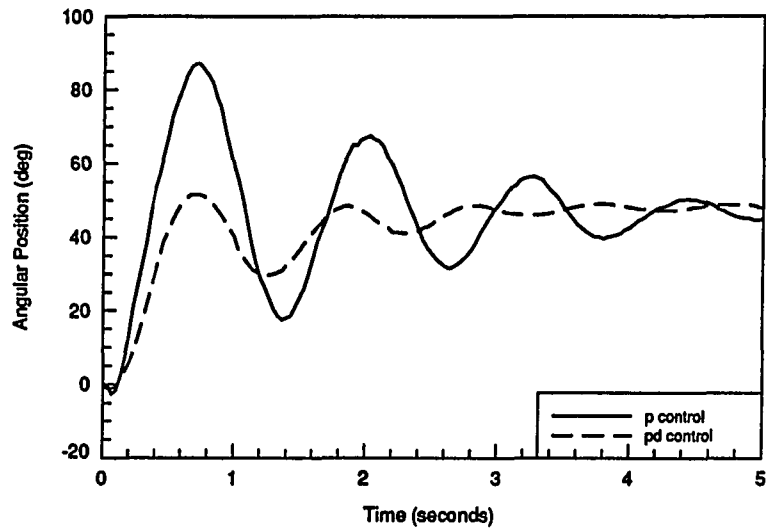


Figure 5.6: Experimental PD end point response of the flexible arm and 23% load with a target end point position of 45 degrees

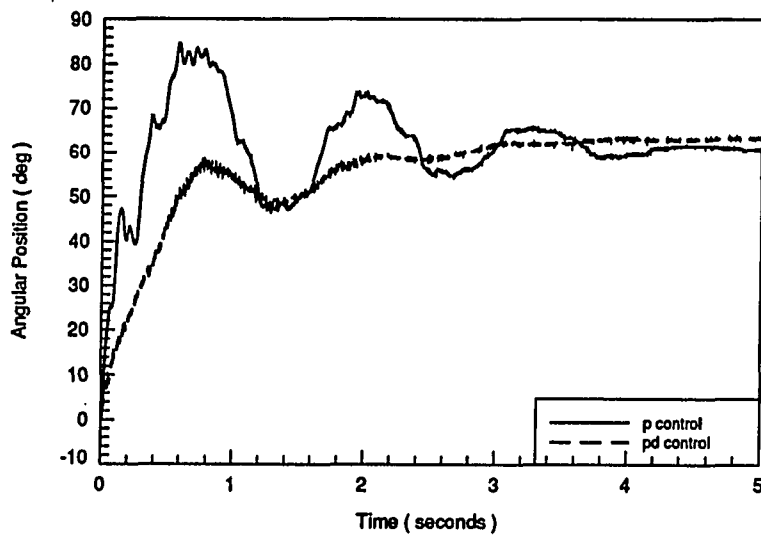


Figure 5.7: Experimental PD hub position response of the flexible arm and 23% load with a target end point position of 45 degrees

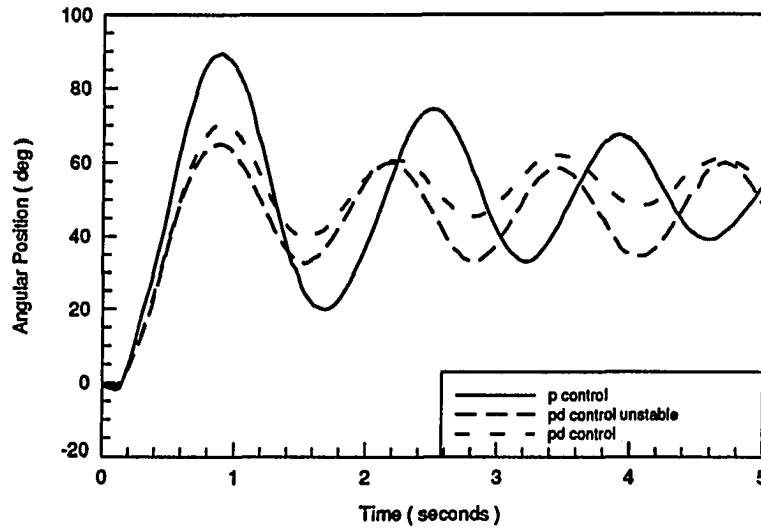


Figure 5.8: Experimental PD end point response of the flexible arm and 64% load with a target end point position of 45 degrees

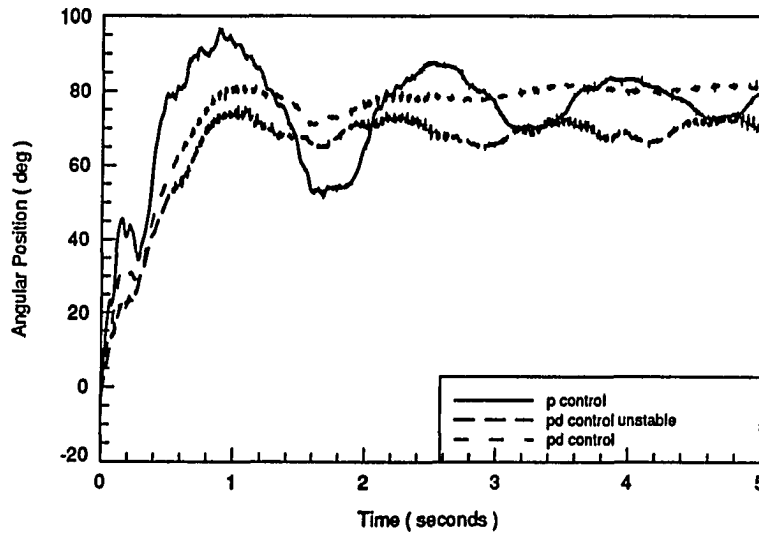


Figure 5.9: Experimental PD hub position response of the flexible arm and 64% load with a target end point position of 45 degrees

onds, 12 degree overshoot, settling time of 3 seconds, and a 3 degree steady state error. Figure 5.11 shows the hub position responses exhibit very little high frequency motion.

Figures 5.12 and 5.13 give the responses of the flexible arm with 23% end mass and a target position of 90 degrees. The position only controller shows a rise time of 0.5 seconds and 63 degree overshoot. The steady state error is 2 degrees. It does not settle within 5 seconds. The PD controller shows a rise time of 0.5 seconds and 22 degree overshoot. The settling time is larger than 5 seconds. The steady state error is -4 degrees. Figure 5.13 shows the hub angle does exhibit some high frequency motion between 0.75 and 1.4 seconds. The high frequency motion does diminish.

Figures 5.14 and 5.15 give the responses of the flexible arm with 64% end mass and a target position of 90 degrees. Both control algorithms give 0.7 second rise times and -18 degree steady state errors. The position only controller gives an overshoot of 70 degrees and a 4 second settling time. The PD controller gives a 45 degree overshoot and a 3.6 second settling time. Figure 5.15 shows the hub angle response exhibits a period of high frequency motion from 1 to 1.5 seconds. The end point in both cases exhibited significant out of plane motion.

5.4 Modal Feedback Experimental Results

This section presents the results of including mode shapes in the feedback control laws. The feedback gains obtained from the linear quadratic regulators in Chapter 4 are implemented in the test bed. This linear control algorithm will be referred to as the flexible control (FC) algorithm. Each figure shows the responses of three linear FC algorithms and one nonlinear FC algorithm. The first linear scheme uses

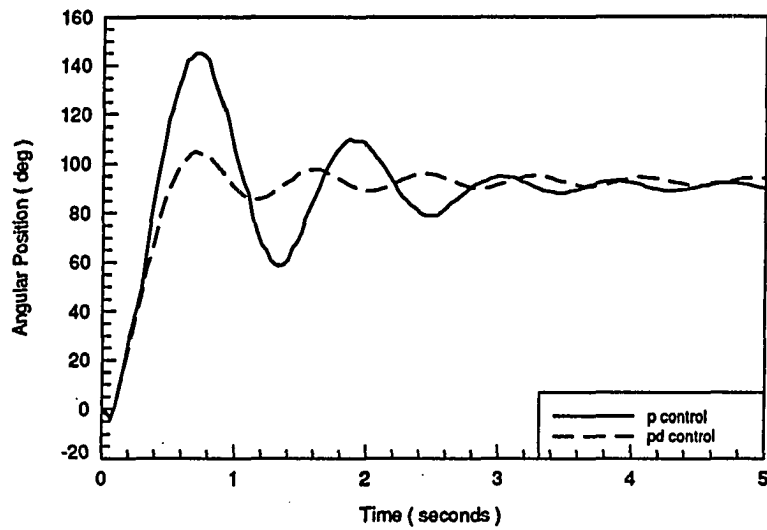


Figure 5.10: Experimental PD end point response of the unloaded arm with a target end point position of 90 degrees

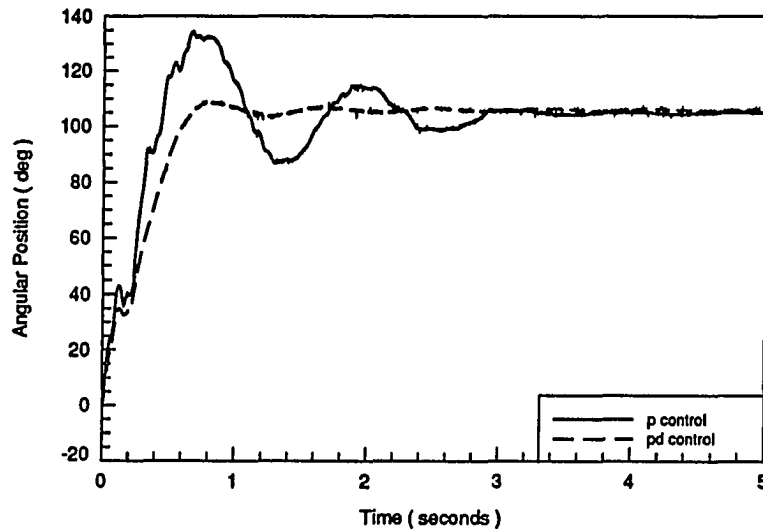


Figure 5.11: Experimental PD hub position response of the unloaded arm with a target end point position of 90 degrees

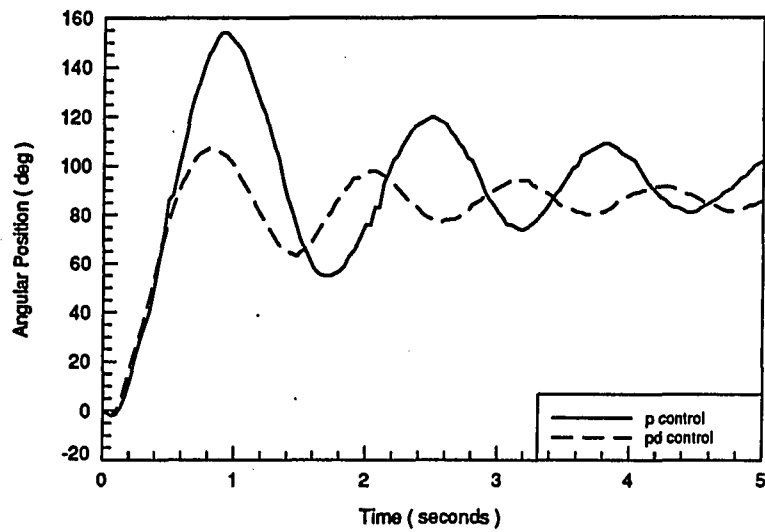


Figure 5.12: Experimental PD end point response of the flexible arm and 23% load with a target end point position of 90 degrees

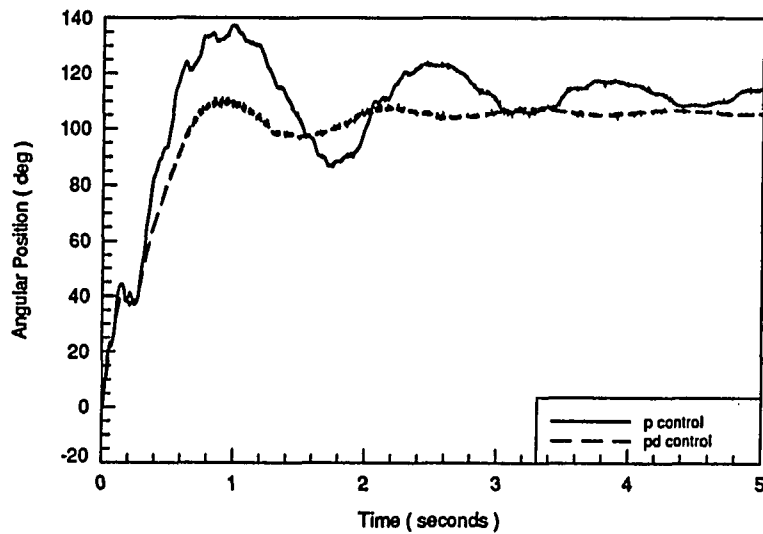


Figure 5.13: Experimental PD hub position response of the flexible arm and 23% load with a target end point position of 90 degrees

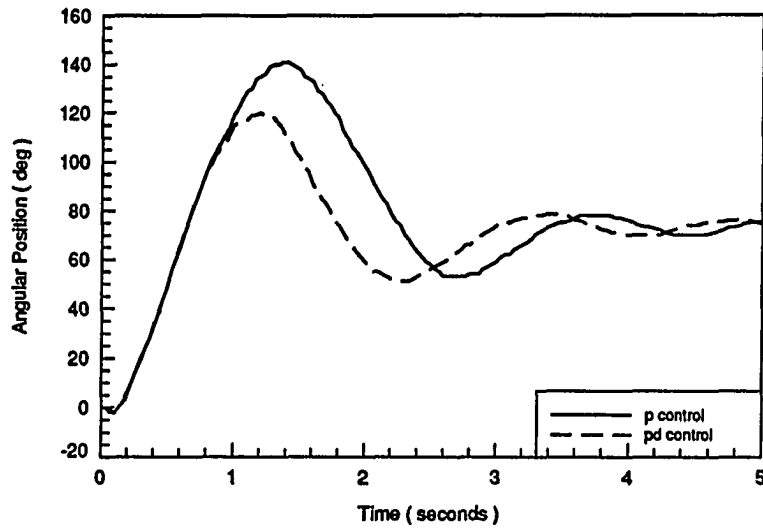


Figure 5.14: Experimental PD end point response of the flexible arm and 64% load with a target end point position of 90 degrees

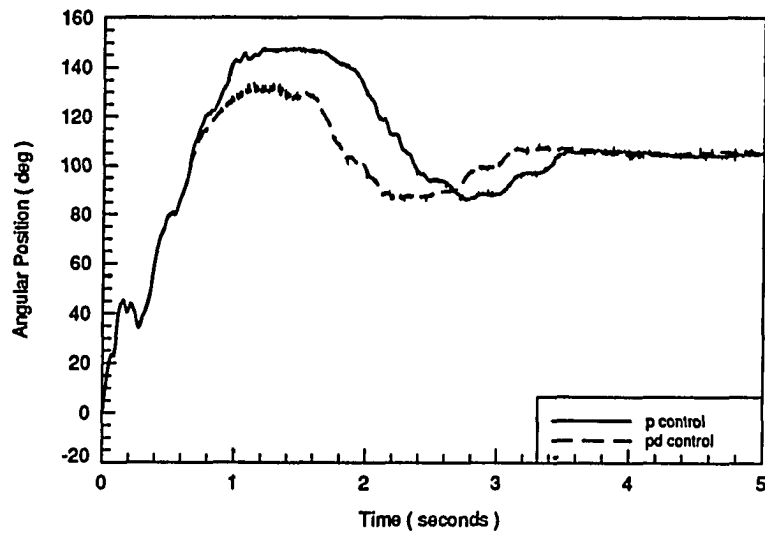


Figure 5.15: Experimental PD hub position response of the flexible arm and 64% load with a target end point position of 90 degrees

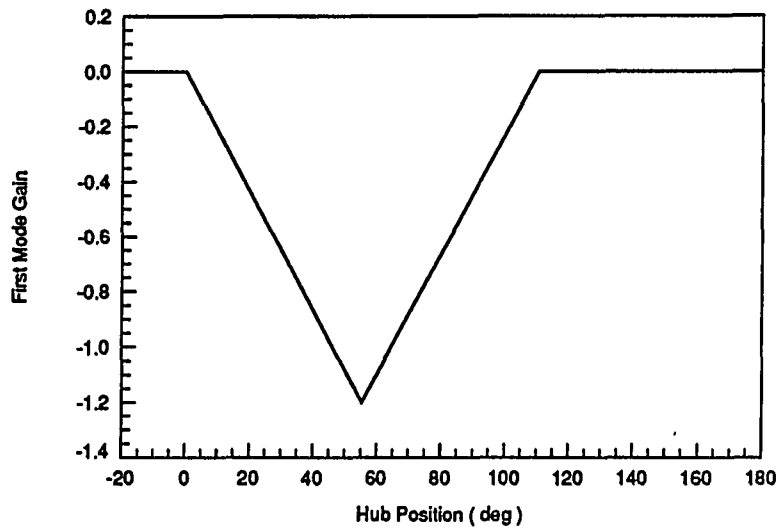


Figure 5.16: NLFC first mode gain as a function of hub position

feedback from two mode shapes. The second uses no feedback from the modes. This is essentially a PD controller that uses the same hub position and velocity gains as the other FC algorithms. The third response does not use second mode feedback. The last flexible controller is nonlinear and will be referred to as NLFC. This control algorithm utilizes both flexible modes in the feedback law. The nonlinearity is due to the first mode gain dependency on the hub position. Figure 5.16 shows the dependency for the unloaded arm with a target 45 degree end point position. The gain is set to zero when the hub angle is negative. The gain linearly increases as a function of hub angle from zero to the desired steady state. The gain then linearly decreases until a hub angle of two times the steady state value is reached. At larger hub angles, the gain is again zero. In Figure 5.16, the first mode gain is negative.

Figures 5.17 and 5.18 give the responses of the unloaded arm with a 45 degree target end point position. The results are summarized in Table 5.1. The FC with no

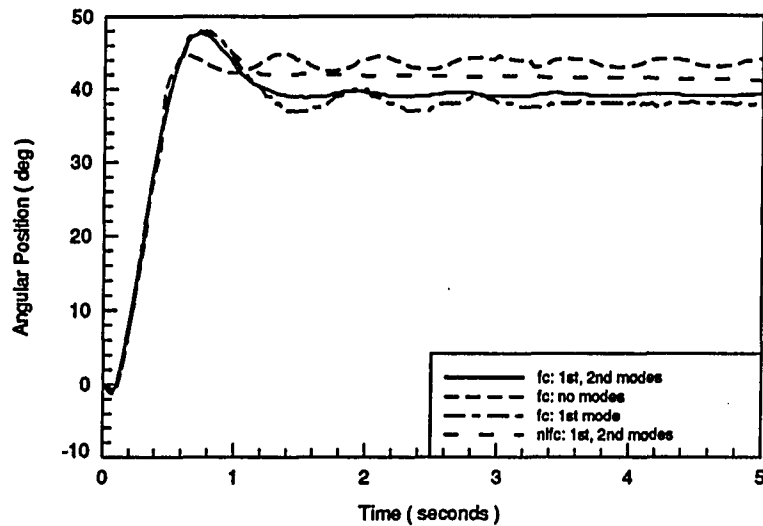
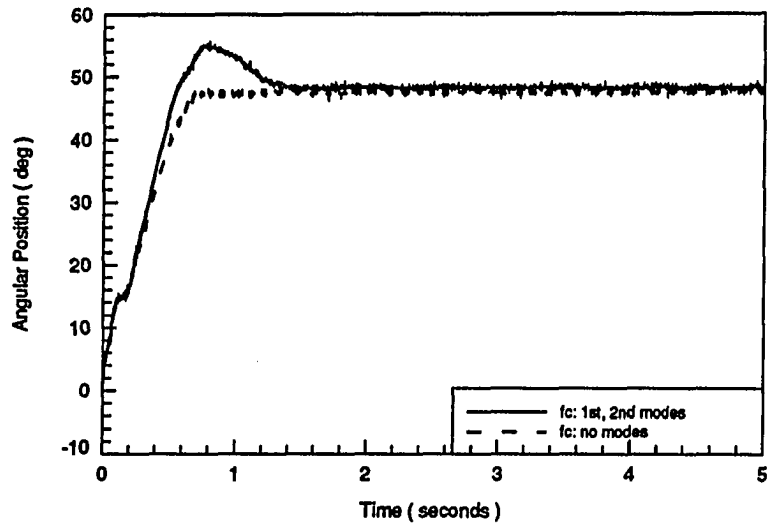


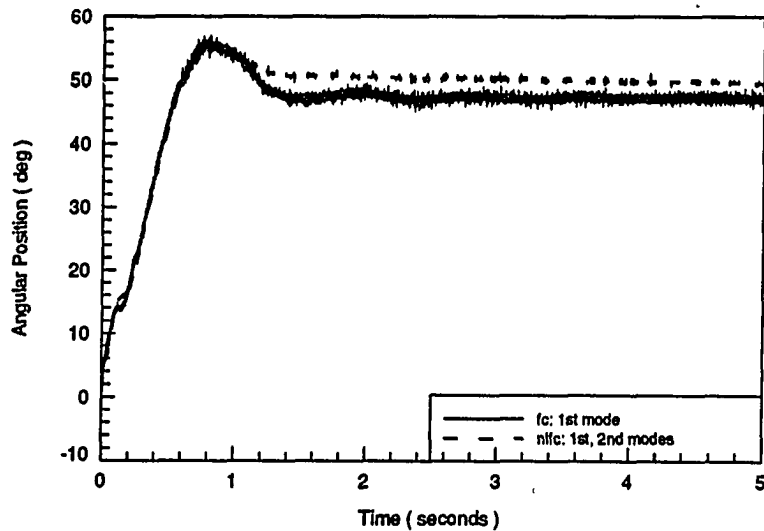
Figure 5.17: Experimental FC end point response of the unloaded arm with a target end point position of 45 degrees

modal feedback gives the smallest overshoot, but a large settling time. The NLFC results in the shortest settling time and the second smallest overshoot. Figure 5.18 shows the hub angle responses. The FC with first mode feedback shows a high frequency instability. This instability results in a sixth mode vibration in the arm. The other response have stable hub angle responses.

Figures 5.19 and 5.20 give the responses of the flexible arm and 23% end mass with a target end point position of 45 degrees. The results are summarized in Table 5.2. The FC with first mode feedback results in the shortest response time. This is due to its low steady state value. The rise times for the other algorithms are practically identical. The linear FC with first and second mode feedback gives the shortest settling time. Figure 5.20 shows the high frequency instability of the FC



(a)



(b)

Figure 5.18: Experimental FC hub position response of the unloaded arm with a target end point position of 45 degrees

Table 5.1: Summary of the FC experimental responses of the unloaded arm with a target end point position of 45 degrees.

algorithm	rise time (sec)	overshoot		settling time (sec)	steady state error	
		(deg)	(%)		(deg)	(%)
FC, 1st & 2nd modes	0.5	8	22	1.3	-6	-13
FC, no modes	0.55	2	5	3.5	-2	-4
FC, 1st mode	0.5	9	24	3.0	-7	-16
NLFC	0.52	6	14	1.1	-3	-7

with first mode feedback algorithm. The other hub angle responses do not show this instability.

Figures 5.21 and 5.22 give the responses of the flexible arm and 64% end mass with a target end point position of 45 degrees. The results are summarized in Table 5.3. The algorithms do not produce good results. All of the settling times are longer than 5 seconds with significant overshoot. Figure 5.22 shows the high frequency instability of the FC with first mode feedback algorithm. In this case, the instability is not as pronounced. However, the high frequency vibration occurs. Again, the other cases do not have the instability.

Figures 5.23 and 5.24 give the responses of the unloaded arm with a 90 degree target end point position. The results are summarized in Table 5.4. The best responses are from the FC with first and second modes and the NLFC. Both give almost identical results. The difference is the NLFC exhibits a smaller overshoot. The FC with no modal feedback gives the smallest overshoot and the longest settling time.

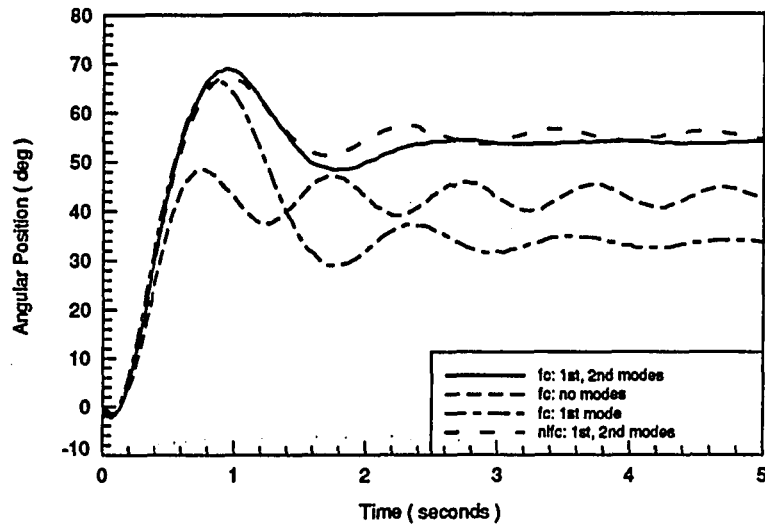
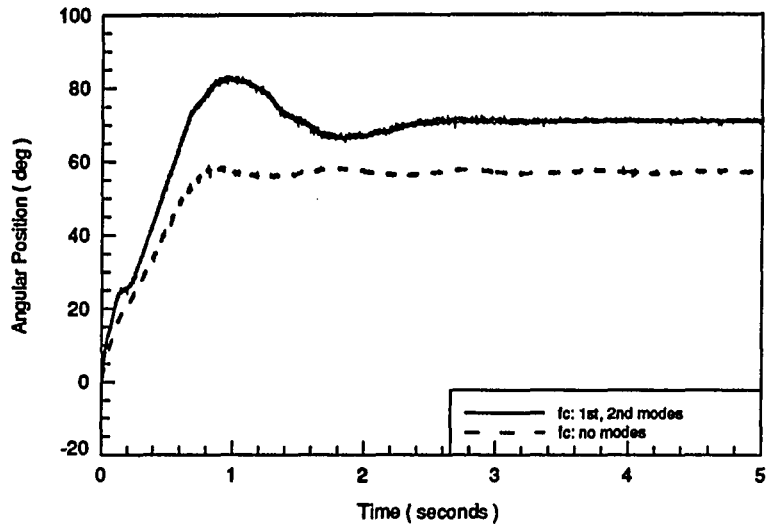


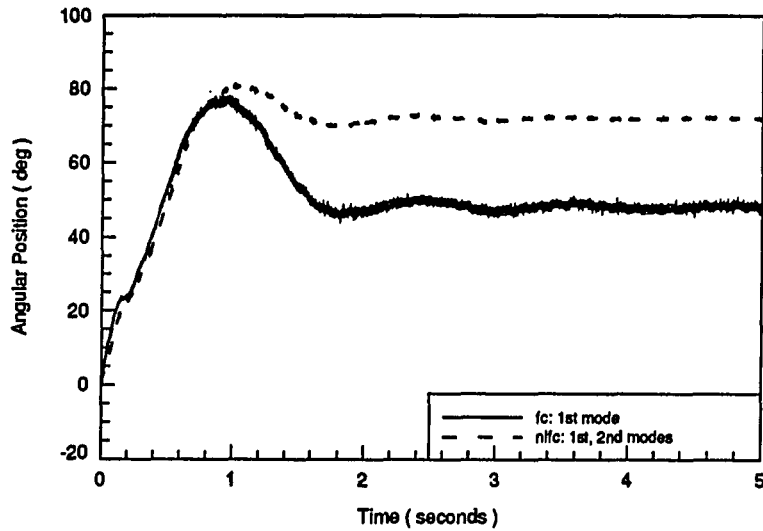
Figure 5.19: Experimental FC end-point response of the flexible arm and 23% load with a target end point position of 45 degrees

Table 5.2: Summary of the FC experimental responses of the flexible arm and 23% load with a target end point position of 45 degrees.

algorithm	rise time (sec)	overshoot		settling time (sec)	steady state error	
		(deg)	(%)		(deg)	(%)
FC, 1st & 2nd modes	0.6	14	26	2.4	9	20
FC, no modes	0.6	4	9	>5	-1	-2
FC, 1st mode	0.4	32	94	3.8	-11	-24
NLFC	0.6	12	21	4.2	11	24



(a)



(b)

Figure 5.20: Experimental FC hub position response of the flexible arm and 23% load with a target end point position of 45 degrees

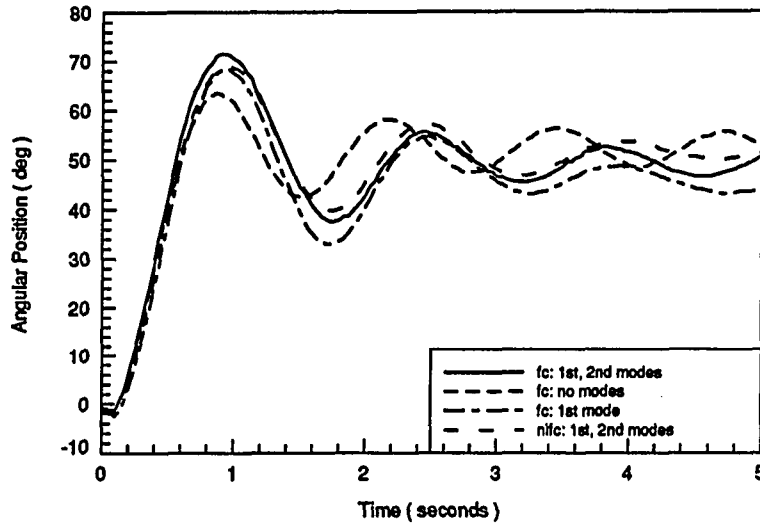
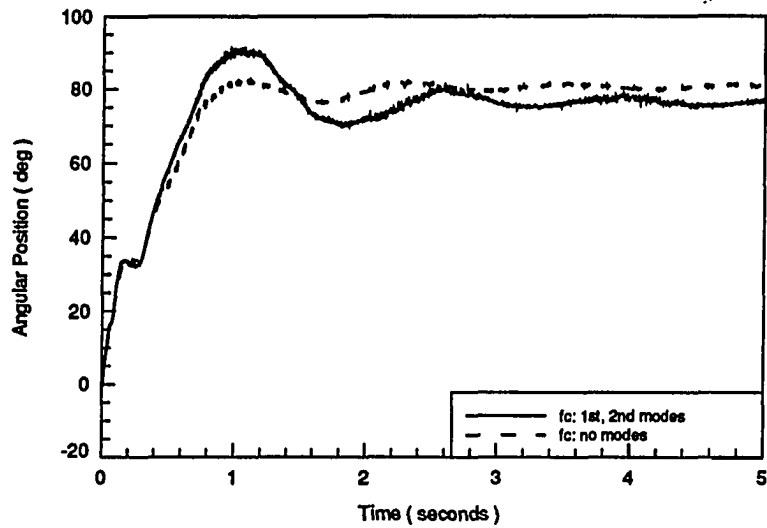


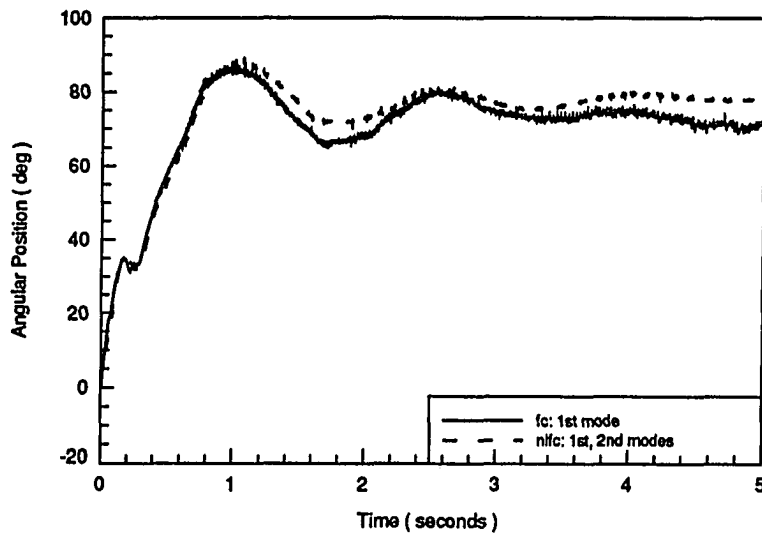
Figure 5.21: Experimental FC end point response of the flexible arm and 64% load with a target end point position of 45 degrees

Table 5.3: Summary of the FC experimental responses of the flexible arm and 64% load with a target end point position of 45 degrees.

algorithm	rise time (sec)	overshoot		settling time (sec)	steady state error	
		(deg)	(%)		(deg)	(%)
FC, 1st & 2nd modes	0.55	22	45	>5	4	9
FC, no modes	0.6	12	23	>5	7	16
FC, 1st mode	0.55	23	50	>5	1	2
NLFC	0.57	17	33	>5	6	13



(a)



(b)

Figure 5.22: Experimental FC hub position response of the flexible arm and 64% load with a target end point position of 45 degrees

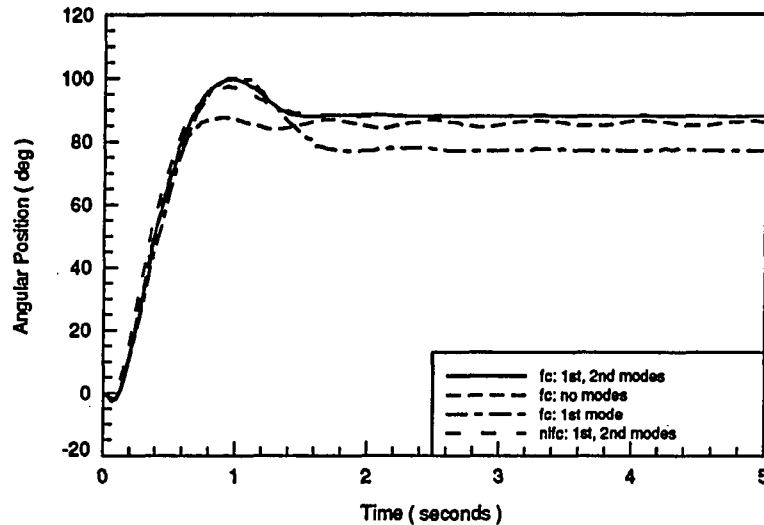
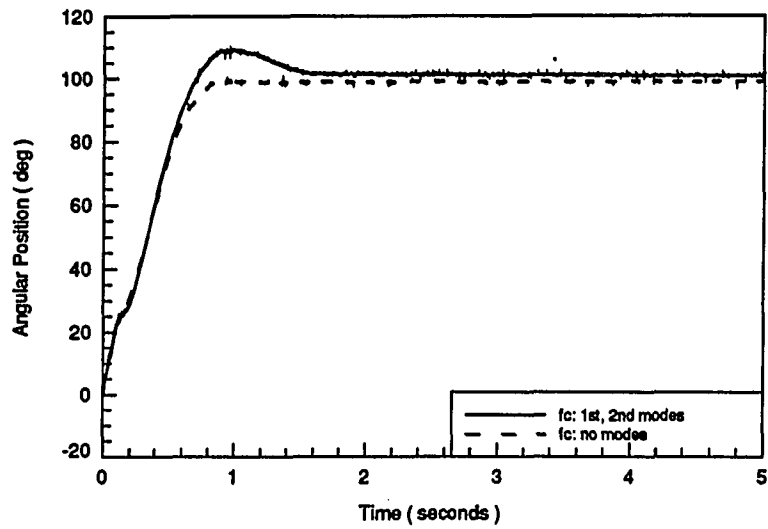


Figure 5.23: Experimental FC end point response of the unloaded arm with a target end point position of 90 degrees

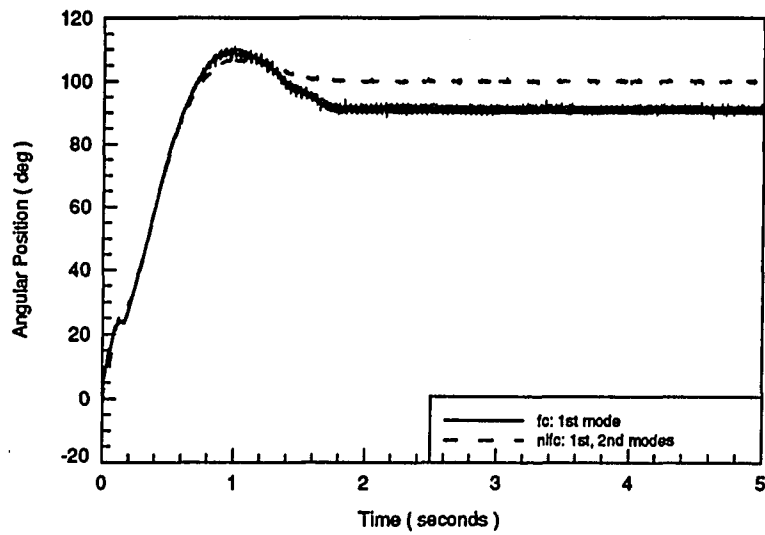
Figure 5.24 shows the pronounced high frequency instability with the FC, first mode algorithm.

Figures 5.25 and 5.26 give the responses of the flexible arm and 23% end mass with a target end point position of 90 degrees. The results are summarized in Table 5.5. All of the algorithms exhibit practically identical rise times. The FC with first and second mode feedback gives the shortest settling time. The NLFC exhibits the same overshoot as the FC with first and second modes. However, the NLFC exhibits a longer settling time. The FC with first mode feedback gave the largest steady state error. Figure 5.26 shows the hub position response of the FC with first mode feedback exhibits the high frequency instability.

Figures 5.27 and 5.28 give the responses of the flexible arm and 64% end mass with a target end point position of 90 degrees. The results are summarized in Ta-



(a)



(b)

Figure 5.24: Experimental FC hub position response of the unloaded arm with a target end point position of 90 degrees

Table 5.4: Summary of the FC experimental responses of the unloaded arm with a target end point position of 90 degrees.

algorithm	rise time (sec)	overshoot		settling time (sec)	steady state error	
		(deg)	(%)		(deg)	(%)
FC, 1st & 2nd modes	0.65	10	11	1.4	-2	-2
FC, no modes	0.7	4	5	2.0	-5	-6
FC, 1st mode	0.6	22	28	1.6	-12	-13
NLFC	0.65	8	9	1.4	-2	-2

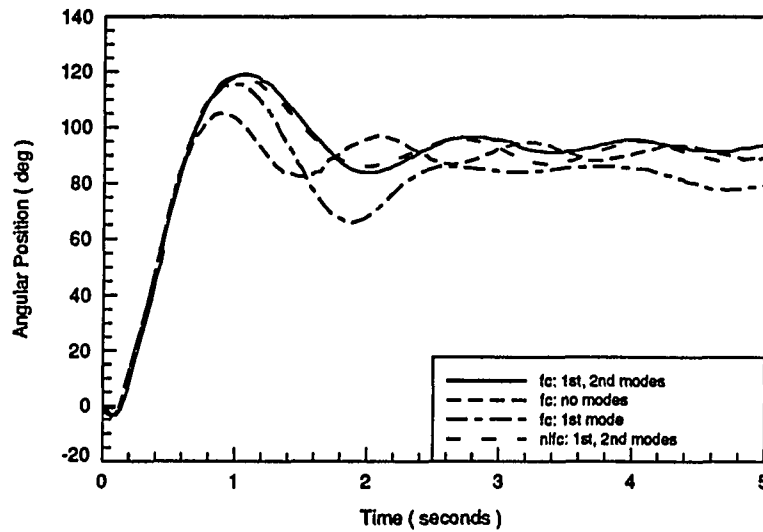
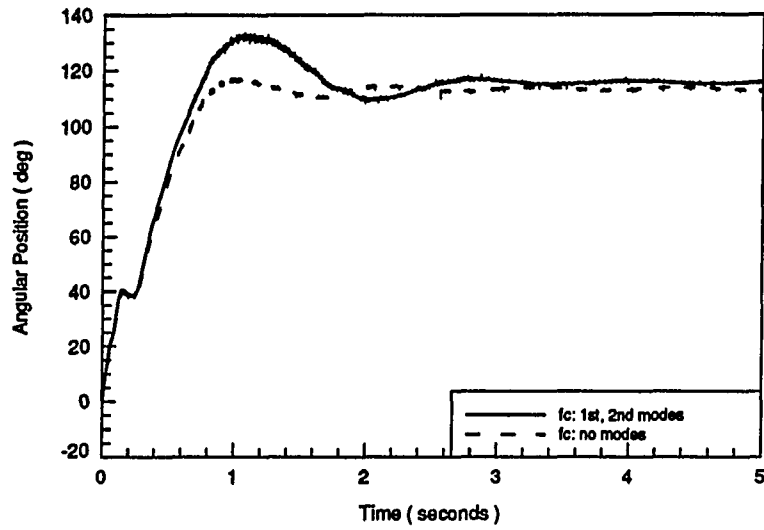
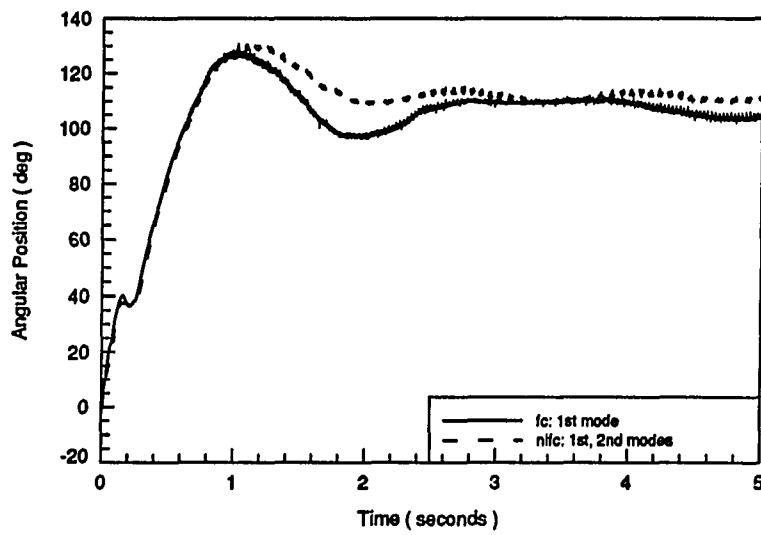


Figure 5.25: Experimental FC end point response of the flexible arm and 23% load with a target end point position of 90 degrees



(a)



(b)

Figure 5.26: Experimental FC hub position response of the flexible arm and 23% load with a target end point position of 90 degrees

Table 5.5: Summary of the FC experimental responses of the flexible arm and 23% load with a target end point position of 90 degrees.

algorithm	rise time (sec)	overshoot		settling time (sec)	steady state error	
		(deg)	(%)		(deg)	(%)
FC, 1st & 2nd modes	0.6	25	27	3.4	4	4
FC, no modes	0.6	15	16	4.5	1	1
FC, 1st mode	0.6	32	39	>5	-7	-8
NLFC	0.6	25	27	>5	1	1

ble 5.6. The control algorithms yield similar results. The rise times are 0.65 seconds with large overshoots. Two of the algorithms did settle. However, the settling times are large. Figure 5.28 shows all of the hub position responses are stable. The similar responses can be attributed to the 8.5 in-lb torque limit. The steady state target torque is 8.46 in-lbs. It is also noted that significant out of plane motion occurs with the 64% end mass. The unloaded arm and arm with 23% end mass exhibits very little out of plane motion.

5.5 Summary of Experimental Results

Tables 5.7 and 5.8 summarize the experimental position and position-derivative control algorithm results. The numerical results given in Table 4.4 can be compared to the experimental results given in Table 5.8. The rise times are very similar. The experimental overshoots are less than the numerical models indicate. This could be contributed to coulomb damping in the servo motor that is not modelled. The settling times obtained experimentally are generally slightly longer than the ones obtained

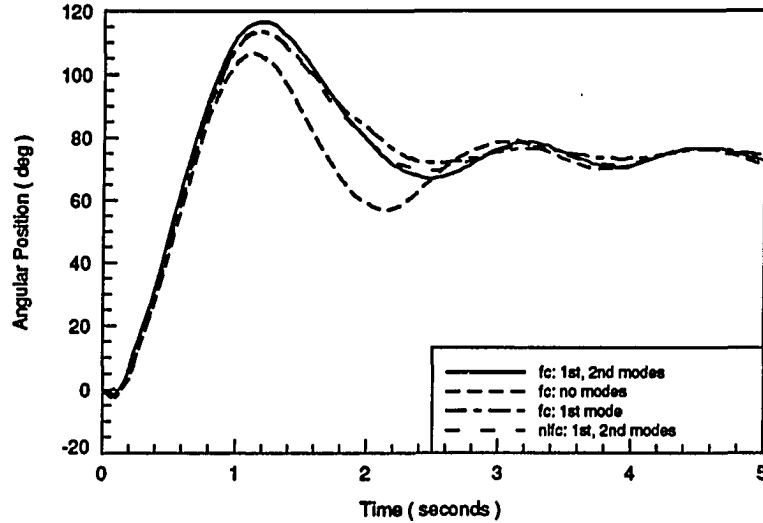
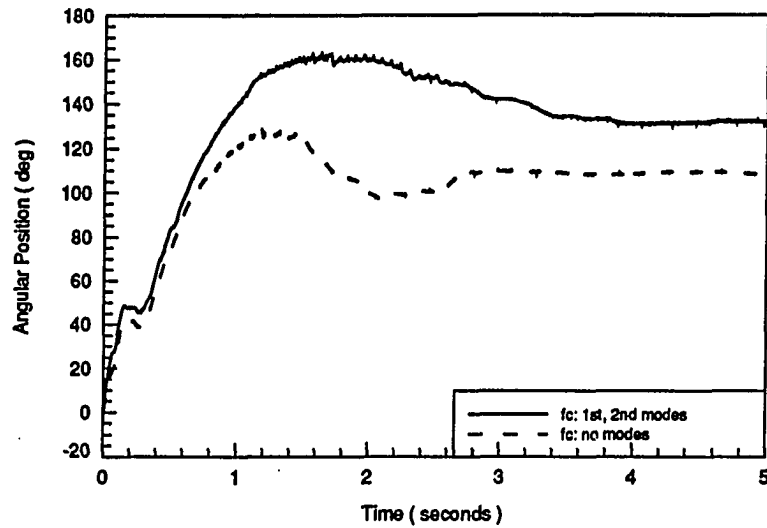


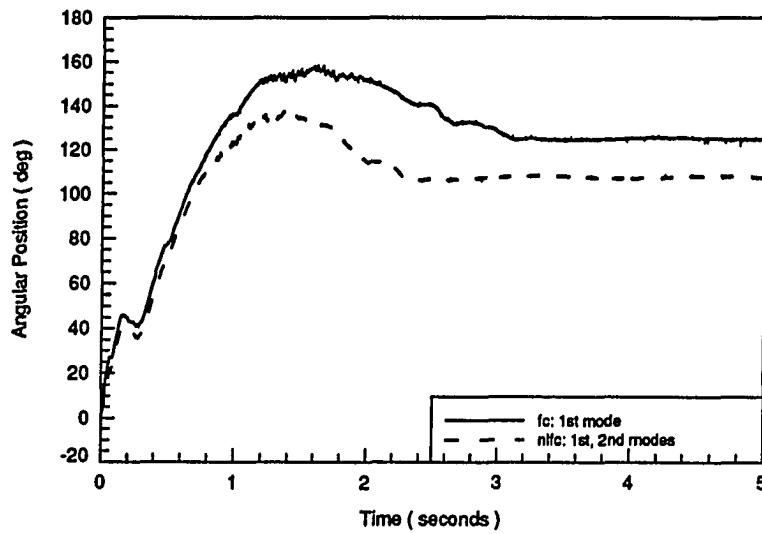
Figure 5.27: Experimental FC end point response of the flexible arm and 64% load with a target end point position of 90 degrees

Table 5.6: Summary of the FC experimental responses of the flexible arm and 64% load with a target end point position of 90 degrees.

algorithm	rise time (sec)	overshoot		settling time (sec)	steady state error	
		(deg)	(%)		(deg)	(%)
FC, 1st & 2nd modes	0.65	40	53	>5	-15	-17
FC, no modes	0.65	32	43	>5	-15	-17
FC, 1st mode	0.65	38	51	3.5	-15	-17
NLFC	0.65	38	51	4.2	-15	-17



(a)



(b)

Figure 5.28: Experimental FC hub position response of the flexible arm and 64% load with a target end point position of 90 degrees

Table 5.7: Summary of the experimental responses of the flexible arm and payloads using the P control algorithm

target end point (deg)	payload (% of arm mass)	rise time (sec)	overshoot		settling time (sec)	steady state error	
			(deg)	(%)		(deg)	(%)
45	0	0.3	36	86	4.8	-3	-7
45	23	0.3	43	91	>5	2	4
45	64	0.5	37	71	>5	7	16
90	0	0.4	55	60	3.8	2	2
90	23	0.5	63	68	>5	2	2
90	64	0.7	70	97	4	-18	-20

numerically. The experimental results also show steady state errors.

Tables 5.1-5.6 summarize the results from the flexible controller. The FC algorithms give improved responses compared to the PD controllers. The feedback gains must be recomputed for each payload. The NLFC gives the best compromise between overshoot and settling time for the unloaded cases. However, the linear FC with first and second mode feedback give better responses with the 23% end mass. All of the algorithms resulted in rather poor responses with the 64% end mass. The FC with first mode feedback shows a high frequency instability in all but the final situation. A vision system may be necessary to minimize the steady state errors.

Table 5.8: Summary of the experimental responses of the flexible arm and payloads using the PD control algorithm

target end point (deg)	payload (% of arm mass)	rise time (sec)	overshoot		settling time (sec)	steady state error	
			(deg)	(%)		(deg)	(%)
45	0	0.45	8	21	4	-7	-16
45	23	0.5	5	10	4	3	7
45	64	0.6	13	24	>5	11	24
90	0	0.5	12	13	3	3	3
90	23	0.5	22	26	>5	-4	-4
90	64	0.7	45	62	3.6	-18	-20

6. CONCLUSIONS

This thesis presents the equations of motion for a flexible arm robot with a payload, including the effects of gravity. The equations are then linearized for use in developing control algorithms.

Using the model, several control algorithms are developed, including PD, LQR, and LQR with prescribed degree of stability. The nonlinear system is then simulated with the control algorithms. A limit is placed on the magnitude of the control torque. This is to prevent the arm from plastically deforming.

The PD controller uses only hub position and velocity as feedback variables. The PD controller produced fast responses followed by large overshoots and long settling times.

The LQR controller uses modal, as well as hub position and velocity feedback. These algorithms are sensitive to the weighting factors used in deriving the feedback gains. Two sets of feedback gains are developed from two different sets of weighting factors. The first LQR results in responses with good rise times, overshoots, and settling times for the unloaded arm. The second LQR results in good responses for the arm with the heaviest payload and a target end point of 45 degrees. The responses of the flexible arm with the heaviest payload and a target end point position

of 90 degrees are poor due to the torque limit. The second LQR results in very slow responses for the lighter payloads.

The LQR with prescribed degree of stability gives better responses if the stability parameter is not large. Numerical results with a prescribed degree of stability of 2 results in faster responses than the original LQR. However, increasing the prescribed degree of stability can result in an unstable system. This is shown in a case with a prescribed degree of stability of 3.

A flexible robot arm in the vertical plane is implemented in an experimental test bed. A variety of control algorithms are tested experimentally. The PD controller is implemented with results similar to the simulation results. Control algorithms that feedback the mode shapes are also implemented. These controllers result in shorter settling times in most cases. During the experiments, it is found that higher order modes can become unstable with large velocity and first mode gains. The second mode feedback gain tends to decrease this instability. A nonlinear controller based on varying the first mode feedback gain with position is also implemented. This controller resulted in smaller overshoots in some cases. For best performance, the control algorithms must have feedback gains determined for each payload. The experimental results show some steady state errors. To limit these errors, an end point position sensor may be needed.

Many avenues for future work exist. A more precise velocity transducer could be implemented. A flexible arm that allows a larger range of flexibility while not plastically deforming could be constructed. A smaller DC servo motor with less coulomb damping could be installed in the test bed. The effects of feeding back more mode shapes and the mode shape time derivatives could be experimentally investigated. A

stochastic model incorporating measurement noise could be developed. A two arm flexible robot could also be implemented.

7. BIBLIOGRAPHY

- [1] Book, W. J. "Control of Flexible (Non-Rigid) Robot Arms." IEEE Video Conference Presentation Notes, 1985.
- [2] Book, W. J. "New Concepts in Lightweight Arms." *Robotics Research, 2nd International Symposium*, MIT Press, Cambridge, 1985.
- [3] Book, W. J., Maizza-Neto, O., and Whitney, D. E. "Feedback Control of Two Beam, Two Joint Systems With Distributed Flexibility." *ASME Journal of Dynamic Systems, Measurement, and Control*, 97 (December 1975): 424-431.
- [4] Singh, S. N. and Schy, A. A. "Decomposition and State Variable Feedback Control of Elastic Robotic Systems." *Proceedings 1985 American Control Conference*, 1 (1985): 375-380.
- [5] Skaar, S. B. and Tucker, B. "Point Control of a One-Link Flexible Manipulator." *Journal of Applied Mechanics*, 53 (March 1986): 23-27.
- [6] Singh, S. N. and Schy, A. A. "Elastic Robot Control: Nonlinear Inversion and Linear Stabilization." *IEEE Transactions on Aerospace and Electronic Systems*, 22 No. 4 (July 1986): 340-347.
- [7] Korolov, V. V., Chen, Y. H. "Controller Design Robust to Frequency Variation in a One-Link Flexible Robot Arm." *ASME Journal of Dynamic Systems, Measurement, and Control*, 111 (March 1989): 9-14.
- [8] Schmitz, E. "Modeling and Control of a Planar Manipulator with an Elastic Forarm." *Proceedings 1989 IEEE International Conference on Robots and Control*, 2 (1989): 894-899.
- [9] Nathan, P. J. and Singh, S. N. "Variable Structure Control of a Robotic Arm with Flexible Links." *Proceedings 1989 IEEE International Conference on Robots and Control*, 2 (1989): 882-887.

- [10] Yeung, K. S. and Chen, Y. P. "Sliding-Mode Controller Design of a Single-Link Flexible Manipulator Under Gravity." *International Journal of Control*, 52 No. 1 (July 1990): 101-117.
- [11] Castelazo, I. A. and Lee, H. "Nonlinear Compensation for Flexible Manipulators." *ASME Journal of Dynamic Systems, Measurement, and Control*, 112 (March 1990): 62-68.
- [12] Asada, H., Ma, Z.-D., and Tokumaru, H. "Inverse Dynamics of Flexible Robot Arms: Modeling and Computation for Trajectory Control." *ASME Journal of Dynamic Systems, Measurement, and Control*, 112 (June 1990): 177-185.
- [13] Chang, L.-W. and Park, K. S. "A Vertical-Plane Motion Control of an Electrohydraulically-Actuated Single-Flexible-Link Arm." *Proceedings 1990 American Control Conference*, 2 (1990): 1208-1213.
- [14] Yuan, K. and Lin, L.-C. "Motor-based Control of Manipulators with Flexible Joints and Links." *Proceedings 1990 IEEE International Conference on Robotics and Control*, 3 (1990): 1809-1814.
- [15] Chiou, B. C. and Shahinpoor, M. "Dynamic Stability Analysis of a Two-Link Force-Controlled Flexible Manipulator." *ASME Journal of Dynamic Systems, Measurement, and Control*, 112 (December 1990): 661-666.
- [16] Choura, S., Jayasuriya, S., and Medick, M. A. "On the Modeling and Open-Loop Control of a Rotating Thin Flexible Beam." *ASME Journal of Dynamic Systems, Measurement, and Control*, 113 (March 1991): 26-33.
- [17] Cetinkunt, S. and Wu, S. "Output Predictive Adaptive Control of a Single-Link Flexible Arm." *International Journal of Control*, 53 No. 2 (February 1991): 311-333.
- [18] Fukuda, T. and Kuribayashi, Y. "Flexibility Control of Elastic Robotic Arms and Its Application to Contouring Control." *Proceedings 1984 IEEE International Conference on Robotics and Automation*, 1 (1984): 540-545.
- [19] Cannon, R. H. and Schmitz, E. "Initial Experiments on the End-Point Control of a Flexible One-Link Robot." *International Journal of Robotics Research*, 3 No. 3 (Fall 1984): 62-75.
- [20] Fukuda, T. "Flexibility Control of Elastic Robotic Arms." *Journal of Robotic Systems*, 2 No. 1 (1985): 73-88.

- [21] Hastings, G. G. and Book, W. J. "Experiments in Optimal Control of a Flexible Arm." *Proceedings 1985 American Control Conference*, 1 (1985): 728-729.
- [22] Sakawa, Y., Matsuno, F., and Fukushima, S. "Modeling and Feedback Control of a Flexible Arm." *Journal of Robotic Systems*, 2 No. 4 (1985): 453-472.
- [23] Rovner, D. M. and Cannon, R. H. "Experiments Toward On-Line Identification and Control of a Very Flexible One-Link Manipulator." *International Journal of Robotics Research*, 6 No. 4 (Winter 1987): 3-19.
- [24] Chalhoub, N. G. and Ulsoy, A. G. "Control of a Flexible Robot Arm: Experimental and Theoretical Results." *ASME Journal of Dynamic Systems, Measurement, and Control*, 109 (December 1987): 299-309.
- [25] Kotnik, P. T., Yurkovich, S., and Ozguner, U. "Acceleration Feedback for Control of a Flexible Manipulator Arm." *Journal of Robotic Systems*, 5 No. 3 (1988): 181-196.
- [26] Chang, L.-W. and Kirkland, M. "Implementation of a Vertical-Plane Motion Control of an Electrohydraulically-Actuated Single-Flexible-Link Arm." *Proceedings 1990 American Control Conference*, 2 (1990): 1214-1219.
- [27] Singer, N. C. and Seering, W. P. "Experimental Verification of Command Shaping Methods for Controlling Residual Vibration in Flexible Robots." *Proceedings 1990 American Control Conference*, 2 (1990): 1738-1744.
- [28] Oakley, C. M. and Barratt, C. H. "End-Point Controller Design for an Experimental Two-Link Flexible Manipulator Using Convex Optimization." *Proceedings 1990 American Control Conference*, 2 (1990): 1752-1759.
- [29] Park, J.-H. and Asada, H. "Design and Control of Minimum-Phase Flexible Arms with Torque Transmission Mechanisms." *Proceedings 1990 IEEE International Conference on Robotics and Control*, 3 (1990): 1790-1795.
- [30] Chiou, B. C. and Shahinpoor, M. "Experimental and Theoretical Observations On the Dynamic Stability of a One-Link Force-Controlled Flexible Manipulator", *Proceedings 1991 IEEE International Conference on Robotics and Automation*, 2 (1991): 1208-1213.
- [31] Schoenwald, D. A., Feddema, J. T., Eisler, G. R., and Segalman, D. J. "Minimum-Time Trajectory Control of a Two-Link Flexible Robotic Manipulator." *Proceedings 1991 IEEE International Conference on Robotics and Automation*, 3 (1991): 2114-2120.

- [32] Hufnagel, A. M. "Gravitational and Coupling Effects in Modeling of an Elastic Robot Arm." Ph.D. dissertation, Iowa State University, Ames, Iowa, 1989.
- [33] Byars, E. F. and Snyder, R. D. *Engineering Mechanics of Deformable Bodies*, third ed., Intext Educational Publishers, New York, 1975.
- [34] Åström, K. J. and Wittenmark, B. *Computer-Controlled Systems*, second ed., Prentice Hall, New Jersey, 1984.
- [35] Integrated Systems Inc. "MATRIXx Control Design Module", seventh ed., Santa Clara, January 1990.
- [36] Kwakernaak, H. and Sivan, R. "Linear Optimal Control Systems." Wiley-Interscience, New York, 1972.
- [37] Anderson, B. D. O. and Moore, J. B. "Linear System Optimization with Prescribed Degree of Stability." *Proceedings IEE*, 116 No. 12 (December 1969): 2083-2087.